JETP Letters, Vol. 81, No. 11, 2005, pp. 543–547. From Pis'ma v Zhurnal Éksperimental'noĭ i Teoreticheskoĭ Fiziki, Vol. 81, No. 11, 2005, pp. 675–679.
Original English Text Copyright © 2005 by Korenman, Pomerantsev, Popov.

Coulomb Deexcitation of Muonic Hydrogen within the Quantum Close-Coupling Method¶

G. Ya. Korenman, V. N. Pomerantsev, and V. P. Popov

Institute of Nuclear Physics, Moscow State University, Moscow, 119899 Russia

Received April 21, 2005

The Coulomb deexcitation of muonic hydrogen in collisions with the hydrogen atom has been studied in the framework of the fully quantum-mechanical close-coupling method for the first time. The calculations of the *l*-averaged cross sections of the Coulomb deexcitation are performed for $(\mu p)_n$ and $(\mu d)_n$ atoms in the initial states with the principal quantum number $n = 3$–9 and at relative energies $E = 0.1$–100 eV. The obtained results for the *n* and *E* dependences of the Coulomb deexcitation cross sections drastically differ from the semiclassical results. An important contribution of the transitions with $\Delta n > 1$ to the total Coulomb deexcitation cross sections (up to ~37%) is predicted. © *2005 Pleiades Publishing, Inc.*

PACS numbers: 74.50.+r, 74.80.Fp

INTRODUCTION

Exotic hydrogen atoms are formed in highly excited states. The ensuing deexcitation proceeds via many intermediate states up to nuclear absorption or transition to the ground state. The collisional processes play an important role in this cascade. In particular, the elastic scattering and Stark transitions decelerate while the Coulomb deexcitation (CD) accelerates the exotic atoms, influencing their quantum numbers and energy distributions. The CD process has attracted a lot of attention, especially after "hot" πp atoms with kinetic energies up to 200 eV were found experimentally [1, 2]. The most plausible explanation of the high-energy components of the exotic atoms is that part of the transitions from the states with $n \geq 3$ proceeds via the CD.

The theoretical study of the CD process has been performed up to now by three different approaches. The first results were obtained by Bracci and Fiorentini [3] in the two-state semiclassical approach with some additional approximations (hereinafter referred to as the BF model). Later, the CD cross sections were calculated within the advanced adiabatic (AA) approach [4, 5] (see also references therein) based on the adiabatic hidden crossing theory [6], and within the classical-trajectory Monte Carlo (CTMC) method [7]. While the CTMC and BF results are in fair agreement, the more elaborated AA approach [4, 5] gives much smaller cross sections than [3]. On the other hand, the BF and CTMC approaches cannot be expected to give reliable results for the CD process in low-*n* states. Therefore, the situation in the most interesting region ($n = 3$–7) is rather ambiguous, and it is necessary to study the CD process within the more realistic quantum-mechanical approach.

In this paper, we study the Coulomb deexcitation of $(\mu p)_n$ and $(\mu d)_n$ atoms in collisions with H, using the close-coupling method. To illustrate some gross features of the calculated cross sections, we present here only the *l*-averaged CD cross sections.

FORMALISM

The close-coupling (CC) method gives a unified quantum-mechanical treatment of nonreactive scattering processes

$$(a\mu^-)_{nl} + (be)_{1s} \longrightarrow (a\mu^-)_{n'l'} + (be)_{1s} \qquad (1)$$

including elastic scattering ($n' = n$, $l' = l$), Stark transitions ($n' = n$, $l' \neq l$), and Coulomb deexcitation ($n' < n$). Here, *a* and *b* are nuclei of hydrogen isotopes (*p*, *d*, or *t*). In the present consideration, as well as in the previous studies [3, 7], we restrict ourselves to the "frozen" electron approximation; i.e., the electron state is fixed in its ground state during the collision. The CC approach can be extended in a straightforward manner to include the target electron excitations.

The total nonrelativistic Hamiltonian of the four particles ($a\mu^- + be$) in the c.m. system is given by

$$H = -\frac{1}{2m}\Delta_{\mathbf{R}} + h_\mu(\boldsymbol{\rho}) + h_e(\mathbf{r}) + V(\mathbf{r}, \boldsymbol{\rho}, \mathbf{R}). \qquad (2)$$

Here, *m* and $\mathbf{R} = \mathbf{R}_{be} - \mathbf{R}_{a\mu}$ are the reduced mass and relative coordinate of the colliding subsystems, $\mathbf{R}_{be}$ and $\mathbf{R}_{a\mu}$ are the coordinates of the centers of mass of the atoms, and $\boldsymbol{\rho} = \mathbf{r}_\mu - \mathbf{r}_a$ and $\mathbf{r} = \mathbf{r}_e - \mathbf{r}_b$ are their inner coordinates. The eigenvalues and eigenfunctions of the inner Hamiltonians h_μ and h_e of the $(a\mu)$ and (be) atoms

¶ The text was submitted by the authors in English.

will be denoted as ε_n, $\Phi_{nlm}(\boldsymbol{\rho})$, and ϵ_{1s}, $\varphi_{1s}(\mathbf{r})$, respectively. The interaction potential

$$V(\mathbf{r}, \boldsymbol{\rho}, \mathbf{R}) = V_{ab} + V_{\mu b} + V_{ae} + V_{\mu e}, \quad (3)$$

includes the pair Coulomb interactions $V_{\alpha\beta}$ between the particles from two colliding subsystems. The atomic units ($\hbar = e = m_e m_b/(m_e + m_b) = 1$) will be used throughout the paper unless otherwise stated.

In the framework of the method, the total wavefunction of the system with the definite energy E and quantum numbers of the total angular momentum J and M is presented as

$$\Psi_E^{JM}(\mathbf{r}, \boldsymbol{\rho}, \mathbf{R}) = R^{-1}\sum_{nlL} G_{nlL}^J(R)|1s, nl, L : JM\rangle, \quad (4)$$

where the basis states$|1s, nl, L : JM\rangle$ are the tensor product of the inner atomic wavefunctions $|1s\rangle$, $|nlm\rangle$ and the relative angular momentum function $Y_{L\Lambda}(\hat{\mathbf{R}})$. The radial functions of the relative motion $G_{nlL}^J(R)$ satisfy the coupled second-order differential equations

$$\left(\frac{d^2}{dR^2} + k_n^2 - \frac{L(L+1)}{R^2}\right)G_{nlL}^J(R) = 2m\sum_{n'l'L'} W_{nlL,\,n'l'L'}^J(R)G_{n'l'L'}^J(R), \quad (5)$$

where $k_n^2 = 2m(E_{cm} + \varepsilon_{n_0} - \varepsilon_n)$; E_{cm} and n_0 are the energy of the relative motion and the principal quantum number in the entrance channel. In order to obtain the matrix elements of interaction potential (3),

$$W_{nlL,\,n'l'L'}(R) = \langle 1s, nl, L : JM|V|1s, n'l', L' : JM\rangle \quad (6)$$

we average it over the electron coordinate $\mathbf{r}$ and, then, use the multipole expansion. The following integration over $\boldsymbol{\rho}$ and $\hat{\mathbf{R}}$ reduces matrix element (6) to a multiple finite sum.

In the present study, we restrict the basis set to the open channels only. Then, the boundary conditions at $R \longrightarrow \infty$ for the radial functions contain ingoing and outgoing waves in the entrance channel and outgoing waves in all the other channels. Coupled differential equations (5) are solved numerically by the Numerov method. In fact, we solve the equations with the standing-wave boundary conditions involving the real and symmetrical K matrix instead of the S matrix. The corresponding T matrix is given by the equation $T = 2K/(I - iK)$, where I is the unit matrix. With the calculated T matrix, one can obtain the cross sections of all processes (1). In this paper, we discuss the l-averaged ($n \longrightarrow n'$) cross sections

$$\sigma_{n\to n'}(E) = \frac{\pi}{k_n^2 n^2}\sum_{ll'JLL'}(2J+1)\left|T_{nlL\to n'l'L'}^J\right|^2, \quad (7)$$

and the total CD cross sections

$$\sigma_n^{\mathrm{CD}}(E) = \sum_{n'<n}\sigma_{n\to n'}(E). \quad (8)$$

RESULTS

The CC approach has been used to obtain the cross sections for the collisions of the $(\mu^- p)_n$ and $(\mu^- d)_n$ atoms with H atoms for $n = 3$–9 at $E = 0.1$–100 eV. The calculations of the CD cross sections for the given initial principal quantum number n were done with two sets of basis states: (a) the restricted basis including the states of two neighboring levels with $n' = n$, $n - 1$ with all allowable l' (we refer these results, for brevity, as the "two-level" approximation) and (b) the extended basis incorporating all the states with $n' \le n$. Notice that the CC two-level approximation, in some sense, is similar to the two-state approximations that were used by previous authors [3–5].

In both series of calculations, the sums over the values of J in the cross sections are done until an accuracy better than 0.1% is reached at all energies. The analysis of the J dependence of the partial cross sections $\sigma_{nn'}^J$ shows that the main part of the CD cross sections comes from the partial waves with relatively low J as compared with elastic scattering and Stark transitions. The same result was found in [5]. For example, for $n = 3$ and E_{cm} up to 100 eV, we found for the CD process that $J_{\max}^{\mathrm{CD}} \le 15$, whereas, for the elastic scattering, $J_{\max}^{\mathrm{el}} \lesssim 120$. For the higher n, the value $J_{\max}^{\mathrm{CD}}$ increases approximately $\sim\sqrt{n}$ and the interrelation between $J_{\max}^{\mathrm{CD}}$ and $J_{\max}^{\mathrm{el}}$ remains similar. This result is correlated with the relative importance of the different multipole terms of the interaction potential.

According to our study, the elastic scattering and Stark transitions can be reasonably described within the CC method if only the long-range dipole terms in matrix elements (6) are taken into account. In contrast, to provide the proper treatment of the CD, all the allowed multipoles ($t \le t_{\max} = 2n - 2$) have to be included. For example, the CD cross section $\sigma_{6\to 5}$ at $E_{\mathrm{cm}} = 0.1$ eV calculated in the "dipole" approximation is nearly twice as large as that obtained with all the multipoles included. Such a strong effect of the higher multipoles on the inelastic transitions is due to the fact that the main contribution to the inelastic transitions comes from small distances between colliding objects.

The CD cross sections of the $(\mu p) + H$ and $(\mu d) + H$ collisions in the two-level approximation are shown in Figs. 1 and 2 together with the results of Bracci and Fiorentini [3] and Ponomarev and Solov'ev [5], respectively. It is seen from Fig. 1 that our two-level CC results are in satisfactory agreement with the results of the BF model [3] for $n = 5, 7, 9$, especially in the region

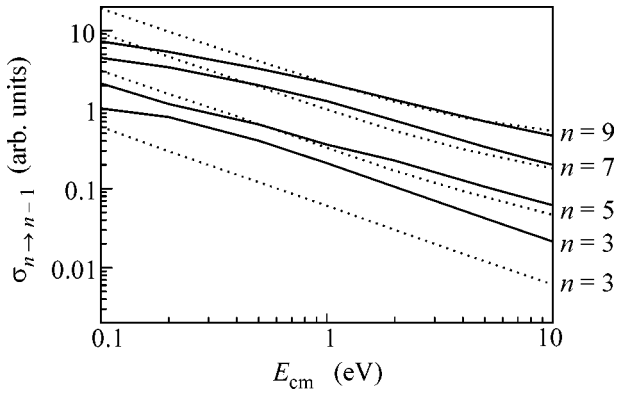

Fig. 1. The CD cross sections $\sigma^{CD}_{n,\,n-1}$ (a.u.) for $(\mu p)_n + H$ collisions with $n = 3, 5, 7, 9$ calculated within the CC two-level approximation (solid lines) in comparison with the results of Bracci and Fiorentini [3] (dotted lines).

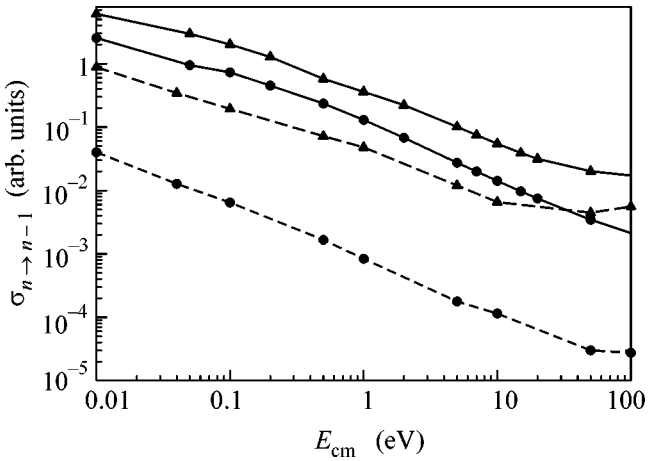

Fig. 2. The cross sections of the Coulomb deexcitation $\sigma^{CD}_{n,\,n-1}$ (a.u.) for $(\mu d)_n + H$ collisions calculated within the CC two-level approximation (solid lines) in comparison with the AA results [5] (dotted lines). The triangles and closed circles mark the curves for the $5 \longrightarrow 4$ and $3 \longrightarrow 2$ transitions, respectively.

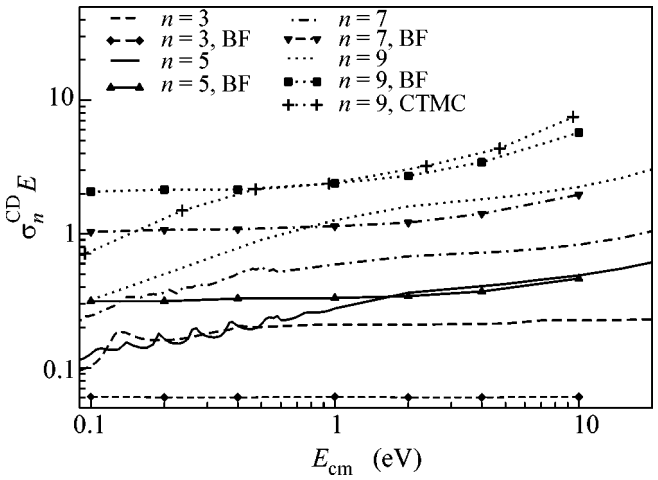

Fig. 3. Energy dependence of the value $E\sigma^{CD}_n(E)$ for different n in the $(\mu p)_n + H$ collisions obtained within the quantum CC approach (the curves without symbols) in comparison with the BF [3] (the curves with triangles and squares) and CTMC [7] (the curve with crosses) results. The dashed, solid, dotted–dashed, and dotted curves are for $n = 3$, 5, 7, and 9, respectively.

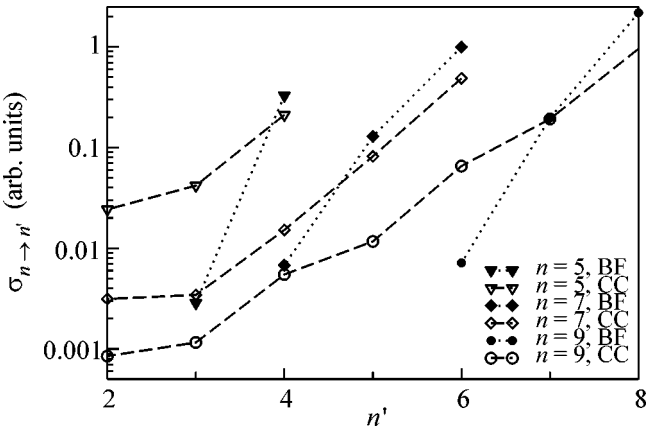

Fig. 4. Dependence of the CD cross sections on the final principal quantum number n' for the different initial n in the $(\mu p)_n + H$ collisions at $E = 1$ eV. The dashed and dotted lines connect the points obtained in the present paper and in [3], respectively. The triangles, squares, and circles correspond to the initial $n = 5$, 7, and 9.

$E_{cm} > 1$ eV. On the other hand, Fig. 2 shows that our results for μd are several times greater than the results obtained within the AA approach [5] for the transition $5 \longrightarrow 4$ and even much greater (almost by two orders of magnitude) for the transition $3 \longrightarrow 2$. The reason for this drastic discrepancy is not clear at present.

The results of the calculations with the extended basis set including all the states with $n' \le n$ are shown in Figs. 3 and 4 and in the table. The comparison of these results with those obtained in the CC two-level approximation shows that the effect of the transitions with $\Delta n > 1$ on the CD cross sections is appreciable for $n \ge 4$. Moreover, the inclusion of the channels with $\Delta n > 1$ leads to a strong suppression of the main $\Delta n = 1$ transitions in comparison with the two-level CC approximation and, due to this, the total CD cross sections are also suppressed. For example, for $n = 4$ and 6, this suppression is about 1.5–2 and 3 times, respectively. As a result, the influence of the channels with $\Delta n > 1$ leads to an essential change in the E and n

The CD cross sections $\sigma_{nn'}$ and σ_n^{CD} (in a.u.) for $(\mu p)_n + H$ collisions calculated in the quantum-mechanical close-coupling approach

E_{cm}, eV	0.1	0.2	0.5	1.0	2.0	5.0	7.0	10.0	15.0	20.0
σ_3^{CD}	1.035	0.805	0.403	0.210	0.105	0.043	0.032	0.023	0.015	0.012
σ_{43}	0.936	0.704	0.515	0.333	0.189	0.083	0.060	0.043	0.030	0.024
σ_{42}	0.458	0.259	0.121	0.069	0.037	0.016	0.012	0.008	0.006	0.005
σ_4^{CD}	1.397	0.965	0.637	0.403	0.226	0.098	0.071	0.052	0.036	0.029
σ_{54}	0.943	0.574	0.306	0.211	0.147	0.070	0.054	0.041	0.031	0.026
σ_{53}	0.219	0.164	0.074	0.042	0.022	0.009	0.007	0.005	0.003	0.003
σ_{52}	0.108	0.082	0.041	0.024	0.013	0.006	0.004	0.003	0.002	0.002
σ_5^{CD}	1.270	0.819	0.422	0.277	0.182	0.085	0.065	0.049	0.037	0.031
σ_{65}	1.619	0.856	0.442	0.250	0.136	0.058	0.043	0.032	0.024	0.021
σ_{64}	0.440	0.270	0.178	0.115	0.064	0.028	0.021	0.016	0.012	0.010
σ_{63}	0.070	0.039	0.024	0.013	0.006	0.003	0.002	0.002	0.001	0.001
σ_6^{CD}	2.166	1.189	0.661	0.387	0.211	0.090	0.067	0.050	0.038	0.033
σ_{76}	2.005	1.410	0.902	0.488	0.275	0.119	0.088	0.065	0.048	0.040
σ_{75}	0.354	0.279	0.136	0.082	0.054	0.024	0.019	0.014	0.011	0.010
σ_{74}	0.070	0.053	0.026	0.015	0.008	0.004	0.003	0.002	0.002	0.001
σ_7^{CD}	2.454	1.762	1.076	0.591	0.340	0.148	0.111	0.083	0.062	0.053
σ_{87}	2.484	1.848	1.322	0.839	0.494	0.221	0.165	0.123	0.091	0.075
σ_{86}	0.396	0.294	0.186	0.128	0.084	0.037	0.028	0.021	0.016	0.013
σ_{85}	0.186	0.128	0.071	0.042	0.023	0.010	0.008	0.006	0.005	0.004
σ_{84}	0.031	0.018	0.010	0.006	0.003	0.001	0.001	0.001	0.001	0.001
σ_8^{CD}	3.108	2.297	1.594	1.018	0.605	0.271	0.202	0.151	0.112	0.094
σ_{98}	2.070	1.773	1.319	0.956	0.604	0.287	0.221	0.170	0.131	0.114
σ_{97}	0.608	0.460	0.295	0.192	0.136	0.062	0.048	0.036	0.028	0.024
σ_{96}	0.294	0.191	0.106	0.065	0.037	0.017	0.013	0.010	0.008	0.008
σ_{95}	0.051	0.039	0.021	0.012	0.007	0.003	0.002	0.002	0.001	0.001
σ_9^{CD}	3.055	2.486	1.754	1.233	0.789	0.371	0.285	0.220	0.170	0.148

dependences as compared with the two-level CC calculation.

Beginning from [3], it is commonly believed that the CD cross sections at low energies behave like $1/E$. In Fig. 3, we show the total CD cross sections multiplied by energy, which reveal more explicitly the distinction from the $1/E$ behavior. The present CD cross sections obtained within the extended basis are compared here with the results of the BF model [3] for $n = 3, 5, 7, 9$ and of the CTMC calculations by Jensen and Markushin [7] for $n = 9$. As is seen from this figure, the energy dependence of the CC cross sections in the region $E > 1$ eV, as a whole, is in qualitative agreement with the BF [3] and CTMC [7] models. But, at lower energies, the CC results do not confirm the $1/E$ energy dependence of the cross sections, except for the state with $n = 3$. At $E \lesssim 1$ eV and $n > 3$, our results show rather a $1/\sqrt{E}$ behavior of the CD cross sections (a similar behavior can be also seen in the CTMC results [7] for $n = 9$).

However, the more detailed insight reveals some resonancelike structures in the energy behavior of the CC cross sections at $E < 1$ eV (which are the most pronounced for $n = 5$ in Fig. 3). This behavior of the CD cross sections is due to the shape resonances in the entrance channel. Similar resonances at the same energy region have already been noted for the elastic scattering and Stark transition cross sections obtained within the one-channel adiabatic approximation [8, 9].

The BF model predicts the power n dependence nearly to n^γ with $\gamma > 2$. However, the present consideration does not confirm that the CD cross sections have such a scale factor depending on n (see Fig. 3 and the table). Moreover, for $n = 4$–6, the nonmonotonic behav-

ior of the σ_n^{CD} as a function of n is seen. A power dependence of the CD cross sections is found in the high-energy region ($E > \varepsilon_n - \varepsilon_{n-1}$).

The dependence of the partial CD cross sections $\sigma_{n \to n'}$ on the final principal quantum number n' is shown in Fig. 4 (see also the table). Our results for the distribution of the CD transitions over the final states n' are substantially different from the results of other approaches. The present calculations confirm that $\Delta n = 1$ transitions dominate, in agreement with the previous results [3, 5, 7]. At the same time, the transitions with $\Delta n > 1$ are strongly enhanced as compared to the results in [3, 5] and are in satisfactory agreement with CTMC calculations [7]. The relative contribution of the transitions with $\Delta n > 1$ does not exceed 1% in the AA approach [5], 10% in the BF model [3], and is about 19% in the CTMC calculations [7] (for $n = 9$). Our CC calculations of $\Delta n > 1$ transitions make up a substantial fraction of the total CD cross sections (16–37%) for $n \geq 4$ and at all the energies under consideration.

CONCLUSIONS

We have studied the main features of the Coulomb deexcitation of excited (μp) and (μd) atoms in collision with the hydrogen atom in the framework of the close-coupling approach. The present quantum-mechanical treatment of the CD process leads to substantially new results in comparison with the previous studies; in particular, these include the following:

(i) the transition $3 \longrightarrow 2$ is strongly enhanced;

(ii) the dominant transitions with $\Delta n = 1$ for $n \geq 4$ are essentially suppressed (about two to three or more times) for all energies under consideration;

(iii) the fraction of the $\Delta n > 1$ transitions is very important and reaches up to 37%;

(iv) the n dependence of the CD cross sections is drastically changed;

(v) finally, the CD cross sections at $E \lesssim 1$ eV are suppressed and its behavior is like $1/\sqrt{E}$.

The gross features of the CD process found here must take place for other exotic hydrogen atoms.

The obtained results are very important for more realistic studies of the kinetics and explanation of a high-energy fraction of exotic hydrogen.[1] The more detailed results will be published elsewhere.

We are grateful to Prof. L.I. Ponomarev for his stimulating interest and fruitful discussions, to the participants of the seminar in MUCATEX for useful discussions, and to T. Jensen and V. Markushin for sending the data on the CD cross sections for $n = 9$. This work was partially supported by the Russian Foundation for Basic Research, grant no. 03-02-16616.

REFERENCES

1. J. F. Crawford, M. Daum, R. Frosch, *et al.*, Phys. Rev. D **43**, 46 (1991).
2. A. Badertscher, M. Bogdan, P. F. A. Goudsmit, *et al.*, Phys. Lett. B **392**, 278 (1997).
3. L. Bracci and G. Fiorentini, Nuovo Cimento A **43**, 9 (1978).
4. A. V. Kravtsov, A. I. Mikhailov, L. I. Ponomarev, and E. A. Solov'ev, Hyperfine Interact. **138**, 99 (2001).
5. L. I. Ponomarev and E. A. Solov'ev, Yad. Fiz. **65**, 1615 (2002) [Phys. At. Nucl. **65**, 1575 (2002)].
6. E. A. Solov'ev, Usp. Fiz. Nauk **157**, 437 (1989) [Sov. Phys. Usp. **32**, 228 (1989)].
7. T. S. Jensen and V. E. Markushin, physics/0205076 and private communication.
8. V. P. Popov and V. N. Pomerantsev, Hyperfine Interact. **119**, 137 (1999).
9. V. V. Gusev, V. P. Popov, and V. N. Pomerantsev, Hyperfine Interact. **119**, 141 (1999).

[1] After this paper had been written, we received a private communication from T. Jensen concerning the results of his calculations of the density dependence of the relative K X-ray yields for muonic hydrogen. Using our data on the CD cross sections, he obtains much a better agreement with the experimental data.

JETP Letters, Vol. 81, No. 11, 2005, pp. 548–550. Translated from Pis'ma v Zhurnal Éksperimental'noĭ i Teoreticheskoĭ Fiziki, Vol. 81, No. 11, 2005, pp. 680–682.
Original Russian Text Copyright © 2005 by Gavrilov, Grafutin, Ilyukhina, Myasishcheva, Prokop'ev, Timoshenkov, Funtikov.

Direct Experimental Observation of the Positronium Atom in Porous Silicon by Positron Annihilation Spectroscopy

S. A. Gavrilov[1], V. I. Grafutin[2], O. V. Ilyukhina[2], G. G. Myasishcheva[2], E. P. Prokop'ev[2], S. P. Timoshenkov[1], and Yu. V. Funtikov[2]

[1] *Moscow State Institute of Electronic Engineering (Technical University), Zelenograd, Moscow region, 124498 Russia*
[2] *Institute of Theoretical and Experimental Physics, ul. Bol'shaya Cheremushkinskaya 25, Moscow, 117218 Russia*
e-mail: epprokopiev@mail.ru

Received November 24, 2004; in final form, April 29, 2005

An analysis of the angular distribution of annihilation photons allows us to report the direct experimental observation of the positronium atom in porous silicon. © *2005 Pleiades Publishing, Inc.*

PACS numbers: 71.60.+z

Previous studies of positron annihilation in porous silicon [1–6] suggested that positronium atoms could exist in it. However, these works did not give direct experimental evidence for the formation of positronium atoms in porous silicon. Here, we report the results of precision experiments on positron annihilation in porous silicon. The experimental data allowed us to distinguish parapositronium annihilation components in the annihilation spectra.

In our experiments, we used a standard technique based on the measurement of the angular distribution of annihilation photons [7–10]. It follows from the energy–momentum conservation law that, in the 2γ annihilation of a positron–electron pair at rest, two γ-ray photons are emitted in opposite directions (at an angle of 180°) with the equal energies m_0c^2 = 0.511 MeV. If the pair momentum p is nonzero, the angles between the γ-ray photons differ from 180° by a value of θ (in the laboratory frame of reference). The range of θ angles is very narrow (less than 1°); therefore, the deviation of the angle from 180° rather than the angle itself is designated as the angle of divergence. The distribution over θ angles is called the angular distribution of annihilation photons. If the pair momentum is $p \ll m_0c$, the angle θ is determined by the equation

$$\theta = p_\perp/m_0c. \quad (1)$$

Thus, the momentum of e^+–e^- pairs (or electrons, if the positron momentum is small as compared with the electron momentum) can be determined by measuring the coincidence counting rate of γ-ray photons in 2γ annihilation as a function of angle θ (the deviation of the angle between γ-ray photons from 180°). The experimental procedure was described in detail elsewhere [7–10].

The angular resolution of currently available instruments is 0.3 mrad or smaller (with good statistics, 10^4–10^5 pulses per point at a maximum of the $f(\theta)$ curve). This resolution makes it possible to obtain the detailed structure of correlation curves (e.g., see [7, 9]). Angular correlation spectra may contain narrow and broad components. The narrow component is usually associated with low-energy parapositronium atoms, and the broad component is due to the annihilation of free positrons or orthopositronium on the electrons of the medium. In the annihilation of completely thermalized parapositronium atoms at room temperature, the deviation of the angle between two annihilation γ-ray photons from 180° is only θ ≈ 0.5 mrad or θ ≈ 10 mrad for the broad component. The experimental spectra are adequately described by the superposition of several Gaussian functions, and a parabolic component is added in the case of metals and elemental semiconductors. Each of the Gaussian functions describes a specific channel of positron annihilation, and it is characterized by intensity (annihilation probability) and variance, which is uniquely related to the energy of the annihilating pair.

Porous silicon layers different in porosity and the chemical surface composition of nanocrystals were chosen as test materials. Single-crystal silicon doped with boron with a resistivity of 0.03 Ω cm and the surface orientation ⟨111⟩ was used as a substrate. Porous silicon was formed by anodic dissolution in an HF (48%)–C_2H_5OH mixture with ratios between the components equal to 2 : 1, 1 : 1, and 1 : 3 to obtain layers with 45, 55, and 70% porosity, respectively. The anodic treatment was performed at a current density of 10 mA/cm^2 at room temperature. In all the samples, the thickness of a porous layer was 20 μm. A portion of the samples was treated in an aqueous solution of $PdCl_2$ (0.1 g/l) immediately after formation. This treatment results in the deposition of palladium as a continuous film several monolayers in thickness on the surface of nanocrystals [11].

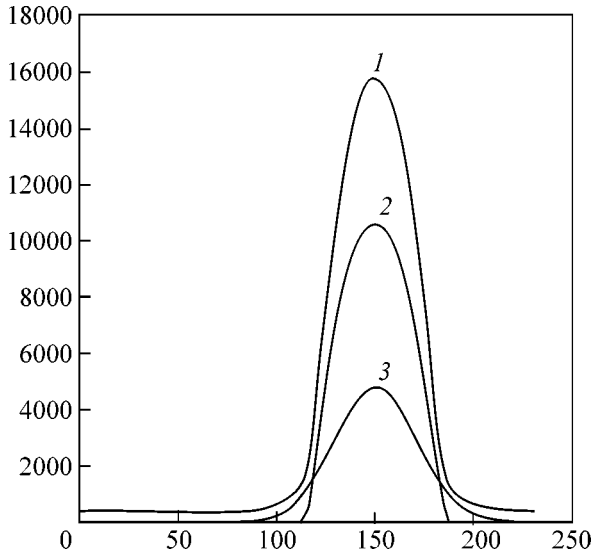

Fig. 1. Angular distributions of annihilation photons in single-crystal silicon samples (mirror *p*-type Si; ⟨111⟩ orientation; KDB-10; $h = 340$ μm): (*1*) experimental data including a background and the sum of parabolic and Gaussian components and (*2*) and (*3*) parabolic and Gaussian components of the spectrum, respectively. The analyzer channels (channel interval of 0.2 mrad) and the number of events are plotted on the abscissa and ordinate, respectively.

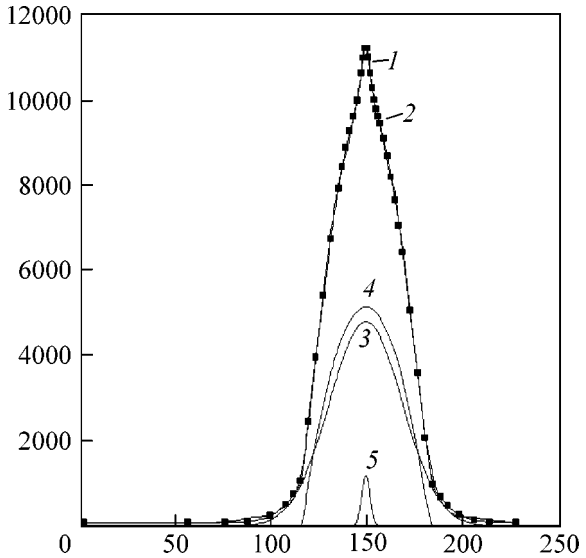

Fig. 2. Angular distributions of annihilation photons in porous silicon samples (⟨111⟩ orientation; KDB-0.03; h = 360–370 μm; HF–C_2H_5OH, 2 : 1; porosity, 45 ± 3%; two Gaussians + a parabola) (see table): (*1*) total spectrum (the sum of spectra *3*–*5*), (points *2*) experimental data, (*3*) the first Gaussian component of the spectrum, (*4*) the parabolic component of the spectrum, and (*5*) the second Gaussian component of the spectrum. The analyzer channels (channel interval of 0.2 mrad) and the number of events are plotted on the abscissa and ordinate, respectively.

The angular distributions of annihilation photons of porous silicon samples (see Figs. 1–3 and the table) are adequately approximated by a parabola (I_p) and two Gaussians (I_{g1}, I_{g2}) (Fig. 2). At the same time, these spectra in defect-free silicon crystals (Fig. 1) are represented by the superposition of a parabola and a Gaussian function. Positron annihilation characterized by the parabolic component can be explained by the annihilation of positrons in the valence band of silicon [9]. In turn, the broad Gaussian component I_{g2} was due to the annihilation of positrons and positronium via various paths in the bulk of the crystal, in the pore volume, and on the pore surface, whereas the narrow Gaussian component I_{g1} was due to the annihilation of parapositronium in the pore volume. The FWHM of this component is on the order of 0.5 mrad, which corresponds to the kinetic energy of the annihilating positron–electron pair equal to 0.079 ± 0.012 eV, and the intensity of this component is on the order of 1.5%. Thus, the total yield of positronium in porous silicon is as high as 6%. Analogous conclusions were drawn from an analysis of difference curves normalized to the unit angular distribution of annihilation photons in porous and single-crystal silicon samples (Fig. 3). These data are direct experimental evidence for the existence of slow quasithermalized parapositronium in pores.

The experimental results allow us to hope that further studies will make it possible to relate the parameters of annihilation spectra to pore size and topology.

We are grateful to Yu.V. Kopaev for stimulating discussions and helpful remarks.

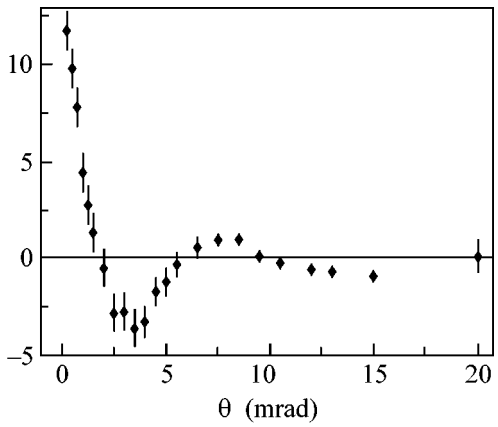

Fig. 3. Difference curves normalized to the unit angular distribution of annihilation photons in porous and single-crystal silicon samples. Porous Si; ⟨111⟩, KDB-0.03; h = 360–370 μm; HF–C_2H_5OH, 2 : 1; and $J = 20$ mA/cm^2. The angle between annihilation photons and the number of events are plotted on the abscissa and ordinate, respectively.

Parameters of the test samples of porous silicon, sample preparation conditions, and characteristics of the angular distributions of annihilation photons

No.	Sample characteristics	$I_{g1} = S_{g1}/S_{sum}$	$I_{g2} = S_{g2}/S_{sum}$	$I_p = S_p/S_{sum}$	Note
PR86	Porous Si, ⟨111⟩, KDB-0.03 h = 20 μm, HF : C_2H_5OH = 2 : 1 J = 20 mA/cm^2	0.015 ± 0.003	0.493 ± 0.052	0.492 ± 0.044	Porosity ~ 45 ± 3%
PR16	Porous Si, ⟨111⟩, KDB-0.03 h = 20 μm, HF : C_2H_5OH = 1 : 1 J = 10 mA/cm^2, t = 2400 s	0.004 ± 0.001	0.504 ± 0.036	0.492 ± 0.031	
PR17	Porous Si, ⟨111⟩, KDB-0.03 h = 20 μm, HF : C_2H_5OH = 1 : 1 J = 10 mA/cm^2, t = 2400 s	0.006 ± 0.003	0.492 ± 0.045	0.502 ± 0.038	+10 min in PdCl
PR18	Porous Si, ⟨111⟩, KDB-0.03 h = 20 μm, HF : C_2H_5OH = 1 : 3 J = 10 mA/cm^2		0.325 ± 0.030	0.675 ± 0.036	
PR19	Porous Si, ⟨111⟩, KDB-0.03 h = 20 μm, HF : C_2H_5OH = 1 : 3 J = 10 mA/cm^2		0.316 ± 0.031	0.684 ± 0.038	+10 min in PdCl

Note: The thickness of silicon wafers was ≈ 360–370 μm; h is the thickness of a porous silicon layer; ⟨111⟩ is the crystallographic orientation; KDB-0.03 is the brand of boron-doped silicon wafers of resistivity 0.03 Ω cm; $I_g = S_g/S_{sum}$ is the intensity of the Gaussian component and $I_p = S_p/S_{sum}$ is the intensity of the parabolic component in the angular distributions of annihilation photons (S_{sum} is the total area of an experimental angular distribution of annihilation photons, and S_g and S_p are the areas of Gaussian and parabolic components in this spectrum, respectively); and J is current density.

REFERENCES

1. R. M. de la Cruz and R. Pareja, in *Positron Annihilation*, Ed. by L. Dorikens-Vanpraet, M. Dorikens, and D. Segers (World Sci., Singapore, 1989), p. 702.
2. R. Suzuki, T. Mikado, H. Ohgaki, *et al.*, Phys. Rev. B **49**, 17 484 (1994).
3. V. P. Shantarovich, I. B. Kevdina, Yu. A. Novikov, *et al.*, Fiz. Tverd. Tela (St. Petersburg) **38**, 2686 (1996) [Phys. Solid State **38**, 1473 (1996)].
4. Y. Itoh, H. Murakami, and A. Kinoshita, Appl. Phys. Lett. **63**, 2798 (1993).
5. Y. Itoh, H. Murakami, and A. Kinoshita, Hyperfine Interact. **84**, 121 (1994).
6. A. P. Knights, G. Kowalski, A. S. Saleh, *et al.*, J. Appl. Phys. **78**, 4411 (1995).
7. V. I. Grafutin and E. P. Prokop'ev, Usp. Fiz. Nauk **172**, 67 (2002) [Phys. Usp. **45**, 59 (2002)].
8. K. P. Aref'ev, S. A. Vorob'ev, and E. P. Prokop'ev, *Positronics in Radiation Materials Science of Ionic Structures and Semiconductors* (Énergoatomizdat, Moscow, 1983) [in Russian].
9. E. P. Prokop'ev, S. P. Timoshenkov, V. I. Grafutin, *et al.*, *Positronics of Ionic Crystals, Semiconductors, and Metals* (Mosk. Inst. Élektron. Tekh., Moscow, 1999) [in Russian]; http://www.prokopep.narod.ru.
10. V. I. Grafutin, E. P. Prokop'ev, S. P. Timoshenkov, *et al.*, Khim. Fiz. **23** (5), 22 (2004).
11. A. N. Parbukov, V. I. Beklemyshev, V. M. Gontar, *et al.*, Mater. Sci. Eng. C **15** (1–2), 121 (2001).

Translated by V. Makhlyarchuk

JETP Letters, Vol. 81, No. 11, 2005, pp. 551–555. From Pis'ma v Zhurnal Éksperimental'noĭ i Teoreticheskoĭ Fiziki, Vol. 81, No. 11, 2005, pp. 683–687.
Original English Text Copyright © 2005 by Klinkhamer, Volovik.

Merging Gauge Coupling Constants without Grand Unification¶

F. R. Klinkhamer[1] and G. E. Volovik[2, 3]

[1] *Institute for Theoretical Physics, University of Karlsruhe (TH), 76128 Karlsruhe, Germany*
[2] *Low-Temperature Laboratory, Helsinki University of Technology, FIN-02015 HUT, Finland*
[3] *Landau Institute for Theoretical Physics, Russian Academy of Sciences, Moscow, 119334 Russia*
e-mail: frans.klinkhamer@physik.uni-karlsruhe.de, volovik@boojum.hut.fi

Received May 5, 2005

The merging of the running coupling constants of the weak, strong, and electromagnetic fields does not require the unification of these gauge fields at high energy. It can, in fact, be the property of a general fermionic system in which gauge bosons are not fundamental. © *2005 Pleiades Publishing, Inc.*

PACS numbers: 11.10.Hi, 12.10.Kt, 12.60.Re, 67.90.+z, 71.10.–w

1. INTRODUCTION

There are several lessons to be learned from the example of relativistic quantum fields emerging in condensed matter. One of them is that the physical cutoff can be different for bosons and fermions if the fermions are more fundamental than the bosons. This occurs in superfluid ^{3}He–A, where bosons are the collective modes of the fermionic quantum vacuum and are composite objects made of fermionic degrees of freedom [1]. The naive counting of fermionic and bosonic contributions to the vacuum polarization suggests that the antiscreening effect of charged bosons must dominate over the screening effect of the fermionic vacuum and that, therefore, the effective $SU(2)$ gauge field emerging in ^{3}He–A must experience asymptotic freedom [2]. However, this is not what happens in superfluid ^{3}He–A. Instead, the $SU(2)$ coupling constant shows the same zero-charge effect as the Abelian $U(1)$ field.[1] The reason is the difference in cutoff scales for bosons and fermions. As a result, the contribution of the fermions to the logarithmically running coupling constant prevails, in spite of the larger boson content. Actually, the hierarchy of cutoff scales in ^{3}He–A is such that the asymptotic-freedom contribution from the gauge bosons does not develop and the only contribution to the vacuum polarization comes from the fermions.

Another important lesson from condensed-matter physics is that the bare coupling constant is absent for emergent gauge fields of a fermionic quantum vacuum. The reason is simply that such gauge bosons cannot exist as free fields, that is, without having fermions around to make the quantum vacuum. This implies, in particular, that the entire gauge coupling constant comes from vacuum polarization.

Here, we assume that the Standard Model of elementary particle physics also has different physical cutoff scales: the compositeness scale E_c, which provides the cutoff for the gauge bosons, and the much higher ultraviolet cutoff E_{UV} for the fermions. Assuming that all three coupling constants of the Standard Model come exclusively from vacuum polarization, we will find that the most natural choice for the compositeness scale E_c is the Planck scale $E_{\text{Planck}} \approx 10^{19}$ GeV (or, possibly, a scale lower by a factor of about 10^4), while the ultraviolet cutoff scale E_{UV} will turn out to be much larger than the Planck scale.

This second cutoff may be associated with the energy scale where Lorentz invariance is violated, $E_{\text{UV}} \sim E_{\text{Lorentz}}$. It has been claimed [3] that cosmic-ray observations imply $E_{\text{Lorentz}} > 10^{21}$ GeV, assuming the absence of very small numerical factors in the dispersion relations.[2] Probably, E_{Lorentz} is even larger. This would mean that the Planck cutoff is highly Lorentz invariant and that the underlying symmetry of the fundamental structure is itself the Lorentz symmetry, which then protects the Lorentz invariance of the effective low-energy physics [5].

If $E_{\text{Lorentz}} \gg E_{\text{Planck}}$, the topological Fermi-point scenario of emergent relativistic quantum fields may be relevant [1]. Specifically, the integration over fermions with energy $E \lesssim E_{\text{Planck}}$ occurs in the fully relativistic region, where fermions are still close to the Fermi points and, therefore, have gauge invariance and general covariance. As a result, the induced effective action

¶ The text was submitted by the authors in English.

[1] The term "zero-charge effect" refers to the long-distance (infrared) behavior, whereas "asymptotic freedom" refers to the short-distance (ultraviolet) behavior.

[2] An explicit calculation of photon propagation in a static background of randomly positioned wormholes has shown how, in principle, small numerical factors could appear in the photon dispersion relation [4], but this calculation does not apply to fermions.

0021-3640/05/8111-0551$26.00 © 2005 Pleiades Publishing, Inc.

for the gauge and gravity fields is automatically invariant.

The small ratio of cutoff parameters, $E^2_{\rm Planck}/E^2_{\rm Lorentz}$, protects the Lorentz invariance of the known physical laws. This would be in accordance with Bjorken's suggestion [6] that a highly accurate relativistic quantum field theory can only emerge if there is a small expansion parameter in the theory.

The merging of gauge coupling constants at high energy is usually associated with Grand Unification of the weak, strong, and electroweak interactions into a larger gauge group with a single coupling constant [7, 8]. The two-scale scenario discussed in the present Letter demonstrates that the merging of running couplings could occur without unification: it could very well be the natural property of an underlying fermionic vacuum.

2. RUNNING COUPLINGS FROM TWO ENERGY SCALES

Let us assume that the gauge fields of the Standard Model are not fundamental but induced, so that the three running coupling constants g_i of the gauge group $U(1) \times SU(2) \times SU(3)$ only come from vacuum polarization. In other words, the fine-structure constants $\alpha_i \equiv g_i^2/4\pi$, for $i = 1, 2, 3$, are completely determined by logarithms and have vanishing inverse bare values, $1/\alpha_i^{(0)} = 0$.

If gauge bosons are fermion composites, the ultraviolet cutoff scale for the vacuum polarization caused by fermions must be larger than the one caused by gauge bosons. Let $E_{\rm UV}$ be the cutoff for the fermions and $E_{\rm c} \ll E_{\rm UV}$ be the compositeness scale that provides the cutoff energy for the gauge bosons. Then, for energies above the electroweak scale but below the compositeness scale, one has at one loop (see [8, 9])

$$\alpha_1^{-1}(E) = \frac{5N_F}{9\pi}\ln\frac{E^2_{\rm UV}}{E^2}, \tag{1a}$$

$$\alpha_2^{-1}(E) = \frac{N_F}{3\pi}\ln\frac{E^2_{\rm UV}}{E^2} - \frac{11}{6\pi}\ln\frac{E^2_{\rm c}}{E^2}, \tag{1b}$$

$$\alpha_3^{-1}(E) = \frac{N_F}{3\pi}\ln\frac{E^2_{\rm UV}}{E^2} - \frac{11}{4\pi}\ln\frac{E^2_{\rm c}}{E^2}, \tag{1c}$$

for $M_Z \ll E \ll E_{\rm c} \ll E_{\rm UV}$ and using natural units with $\hbar = c = 1$. Here, N_F is the number of fermion families contributing to the screening (zero-charge) vacuum polarization, whereas the antiscreening (asymptotic-freedom) contribution comes from the non-Abelian gauge bosons.

At the compositeness scale $E_{\rm c}$, the weak and strong inverse couplings, as well as the hypercharge inverse coupling with a factor of 3/5, approach the same value:

$$\frac{3}{5}\alpha_1^{-1}(E_{\rm c}) = \alpha_2^{-1}(E_{\rm c}) = \alpha_3^{-1}(E_{\rm c}) = \frac{N_F}{3\pi}\ln\frac{E^2_{\rm UV}}{E^2_{\rm c}}. \tag{2}$$

Above the compositeness scale, the behavior depends on the details of the dynamics. If the gauge bosons break up for $E > E_{\rm c}$, the story ends here, at least as far as the gauge bosons are concerned. If, on the other hand, the gauge bosons survive but for some reason do not contribute to the vacuum polarization, the couplings run together as

$$\frac{3}{5}\alpha_1^{-1}(E) = \alpha_2^{-1}(E) = \alpha_3^{-1}(E) = \frac{N_F}{3\pi}\ln\frac{E^2_{\rm UV}}{E^2}, \tag{3}$$

for $E_{\rm c} \ll E \ll E_{\rm UV}$. As discussed in the Introduction, a similar situation occurs in superfluid ^{3}He–A, with only fermions contributing to the polarization of the vacuum. In this liquid, the running coupling constant of the effective $SU(2)$ field behaves in exactly the same way as that of the Abelian $U(1)$ field; that is, it experiences the same zero-charge effect. Of course, as the couplings α_i from Eq. (3) grow with energy, higher-order contributions need to be added to the logarithm shown (see [9]).

Let us, first, estimate the compositeness scale $E_{\rm c}$. This can be done in the same way as the standard calculation of the unification scale (see [9]), i.e., only using the bosonic contributions to the running couplings. One then obtains, for the compositeness energy scale, the same value as is usually assumed to hold for Grand Unified Theories (GUTs).[3]

Canceling out the fermionic contributions from the right-hand sides of Eqs. (1a)–(1c), one finds two equations at the electroweak scale M_Z:

$$\alpha_2^{-1}(M_Z) - \alpha_3^{-1}(M_Z) = \frac{11}{12\pi}\ln\frac{E^2_{\rm c}}{M_Z^2}, \tag{4a}$$

$$\frac{3}{5}\alpha_1^{-1}(M_Z) - \alpha_2^{-1}(M_Z) = \frac{11}{6\pi}\ln\frac{E^2_{\rm c}}{M_Z^2}. \tag{4b}$$

Extracting the combination $1/\alpha_Q \equiv 1/\alpha_1 + 1/\alpha_2$ from these equations, one obtains Eq. (21.5.16) of [9], which expresses the logarithm in terms of the strong coupling constant α_3 and the fine-structure constant α_Q at the electroweak scale:

$$\ln\frac{E^2_{\rm c}}{M_Z^2} = \frac{2\pi}{11\alpha_Q(M_Z)}\left(1 - \frac{8}{3}\frac{\alpha_Q(M_Z)}{\alpha_3(M_Z)}\right). \tag{5}$$

[3] The reason is that the right-hand sides of Eqs. (1a)–(1c) can be written solely in terms of $\ln(E^2_{\rm c}/E^2)$ and $\tilde{\alpha}^{-1} \equiv N_F/(3\pi)\ln(E^2_{\rm UV}/E^2_{\rm c})$, with $E_{\rm c}$ and $\tilde{\alpha}$ taking the role of the unification energy $E_{\rm GUT}$ and coupling constant $\alpha_{\rm GUT}$.

Taking the numerical values $\alpha_3(M_Z) \approx 0.120$ and $\alpha_Q(M_Z) \approx 1/128$ at $E = M_Z \approx 91.2$ GeV [9], this gives the following estimate:

$$\ln(E_c^2/M_Z^2) \approx 60.4. \quad (6)$$

The compositeness scale E_c is about 10^{15} GeV, which is relatively close to the Planck energy scale $E_{\text{Planck}} \equiv \sqrt{\hbar c^5/G} \approx 1.22 \times 10^{19}$ GeV.

Let us now estimate the ultraviolet cutoff E_{UV} for the fermions. From Eqs. (1a) and (1b), the fine-structure constant α_Q at the electroweak scale reads

$$\alpha_Q^{-1}(M_Z) = \frac{8N_F}{9\pi}\ln\frac{E_{\text{UV}}^2}{M_Z^2} - \frac{11}{6\pi}\ln\frac{E_c^2}{M_Z^2}. \quad (7)$$

Using Eq. (5) to eliminate the compositeness scale E_c, one obtains

$$\ln\frac{E_{\text{UV}}^2}{M_Z^2} = \frac{3\pi}{2N_F\alpha_Q(M_Z)}\left(1 - \frac{2}{3}\frac{\alpha_Q(M_Z)}{\alpha_3(M_Z)}\right). \quad (8)$$

With the numerical values mentioned above, this gives the following estimate:

$$\ln(E_{\text{UV}}^2/M_Z^2) \approx 577/N_F. \quad (9)$$

For $N_F = 3$, one has $\ln(E_{\text{UV}}^2/M_Z^2) \approx 192$, so that $E_{\text{UV}} \approx 10^{44}$ GeV $\gg E_{\text{Planck}}$. For $N_F = 5$, the fermion scale is still larger than the Planck energy by a factor of 10^8. The corresponding running coupling constants are shown in the figure.

We realize, of course, that the renormalization-group Eqs. (1a)–(1c), with numerical values (6) and (9) inserted, give a weak mixing angle at $E = M_Z$ somewhat below the experimental value (see also the figure). Specifically, we find $\sin^2\theta_w \approx 0.203$ instead of the experimental value 0.231 [9]. Alternatively, adding the appropriate bare coupling constants $1/\alpha_i^{(0)}$ to the right-hand sides of Eqs. (1a)–(1c) in order to match the three experimental values at $E = M_Z$, we do not find precisely merging coupling constants at high energy.

For a genuine Grand Unified Theory, the problem is serious and has been addressed in different ways; see, e.g., [10–13] and references therein. But, for a dynamic scenario as ours, the precise definition of the compositeness scale is rather uncertain. The scale can, in fact, be slightly different for the various composite gauge bosons. In other words, the three couplings of our scenario need not merge exactly at one particular energy (for example, two couplings could merge first and the third one later).

The simplest way to model these threshold effects is to replace E_c in Eqs. (1b) and (1c) by E_{c2} and E_{c3}, respectively, where E_{c2} and E_{c3} are assumed to be not more than a few orders of magnitude away from the geometric average $E_c \equiv \sqrt{E_{c2}E_{c3}}$. The experimental values $\alpha_i^{\text{exp}}(M_Z)$ then give $\ln(E_{c2}^2/M_Z^2) \approx 50.5$, $\ln(E_{c3}^2/M_Z^2) \approx 58.0$, and $\ln(E_{\text{UV}}^2/M_Z^2) \approx 557/N_F$. This suggests that the range for threshold effects in E_c may be approximately 10^{13}–10^{15} GeV (which is also clear from the figure by making appropriate shifts of the curves). Note, that, without the grand-unified group, there is no danger of having too-rapid proton decay.

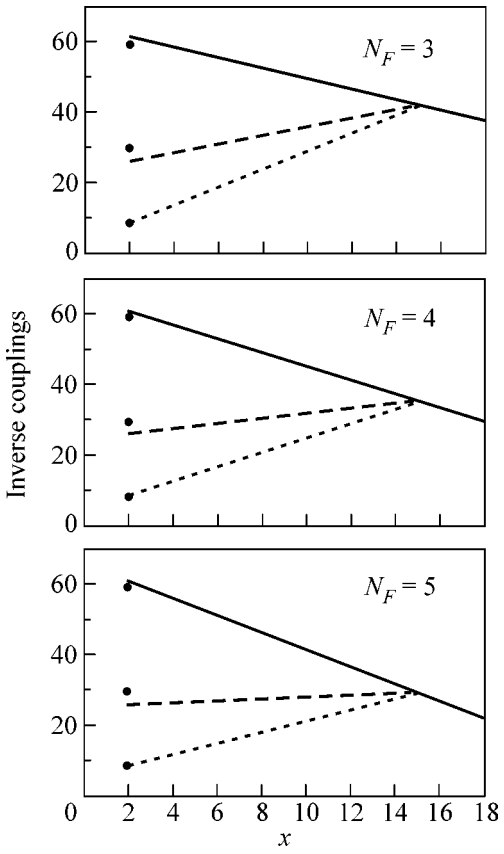

Inverse couplings $(3/5) \times \alpha_1^{-1}$ (solid curve), α_2^{-1} (long-dashed curve), and α_3^{-1} (short-dashed curve), as a function of $x \equiv \log_{10}(E/\text{GeV})$ for different numbers N_F of fermion families. The coupling constants are given by Eqs. (1), (3), (6), and (9), and run together for $E > E_c$ (overlapping curves). At the compositeness scale $E \sim E_c \approx 10^{15}$ GeV, there may be threshold effects that somewhat change the values of the couplings towards lower energies (see text). The dots show the corresponding experimental values at $E = M_Z \approx 91.2$ GeV.

3. DISCUSSION

Let us end with a few general remarks. Trans-Planckian cutoff scales have been considered before, for example, the scale $E_{\text{cutoff}} \approx 10^{42}$ GeV in [14] as corresponding to an exotic (nonexisting) case. The con-

densed-matter-like scenario discussed in the present article suggests, however, that this possibility must be taken seriously.

In this scenario, the merging of the running couplings of weak, strong, and hypercharge fields does not require a unification of these fields at high energy; it may simply be the property of a fermionic system in which gauge bosons are not fundamental. The factor 3/5 for α_1^{-1} in Eq. (3) may indicate an underlying continuous or discrete symmetry between the fermion species.

The large separation between the Planckian (or near-Planckian) compositeness scale E_c and the trans-Planckian scale E_{UV} may be of importance to considerations of the Standard Model symmetries as emergent phenomena. In particular, this allows us to discuss gauge invariance as being an emergent symmetry.

In the topological Fermi-point scenario of emergent relativistic fields [1], the spectrum of fermionic excitations near the Fermi point is linear: fermions are chiral and obey the relativistic Weyl equation. In this scenario, bosonic excitations behave as effective gauge fields interacting with Weyl fermions. This implies that gauge invariance automatically emerges in the fermionic sector close to the Fermi point, i.e., at $E \ll E_{UV}$. The fermions induce gauge invariance for the effective action of the composite vector fields. Since the compositeness cutoff parameter E_c is well below E_{UV}, gauge invariance in the bosonic sector is valid throughout the compositeness scale E_c. Hence, the requirement suggested by Veltman [15] is fulfilled. Specifically, he concluded that, if gauge bosons are composite, gauge invariance should remain valid both in the infrared ($E \ll E_c$) and ultraviolet ($E \gg E_c$) regions. The high accuracy of gauge invariance in the bosonic sector is then determined by the small parameter E_c^2/E_{UV}^2, in accordance with a suggestion by Bjorken [6].

In the Fermi-point scenario, E_{UV} is the scale below which the spectrum of fermionic excitations near the Fermi point is linear, i.e., Lorentz invariance induced by the Fermi point is still obeyed. That is why the Lorentz-violation scale must be approximately equal to or larger than E_{UV}. In turn, this implies that Lorentz invariance is more fundamental than the other physical laws and that we cannot expect to observe its violation in the near future.

Applying the two-scale formalism to gravity, one finds that it gives the wrong value for the gravitational coupling constant. If E_{UV} is again used as the energy cutoff for the fermionic contributions to Newton's constant, one obtains $G^{-1} \sim N_F E_{UV}^2$ instead of $G^{-1} \sim N_F E_{Planck}^2$. It is not clear at the moment how to fix this problem.

We can only speculate that nonlogarithmic (power-law) divergences must be considered with great care. For example, the fourth-order divergence, which leads to a vacuum energy density (cosmological constant Λ) of order E_{UV}^4 or E_{Planck}^4, can be cancelled without fine-tuning, due to the thermodynamic stability of the vacuum [16]. The same may hold for the Higgs mass problem—controlling the quadratically divergent quantum corrections to the Higgs potential mass term (see, e.g., [17]). This cutoff-dependent mass term is simply absorbed by the vacuum energy density and is zero in the equilibrium vacuum, again due to thermodynamic stability [18]. For induced gravity, the cancellation of the vacuum energy density is demonstrated by a calculation of Λ on a (3 + 1)-dimensional brane embedded in AdS_5 space: the induced cosmological constant on the brane vanishes without fine-tuning, thanks to a cancellation of the contributions from (4 + 1)-dimensional fermionic matter and gravity [19].

There may very well be a general principle from the underlying physics, which protects against E_{UV}^n contributions to G^{-1} with $n > 0$. Let us mention, in this respect, another example of induced Sakharov gravity in terms of constituent fields, namely [20], which used such a principle and demonstrated the advantage of two energy scales. In the scheme of [20], the first (lowest) energy scale is the mass scale M' of the constituent fields. With $M' \sim E_{Planck}$, this provides a natural cutoff that determines Newton's constant, $G^{-1} \sim (M')^2 \sim E_{Planck}^2$. The much higher cutoff E'_{UV} drops out from the effective action due to imposed cancellations between the constituent fields (see also [15], where cancellations of fermionic and bosonic effects are required). This scheme only works if Lorentz invariance survives beyond the Planck scale, again in agreement with the statement in [15] that the symmetry should remain valid throughout the cutoff range. The higher cutoff E'_{UV} of [20] must, therefore, be below the Lorentz-violation scale.

In conclusion, it is possible that the scenario of emergent physics, in combination with a hierarchy of cutoff energy scales, can replace the grand-unification scenario based on symmetry breaking. This new scenario (with parameters N_F and $E_c \ll E_{UV}$) naturally leads to the merging of gauge coupling constants, without the need to introduce a simple gauge group (and without having to worry about too-rapid proton decay or excessive magnetic monopoles left over from the early universe).

Moreover, the hierarchy of cutoff energy scales may be related to the well-known hierarchy problem of the Standard Model—the absence of a natural explanation for having $M_Z \ll E_{GUT}$ or E_{Planck} (see, e.g., [15, 17]). The ^{3}He–A example mentioned in the Introduction, where gauge invariance is not fundamental, suggests that the

mass of the weak vector bosons may result not from spontaneous symmetry breaking but from terms depending on the ultraviolet cutoff. If we accept this viewpoint, the typical value of the weak vector boson mass would be $M_Z \sim E_c^2/E_{UV} \ll E_c$, which would be a first step towards understanding the Standard Model hierarchy problem mentioned above (with E_c taking the place of E_{GUT}). From the numerical estimates given in Eqs. (6) and (9) and without further threshold effects at the cutoff energies, the suggested hierarchy would seem to prefer having more than $N_F = 3$ fermion families.

The work of G.E.V. is supported in part by the Russian Ministry of Education and Science, through the Leading Scientific School grant no. 2338.2003.2. This work is also supported by the European Science Foundation COSLAB Program.

REFERENCES

1. G. E. Volovik, *The Universe in a Helium Droplet* (Clarendon, Oxford, 2003).
2. D. J. Gross and F. Wilczek, Phys. Rev. Lett. **30**, 1343 (1973); H. D. Politzer, Phys. Rev. Lett. **30**, 1346 (1973).
3. O. Gagnon and G. D. Moore, Phys. Rev. D **70**, 065002 (2004); hep-ph/0404196.
4. F. R. Klinkhamer and C. Rupp, Phys. Rev. D **70**, 045020 (2004); hep-th/0312032; F. R. Klinkhamer and C. Rupp, hep-ph/0506071.
5. J. Collins, A. Perez, D. Sudarsky, *et al.*, Phys. Rev. Lett. **93**, 191301 (2004); gr-qc/0403053; A. Corichi and D. Sudarsky, gr-qc/0503078.
6. J. D. Bjorken, *Emergent Gauge Bosons*, contributed to *4th Workshop on What Comes Beyond the Standard Model?* (Bled, Slovenia, 2001); hep-th/0111196.
7. H. Georgi and S. L. Glashow, Phys. Rev. Lett. **32**, 438 (1974).
8. H. Georgi, H. R. Quinn, and S. Weinberg, Phys. Rev. Lett. **33**, 451 (1974).
9. S. Weinberg, *The Quantum Theory of Fields II* (Cambridge Univ. Press, Cambridge, 1996).
10. S. Dimopoulos and H. Georgi, Nucl. Phys. B **193**, 150 (1981); S. Dimopoulos, S. Raby, and F. Wilczek, Phys. Rev. D **24**, 1681 (1981); L. E. Ibanez and G. G. Ross, Phys. Lett. B **105B**, 439 (1981).
11. U. Amaldi, W. de Boer, and H. Fürstenau, Phys. Lett. B **260**, 447 (1991); P. Langacker and N. Polonsky, Phys. Rev. D **47**, 4028 (1993); hep-ph/9210235.
12. R. N. Mohapatra and M. K. Parida, Phys. Rev. D **47**, 264 (1993); hep-ph/9204234; D. G. Lee, R. N. Mohapatra, M. K. Parida, and M. Rani, Phys. Rev. D **51**, 229 (1995); hep-ph/9404238.
13. Y. Kawamura, Prog. Theor. Phys. **105**, 691 (2001); hep-ph/0012352.
14. L. V. Laperashvili, H. B. Nielsen, and D. A. Ryzhikh, Int. J. Mod. Phys. A **18**, 4403 (2003); hep-th/0211224; C. R. Das and L. V. Laperashvili, hep-ph/0503138.
15. M. Veltman, Acta Phys. Pol. B **12**, 437 (1981).
16. G. E. Volovik, Ann. Phys. (Leipzig) **14**, 165 (2005); gr-qc/0405012.
17. S. Pokorski, *Phenomenological Guide to Physics Beyond the Standard Model*, Lectures given at *NATO Advanced Study Institute and EC Summer School on String Theory: From Gauge Interactions to Cosmology* (Cargése, France, 2004); hep-ph/0502132.
18. G. E. Volovik, in *I. Ya. Pomeranchuk and Physics at the Turn of the Century*, Ed. by A. Berkov, N. Narozhny, and L. Okun (World Sci., Singapore, 2003), p. 234; hep-ph/0306011.
19. A. A. Andrianov, V. A. Andrianov, P. Giacconi, and R. Soldati, hep-th/0503115.
20. V. P. Frolov, D. V. Fursaev, and A. I. Zelnikov, Nucl. Phys. B **486**, 339 (1997); hep-th/9607104.

JETP Letters, Vol. 81, No. 11, 2005, pp. 556–560. Translated from Pis'ma v Zhurnal Éksperimental'noĭ i Teoreticheskoĭ Fiziki, Vol. 81, No. 11, 2005, pp. 688–692.
Original Russian Text Copyright © 2005 by Kopitsa, Grigoriev, Runov, Maleyev, Garamus, Yashenkin.

Study of the Heavy-Fermion Compound $CeRu_2Si_2$ by the Small-Angle Neutron Scattering Method

G. P. Kopitsa[1], S. V. Grigoriev[1], V. V. Runov[1], S. V. Maleyev[1], V. M. Garamus[2], and A. G. Yashenkin[1]

[1] *Petersburg Nuclear Physics Institute, Russian Academy of Sciences, Gatchina, 188300 Russia*
e-mail: kopitsa@mail.pnpi.spb.ru
[2] *GKSS Research Centre, D-21502 Geesthacht, Germany*

Received May 11, 2005

In order to directly observe neutron scattering by heavy fermion quasiparticles at low temperatures, a $CeRu_2Si_2$ single crystal has been studied by the small-angle neutron scattering method. In the experiment, neutron scattering is observed at $T = 0.85$ K for momentum transfers $q \le 0.04$ Å^{-1}, which is treated as the orbital component of magnetic scattering by heavy fermion quasiparticles. It has been found that the application of a magnetic field $H = 1$ T leads to both an increase in the observed scattering and its anisotropy with respect to the field direction. Moreover, measurements in the magnetic field reveal additional scattering for $q > 0.04$ Å^{-1}, which is well described by a Lorentzian and is interpreted as neutron magnetic scattering by spin-density fluctuations with a correlation radius $R_c \approx 30$ Å. © *2005 Pleiades Publishing, Inc.*

PACS numbers: 61.12.Ex, 71.27.+a

As was shown in theoretical works [1–3], the orbital part of the amplitude of neutron magnetic scattering contains the term

$$F_{\text{sing}} = -ir\frac{\boldsymbol{\sigma}[\mathbf{q}\times\mathbf{p}]}{q^2}, \quad (1)$$

which is singular at $q \longrightarrow 0$. Here, $r = |\gamma|e^2/mc^2 = 5.4 \times 10^{-13}$ cm, $\gamma = -1.91$ is the neutron magnetic moment measured in nuclear magnetons, $\boldsymbol{\sigma}$ is the vector composed of the Pauli matrices, $\mathbf{q} = \mathbf{k}_i - \mathbf{k}_f$ is the neutron momentum transfer ($\mathbf{k}_i$ and $\mathbf{k}_f$ are the neutron momenta before and after scattering, respectively), and $\mathbf{p}$ is the electron momentum operator. Therefore, small-angle neutron scattering by conduction electrons is predicted to occur with the cross section [1–3]

$$\Sigma(q) = \frac{3n_0r^2k_iN}{2p_F\vartheta V}\left(\frac{m^*}{M_n}\right)^2\begin{cases}1; & 2E_n\vartheta \gg T\\ T/2E_n\vartheta; & 2E_n\vartheta \ll T.\end{cases} \quad (2)$$

Here, N is the number of the unit cells per volume V of a scatterer, n_0 is the number of conduction electrons per unit cell, m^* is the effective mass of electrons, M_n is the neutron mass, p_F is the Fermi momentum, $\vartheta \ll 1$ is the scattering angle, T is the scatterer temperature, and E_n is the neutron energy. According to Eq. (2), the scattering cross section is determined by the factor $(m^*/M_n)^2$, which is on the order of 10^{-5}–10^{-6} for the standard metals and, thereby, neutron–electron scattering is negligibly small. However, for heavy fermion compounds, $m^* \approx 100m_e$ [4] and $(m^*/M_n)^2 \sim 10^{-2}$. In this case, this scattering can be detected. The crossover from one scattering regime to the other is expected at $\vartheta_c \cong T/2E_n$. This crossover proceeds because scattering at $2E_n\vartheta \ll T$ occurs on thermally excited quasiparticles, whereas thermal excitation is immaterial for $2E_n\vartheta \gg T$.

In view of gauge invariance [5], if electrons (movable charge carriers) in a metal are subjected to a uniform magnetic field $\mathbf{H}$, Eq. (1) should be rewritten as

$$F_{\text{sing}} = -ir\frac{\boldsymbol{\sigma}\left[\mathbf{q}\times\left(\mathbf{p}-\frac{e}{c}\mathbf{A}_\mathbf{q}\right)\right]}{q^2}. \quad (3)$$

Here, $\mathbf{A}_\mathbf{q}$ is the Fourier transform of the vector potential $\mathbf{A} = \frac{1}{2}[\mathbf{B}\times\mathbf{r}]$, where $\mathbf{B}$ is the magnetic induction inside the sample. Taking into account the Fourier transform, we obtain the additional term in Eq. (3) in the form

$$F_H \propto \frac{\boldsymbol{\sigma}[\mathbf{q}\times[\mathbf{B}\times\mathbf{q}]]}{q^4} = \frac{\boldsymbol{\sigma}(\mathbf{B}q^2-(\mathbf{B}\mathbf{q})\mathbf{q})}{q^4} = \frac{\boldsymbol{\sigma}\mathbf{B}_\perp}{q^2}. \quad (4)$$

In this case, the following term arises in the scattering cross section:

$$\Sigma_H(q) = \Sigma_0\left(\frac{\frac{e}{c}B_\perp}{p_Fk_i\vartheta}\right)^2\begin{cases}2/3; & 2E_n\vartheta \gg T\\ 2T/3E_n\vartheta; & 2E_n\vartheta \ll T,\end{cases} \quad (5)$$

where $\Sigma_0 = (3n_0r^2k_iN/2p_F\vartheta V)(m^*/M_n)^2$. Moreover, according to Eq. (4), this scattering is anisotropic, is strongest for $\mathbf{q} \perp \mathbf{B}$, and is absent for $\mathbf{q} \parallel \mathbf{B}$.

The scattering under consideration is very weak. For this reason, its observation requires, first, the existence of heavy fermion quasiparticles with a sufficiently large effective mass $m^* \geq 100m_e$ in the scattering system and, second, the absence of additional sources of both magnetic and nuclear scattering in this system at temperatures on the order of 1 K. In this work, small-angle neutron scattering (SANS) experiments were carried out with a $CeRu_2Si_2$ single crystal in order to directly observe SANS on heavy fermion quasiparticles and to analyze the magnetic field effect on this scattering.

1. Samples and measurement procedure. The intermetallic system $CeRu_2Si_2$, which has a body-centered tetragonal $ThCr_2Si_2$-type structure with the lattice constants $a = b = 4.197$ Å and $c = 9.797$ Å [6], is a typical heavy fermion compound with the Kondo temperature $T_K \leq 20$ K and Sommerfeld constant $\gamma = C/T \approx$ 350 mJ mol^{-1} K^{-2} near $T \approx 1$ K [7, 8]. The $CeRu_2Si_2$ compound is in a paramagnetic state down to $T \approx$ 20 mK [9]. At the same time, inelastic neutron scattering experiments on $CeRu_2Si_2$ single crystals [6, 10] have revealed the existence of short-range antiferromagnetic correlations with a range of about three lattice constants at temperatures $T \leq 20$ K. A magnetic field $H_m = 7.8$ T suppresses these correlations, and the system undergoes a metamagnetic transition from the paramagnetic to the ferromagnetic state [6]. According to experiments on the de Haas–van Alfvén effect [11, 12], the effective mass of quasiparticles reaches $200m_e$. The $CeRu_2Si_2$ single crystal was grown in a three-arc furnace using Czochralski's method [6].

The SANS measurements were performed for two wavelengths, namely, $\lambda_1 = 8.1$ Å and $\lambda_2 = 10.5$ Å, at the SANS-1 facility (FRG1 reactor, GKSS Research Centre, Geesthacht, Germany) [13], which operated in a geometry close to point geometry. The use of three sample–detector distances SD = 0.7, 1.8, and 4.5 m made it possible to conduct measurements in the momentum transfer range $1.1 \times 10^{-2} < q < 2.1 \times 10^{-1}$ Å^{-1}. Scattered neutrons were detected by a 2D position-sensitive ^{3}He detector.

The sample was mounted in a cryostat, and measurements were carried out at two temperatures, namely, $T = 0.85$ and 293 K. Long-term stabilization of the sample was better than ≈0.01 K. The external magnetic field H created by a cryomagnet varied from 0 to 1 T. The single crystal was oriented such that the (001) axis was perpendicular to both the incident neutron beam and the applied magnetic field H.

The raw spectra for each q interval were corrected to scattering by both the cryostat and the setup equipment, as well as to the room background, using the standard procedure [14]. The measured 2D spectra were reduced to the absolute scale by normalization to the cross section for incoherent neutron scattering by 1 mm of H_2O taking into account the detector efficiency [14].

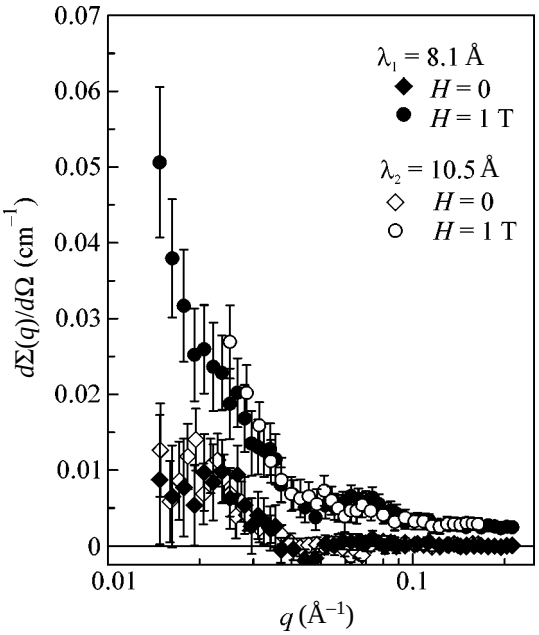

Fig. 1. Momentum transfer dependences of the scattering cross section $d\Sigma(q)/d\Omega$ measured at $T = 0.85$ K (diamonds) in the absence of magnetic field and (circles) in a magnetic field $H = 1$ T for neutron wavelengths (closed symbols) $\lambda_1 = 8.1$ Å and (open symbols) $\lambda_2 = 10.5$ Å.

The low-temperature scattering intensity I_s analyzed in this work was calculated as the excess over nuclear scattering, which is taken as scattering by the sample at room temperature, $T_r = 293$ K:

$$I_s(q) = I(T, q) - I(T_r, q)R. \quad (6)$$

Here, $R = I(T = 0.85\text{ K}, 0)/I(T = 293\text{ K}, 0)$ is the neutron transmission coefficient. The scattering intensity component induced by the magnetic field was determined as

$$I_H(q) = I(H, q) - I(H = 0, q)R1, \quad (7)$$

where $R1 = I(H = 1\text{T}, 0)/I(H = 0, 0)$.

2. Measurement results. The momentum dependences of the SANS cross section $d\Sigma(q)/d\Omega$ measured at $T = 0.85$ K in the absence of magnetic field and in a magnetic field $H = 1$ T are shown in Fig. 1 for neutron wavelengths $\lambda_1 = 8.1$ Å and $\lambda_2 = 10.5$ Å. As is seen in this figure, low-temperature scattering in the absence of a magnetic field occurs at both λ values for $q \leq q_0 \approx$ 0.04 Å^{-1}. This scattering intensity is very low (about 10^{-2} cm^{-1} at $q \approx 0.015$ Å^{-1}) but is statistically significant and increases as q decreases. The scattering cross section estimated for $q = 0.015$ Å^{-1} by Eq. (2) with the parameters $n_0 = 1$, $(m^*/M_n)^2 \approx 0.012$, $N \approx 5.85 \times 10^{20}$, $V = 0.05$ cm^3, and $p_F = (3\pi^2 n_0 N_a/V_m)^{1/3} \approx 0.64$ Å^{-1} ($N_a = 6.022 \times 10^{23}$ mol^{-1} and $V_m = 51.7$ cm^3 mol^{-1}) is equal to

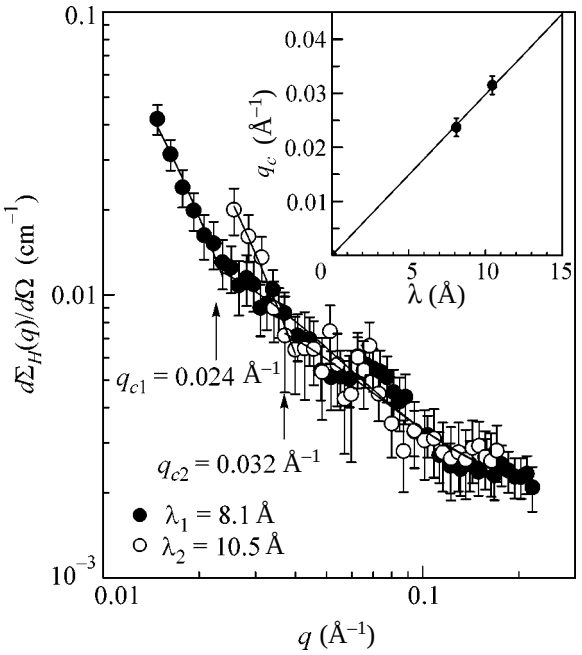

Fig. 2. Momentum transfer dependences of the cross section $d\Sigma_H(q)/d\Omega$ for scattering induced by the magnetic field H = 1 T as measured for neutron wavelengths (closed circles) λ_1 = 8.1 Å and (open circles) λ_2 = 10.5 Å. The dashed and solid lines are obtained by formulas (10) and (11), respectively. Inset: λ dependence of q_c.

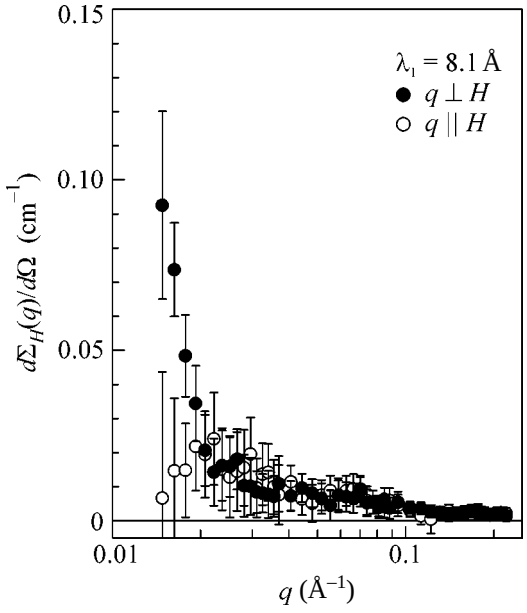

Fig. 3. Momentum transfer dependences of the scattering cross section $d\Sigma_H(q)/d\Omega$ with the momentum transfers (open circles) parallel and (closed circles) perpendicular to the magnetic field H = 1 T for λ_1 = 8.1 Å.

$d\Sigma(q)/d\Omega \approx 0.6 \times 10^{-2}$ and 0.5×10^{-2} cm^{-1} for λ_1 and λ_2, respectively. As is clearly seen (Fig. 1), these estimates nearly coincide with experimental data for $d\Sigma(q)/d\Omega$.

The presence of the magnetic field H = 1 T gives rise to a strong increase in the scattering cross section and to the appearance of additional scattering for $q > q_0$, which has a diffuse but pronounced maximum at $q \approx 0.067$ Å^{-1}.

The momentum dependences of the cross section $d\Sigma_H(q)/d\Omega$ for scattering induced by a magnetic field that are obtained using Eq. (6) for both wavelengths are shown in Fig. 2 on the log–log scale. As is clearly seen in this figure for both cases, there are two q ranges where $d\Sigma_H(q)/d\Omega$ behaves as q^{-n} with different n values. The exponent $n \approx 4$ and 2 for $q \le q_{c1,\,c2}$ and $q \ge q_{c1,\,c2}$, respectively (where $q_{c1} \approx 0.024$ Å^{-1} and $q_{c2} \approx 0.032$ Å^{-1} for λ_1 and λ_2, respectively, are the crossover points from one scattering regime to the other). The inset in Fig. 2 shows q_c versus λ. This dependence is evidently approximated by the following linear dependence $q_c(\lambda)$ shown by the solid straight line:

$$q_c = 2k\sin(\vartheta_c/2) \approx k(T/2E_n) \approx 0.0038T\lambda, \qquad (8)$$

where $k = 2\pi/\lambda$, $E_n = 81.81/\lambda^2$, and $\vartheta_c = T/2E_n$. We note that the sample temperature estimated from this dependence is equal to $T_{ex} = 0.95 \pm 0.07$ K, which nearly coincides with the actual sample temperature $T = 0.85 \pm 0.01$ K.

Such a behavior of the scattering cross section $d\Sigma_H(q)/d\Omega$, along with the E_n dependence of q_c, completely corresponds to the theoretically predicted properties of SANS given by Eq. (5) on movable carriers in the magnetic field. We emphasize that the data presented in Figs. 1 and 2 are azimuthally averaged in order to achieve better statistical accuracy. However, according to Eq. (4), the magnetic-field-induced part of the cross section for neutron–electron scattering is expected to depend as $\sin^4\alpha$ on the angle α between the magnetic field **H** and the momentum transfer **q**.

The momentum dependences of the scattering cross section $d\Sigma_H(q)/d\Omega$ with the momentum transfers (open circles) parallel and (closed circles) perpendicular to the magnetic field H are shown in Fig. 3 for λ_1 = 8.1 Å. As is clearly seen, for $q < q_{c1}$, $d\Sigma_H(q)/d\Omega$ behaves differently for neutrons with **q** perpendicular and parallel to the magnetic field. In this q range, scattering induced by the field exhibits a sharp increase for $\mathbf{q} \perp \mathbf{H}$, whereas it decreases almost to zero for the case $\mathbf{q} \parallel \mathbf{H}$ as q decreases. The observed scattering is almost isotropic for $q > q_{c1}$. We note that a similar behavior of $d\Sigma_H(q)/d\Omega$ is observed for λ_2 = 10.5 Å.

Figure 4 shows the α dependences of the scattering cross section $d\Sigma_H(q)/d\Omega$ that are obtained for two different momentum transfers $q_1 = 0.018$ Å$^{-1} < q_c$ and $q_2 = 0.03$ Å$^{-1} > q_c$. As is seen in this case, the scattering cross

section α depends on the angle α only for $q < q_c$, whereas it remains almost constant for $q > q_c$. It has been found that the α dependence of α for q_1 is well approximated by the formula

$$\frac{d\Sigma_H(q, \alpha)}{d\Omega} = C\sin^4\alpha - D\sin^2\alpha + I_{iso}, \quad (9)$$

where C and D are free parameters and I_{iso} is a constant that is independent of the angle α and is associated with isotropic scattering by spin-density fluctuations (see below).

As was mentioned above, the cross section $d\Sigma_H(q)/d\Omega$ behaves differently for $q < q_c$ and $q > q_c$. It has been found that the momentum dependence of $d\Sigma_H(q)/d\Omega$ for small q values at both wavelengths is well reproduced by the expression

$$\frac{d\Sigma_H(q)}{d\Omega} = \frac{A_1}{q^4}, \quad (10)$$

where $A_1 = (A_0 q_c^4)/E_n$ is the scattering amplitude and A_0 is a free parameter, which is necessarily proportional to the magnetic field squared according to Eq. (5).

We emphasize that these results (q and α dependences of $d\Sigma_H(q)/d\Omega$ for $q < q_c$) completely agree with the theoretical assumptions concerning the properties of neutron–electron scattering in the magnetic field.

The behavior of $d\Sigma_H(q)/d\Omega$ for large q values is well described by the Lorentzian

$$\frac{d\Sigma_H(q)}{d\Omega} = \frac{A_2}{q^2 + \kappa^2} + I_{inc}, \quad (11)$$

where $\kappa = 1/R_c$ is the inverse correlation radius, A_2 is a free parameter, and I_{inc} is a constant that is independent of q and is associated with scattering by objects with sizes smaller than or on the order of the wavelength of neutrons incident on the sample. As is well known, Eq. (11) is used to describe magnetic scattering by thermodynamic spin-density fluctuations such as critical fluctuations in ferromagnets above T_C [15]. According to [6, 10], antiferromagnetic correlations are observed in the paramagnetic compound $CeRu_2Si_2$ at temperatures $T \le 20$ K and magnetic fields $H < H_m = 7.8$ T. The average magnetic moment of a paramagnetic system at $H = 0$ is $M = \langle m_i \rangle = 0$ (where $m_i = \langle S_i \rangle$ is the magnetic moment of an atom), and scattering by spin-density fluctuations is absent. The application of the magnetic field leads to the appearance of a nonzero mean magnetic moment in the system and creates the magnetic contrast $\Delta\rho = \rho_m - \langle\rho_m\rangle$ (where ρ_m and $\langle\rho_m\rangle$ is the local and average spin densities of the scattering lengths in the system) between antiferromagnetic correlations with $\langle m_i \rangle = 0$ (zero "holes") and the paramagnetic matrix with $M \neq 0$. This behavior means that additional scattering induced by the field for $q > q_c$ can be attributed to the spin part of the magnetic scattering amplitude.

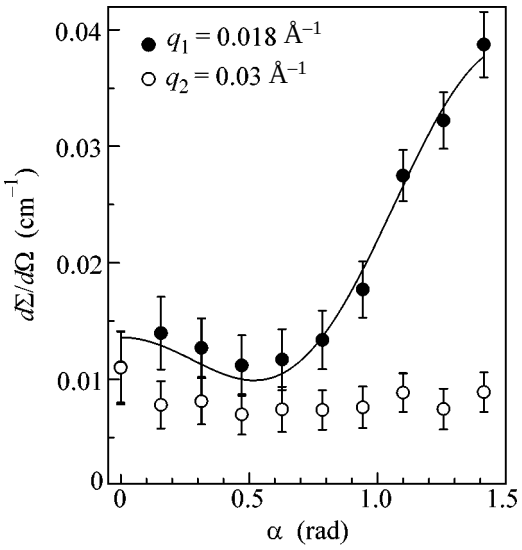

Fig. 4. Scattering cross section $d\Sigma_H(q)/d\Omega$ vs. the angle α between the magnetic field **H** and momentum transfer **q** for (closed circles) $q_1 = 0.018$ Å^{-1} and (open circles) $q_2 = 0.03$ Å^{-1}. The solid line is the calculation by Eq. (9).

To obtain the final results, Eqs. (10) and (11) were convolved with the resolution function of the facility, which is approximated by a Gaussian. Experimental data for $d\Sigma_H(q)/d\Omega$ are processed by the least-square method in the ranges $q \in$ 0.015–0.22 and 0.025–0.17 Å^{-1} for λ_1 and λ_2, respectively. The processing results are

The lsm fit parameters for the scattering cross section $d\Sigma_H(q)/d\Omega$

Wavelength λ (Å)	Range q (Å^{-1})	Scattering law $\sim q^{-4}$	Lorentzian		
		A_1 (×10^{-8} cm^{-1})	A_2 (×10^{-5} cm^{-1})	$R_c = 1/\kappa$ (Å)	I_{inc} (×10^{-2} cm^{-1})
8.1	0.015–0.023	0.24 ± 0.03		–	
	0.024–0.22	–	1.66 ± 0.5	31 ± 12	0.167 ± 0.06
10.5	0.025–0.032	1.07 ± 0.18		–	
	0.034–0.17	–	1.44 ± 0.8	28 ± 12	0.205 ± 0.055

presented in the table and shown in Fig. 2 by the solid and dashed lines.

CONCLUSIONS

The SANS experiment with the $CeRu_2Si_2$ single crystal reveals the following properties.

(i) Small-angle neutron scattering occurs at $T = 0.85$ K and $H = 0$ for momentum transfers $q \le 0.04$ Å^{-1} and, according to theoretical predictions [3] and our estimates of $d\Sigma(q)/d\Omega$, can be associated with the orbital part of magnetic scattering by heavy fermion quasiparticles.

(ii) The application of the magnetic field $H = 1$ T leads both to an increase in the observed scattering and its anisotropy with respect to the field direction.

(iii) Measurements in the magnetic field reveal additional scattering for $q > 0.04$ Å^{-1}, which is well described by a Lorentzian and is interpreted as neutron magnetic scattering by spin-density fluctuations with a correlation radius $R_c \approx 30$ Å.

We are grateful to S. Raymond for kindly placing the sample at our disposal, to A.I. Okorokov for continuous interest in the work, and to D.Yu. Chernyshev for stimulating discussions. This work was supported by the Russian Foundation for Basic Research (project nos. 04-02-16342, 03-02-17340, and 00-15-96814); by the Russian programs "Quantum Macrophysics," "Strongly Correlated Electrons in Semiconductors, Metals, Superconductors, and Magnetic Materials," and "Neutron Investigations of Matter;" by the Council of the President of the Russian Federation for Support of Young Russian Scientists and Leading Scientific Schools (project no. NSh-1671.2003.2); and Russian State Contract no. 40.012.1.1.1149.

REFERENCES

1. R. J. Elliott, Proc. R. Soc. London, Ser. A **235**, 298 (1956).
2. S. L. Ginzburg and S. V. Maleyev, Fiz. Tverd. Tela (Leningrad) **7**, 3063 (1965) [Sov. Phys. Solid State **7**, 2477 (1965)].
3. S. V. Maleyev, Usp. Fiz. Nauk **172**, 617 (2002) [Phys. Usp. **45**, 569 (2002)].
4. G. R. Stewart, Rev. Mod. Phys. **56**, 755 (1984).
5. L. D. Landau and E. M. Lifshitz, *Course of Theoretical Physics*, Vol. 5: *Statistical Physics*, 3rd ed. (Nauka, Moscow, 1982; Pergamon, Oxford, 1986), Part 1.
6. L. P. Regnault, W. A. Erkelens, J. Rossat-Mignod, *et al.*, Phys. Rev. B **38**, 4481 (1988).
7. M. J. Besnus *et al.*, Solid State Commun. **5**, 779 (1985).
8. R. A. Fisher, C. Marcenat, N. E. Phillips, *et al.*, J. Low Temp. Phys. **84**, 49 (1991).
9. D. Takahashi, S. Abe, H. Mizuno, *et al.*, Physica B (Amsterdam) **329–333**, 489 (2003).
10. M. Sato *et al.*, ISSP Report (Tokyo, 1997).
11. H. Aoki, S. Uji, A. K. Albessard, and Y. Onuki, Phys. Rev. Lett. **71**, 2110 (1993).
12. S. R. Julian, F. S. Tautz, G. J. McMullan, and G. G. Lonzarich, Physica B (Amsterdam) **199–200**, 63 (1994).
13. H. B. Shuhrmann, N. Burkhardt, G. Dietrich, *et al.*, Nucl. Instrum. Methods Phys. Res. A **356**, 133 (1995).
14. G. D. Wignall and F. S. Bates, J. Appl. Crystallogr. **20**, 28 (1986).
15. S. V. Maleyev and V. A. Ruban, Zh. Éksp. Teor. Fiz. **62**, 416 (1972) [Sov. Phys. JETP **35**, 222 (1972)].

Translated by R. Tyapaev

JETP Letters, Vol. 81, No. 11, 2005, pp. 561–566. From Pis'ma v Zhurnal Éksperimental'noĭ i Teoreticheskoĭ Fiziki, Vol. 81, No. 11, 2005, pp. 693–698.
Original English Text Copyright © 2005 by Cattani, Anderson, Kim, Lisak.

Formation of Bose–Einstein Condensate Structures in Laser Fields: Semiclassical Approach and Electrodynamic Effects¶

F. Cattani[1], D. Anderson[1], A. V. Kim[2], and M. Lisak[1]

[1] *Department of Electromagnetics, Chalmers University of Technology, SE-412 96 Göteborg, Sweden*
[2] *Institute of Applied Physics, Russian Academy of Sciences, Nizhni Novgorod, 603950 Russia*

Received April 7, 2005

The formation of Bose–Einstein condensate (BEC) structures via electromagnetically induced interactions is analyzed within a semiclassical approach, wherein an improved interaction potential is obtained. This analysis shows how the laser-induced forces can lead to self-confinement of the ground state even with a homogeneous field. It furthermore indicates that the vector character of the field can be crucially important, since it can change the type of nonlinearity, thus strongly modifying the BEC structures. © *2005 Pleiades Publishing, Inc.*

PACS numbers: 03.75.Fi, 34.20.Cf, 34.80.Qb

BACKGROUND

Recently, the nonlinear behavior of Bose–Einstein condensates (BEC) in laser fields has become a subject of growing attention (see, e.g., [1–3] and references therein), inspired both by new perspectives in the study of BEC in optical lattices and by new possibilities of having a BEC self-localized in space via laser-induced interactions when the atoms are released from a trap. Since most of the experiments on Bose–Einstein condensation have been accurately described by the mean-field method based on the Gross–Pitaevskii equation (GPE) [4], extensions of this equation are also used for describing BEC in optical fields. However, so far the potential energy of the interaction has been modeled as the single-particle ponderomotive potential in problems of optical lattices or as a sum of the laser-induced dipole–dipole interatomic potentials (see, for example, [3] or [5]).

The purpose of the present work is to provide a general approach for describing the laser-induced interaction of Bose–Einstein condensates where the difference between the local field (the microscopic field acting on an atom) and the macroscopic field (the field averaged over a volume containing many atoms) is taken into account. Of particular interest is the investigation of the formation of BEC structures created via interactions where the nature and stability of a Bose condensed state are influenced by the self-induced dipole–dipole interaction forces. This analysis provides us with qualitatively new regimes for the formation of condensate structures. To this purpose, we consider an extension of the GPE by using a semiclassical approach for describing the self-induced forces (striction forces) in the laser-condensate interaction. For a large number of atoms, this description can be significantly simplified by using the macroscopic electrodynamics approach. This analysis also shows that the vector character of the field can be crucially important. For instance, for BEC structures well-localized within a laser wavelength along the field, variations of the dielectric permittivity strongly influence the microscopic field, thus qualitatively changing the type of nonlinearity.

SEMICLASSICAL APPROACH

The dipole–dipole interactions of a BEC in laser fields as well as in static fields have recently been investigated within the framework of quantum theory [5–8]. For models with different effective interaction potentials, simple cases of density modulations and atomic beam guiding have been investigated. The full quantum description is based on the exact Hamiltonian, but, for the conditions of interest in laser-condensate interactions and for large laser detunings from the atomic resonance, a semiclassical model can be derived, wherein the atoms are described by a Schrödinger equation with the interaction term given by the self-induced force calculated in the framework of macroscopic electrodynamics. For a high-frequency field, the averaged induced force per volume, **f**, in transparent media can be obtained as shown in [9] by time averaging of the corresponding electrostriction force in a static electric field [10]. For a zero-temperature, dilute BEC in a far-off-resonant laser field $\mathrm{Re}[\mathbf{E}\exp(-i\omega t)]$, we have (see [9])

$$\mathbf{f} = \frac{n}{16\pi}\nabla\left[|\mathbf{E}|^2\frac{\partial\varepsilon}{\partial n}\right], \qquad (1)$$

¶ The text was submitted by the authors in English.

0021-3640/05/8111-0561$26.00 © 2005 Pleiades Publishing, Inc.

where n is the condensate atom density and ε is the dielectric permittivity of the condensate gas. To describe the striction forces, we have to find a suitable model for ε. Since we assume a large number of condensate particles in a volume λ^3 (λ is the laser wavelength), the dielectric constant can be modeled in the local-field approach, where, for atomic gases, the difference between the local field acting on an atom and the macroscopic field formed by the induced dipoles of the surrounding particles is taken into account (see, for example, [11]). This gives

$$\varepsilon = 1 + \frac{4\pi\alpha n}{1 - (4\pi/3)\alpha n}, \quad (2)$$

where $\alpha = -d^2/\hbar\Delta$ is the atomic polarizability at the laser frequency, with $\Delta = \omega - \omega_a$ being the detuning from the nearest atomic resonance frequency ω_a, and d is the dipole matrix element of the resonant transition. By substituting Eq. (2) into Eq. (1), we obtain the total force acting on a single atom, $\mathbf{F} = \mathbf{f}/n = -\nabla V_d$, where the corresponding potential energy is given by

$$V_d = -\frac{\alpha}{4}\frac{|\mathbf{E}|^2}{(1 - (4\pi/3)\alpha n)^2}. \quad (3)$$

For a single particle ($n = 0$), Eq. (3) describes the ponderomotive force in an inhomogeneous laser beam. However, even in a homogeneous laser field, the force does not vanish, since it may also be generated by the presence of density gradients. As is easily seen, in the low-density limit (or in the weak dipole interaction limit, $4\pi\alpha n/3 \ll 1$), the striction force originating from the induced microscopic dipole–dipole interatomic forces is an attractive force independent of the sign of the frequency detuning, i.e., $V_d \propto -\alpha^2 n$. Although, at first glance, the low-density approximation seems to describe most of the experiments, the structural dynamics and the subsequent density modulations will, in fact, depend on the character of the nonlinearity, i.e., on the sign of the detuning.

SELF-CONFINED BEC

We consider a condensate with repulsive interaction (the s-wave scattering length $a > 0$). The above result implies that the dynamics of the BEC atoms in a laser field can be described by a generalized GPE for the condensate wavefunction $\Psi(\mathbf{r}, t)$ [4]:

$$i\hbar\frac{\partial\Psi}{\partial t} = \hat{H}_0\Psi + \left[U_0|\Psi|^2 - \frac{\alpha}{4}\frac{|\mathbf{E}|^2}{(1 - (4\pi/3)\alpha|\Psi|^2)^2}\right]\Psi, \quad (4)$$

where $\hat{H}_0$ is the linear single-particle Schrödinger Hamiltonian; the wavefunction Ψ is normalized as $N = \int|\Psi|^2 d\mathbf{r}$, with N denoting the total number of atoms, so that the gas density is $n = |\Psi|^2$, $U_0 = 4\pi\hbar^2 a/m$, and m is the atom mass. In Eq. (4), the laser-induced nonlinearity originates from the difference between the macroscopic and local fields in a condensate gas and bears a local character, since, for fixed orientation and separation of the dipoles, the interaction energy for a large number of atoms in a physical volume averaged over the relative positions of the dipoles vanishes (see, e.g., [11]). This is consistent with the approach used in [6], where a phenomenological dipole–dipole interaction is assumed to be in the form of a contact potential, rather than with the model used in [3, 5], where the main contribution is due to the long-range interaction. As a first approximation in the low-density limit, the self-confining dynamics does not depend on the sign of α and, when the interparticle interaction is dominated by the dipole–dipole forces, i.e., for laser intensities such that

$$|\mathbf{E}|^2 > \mathrm{E}_{\mathrm{th}}^2 = \frac{3U_0}{2\pi\alpha^2} = \frac{6\hbar^4 a\Delta^2}{md^4}, \quad (5)$$

the dynamics may result in a density modulation of the condensate ground state and even a tendency towards a subsequent collapselike evolution that usually takes place only in the presence of attractive s-wave interactions [12, 13]. However, the question of what kind of structures the condensate will actually realize must be answered by using exact Eq. (4) and, in fact, the evolution will essentially depend on the sign of the laser frequency detuning. In order to clarify this question, we consider the case of a constant (homogeneous) laser field E = const and restrict our analysis to the steady-state regime, where we can assume $\Psi(\mathbf{r}, t) = \psi(\mathbf{r})\exp(-iEt/\hbar)$. Without an external potential, Eq. (4) reduces to

$$\left[-\frac{\hbar^2}{2m}\nabla^2 + U_0\psi^2 - \frac{\alpha}{4}\frac{|\mathbf{E}|^2}{\left(1 - \frac{4\pi}{3}\alpha\psi^2\right)^2}\right]\psi = E\psi, \quad (6)$$

where ∇^2 is the Laplace operator and E is the ground state energy of the Bose condensate, which depends also on the total number of condensate atoms. It is obvious that, due to the focusing nature of the induced dipole–dipole interaction nonlinearity, there are continuous families of symmetrical localized solutions of Eq. (6) for any space dimensionality. However, since the validity of a model with a constant field, as we will see below, depends on the orientation of the density gradients, we will here pay particular attention to 3D axisymmetrical and 1D cases.

In 1D, Eq. (6) is similar to that which describes particle motion in the effective potential $V_e(\psi) = -U_0\psi^4 + (\alpha/2)|\mathbf{E}|^2\psi^2/(1 - (4\pi/3)\alpha\psi^2) + 2E\psi^2$. From this analogy, all possible condensate distributions can be inferred from the phase portraits of the system. This is shown in Fig. 1 for the different parameters for which localized

solutions exist. The main bifurcation inequality when a localized BEC can occur is given by Eq. (5). If the laser intensity exceeds this threshold, self-confined states can occur for any number of atoms, as seen in Figs. 1a and 1c, where the separatrix curve passing through zero corresponds to localized solutions. For weak nonlinearity, the bound state has the shape of the Schrödinger soliton, $\psi(x) \simeq \sqrt{2\tilde{E}/\tilde{\delta}U_0}\,\mathrm{sech}(\sqrt{2m\tilde{E}}x/\hbar)$ (where $\tilde{E} = -E - E_c > 0$, $E_c = \alpha|\mathbf{E}|^2/4$, $\tilde{\delta} = (|\mathbf{E}|^2/E_{\mathrm{th}}^2) - 1 > 0$), with the total number of atoms $N = \sqrt{2\tilde{E}/m}\,(2\hbar/\tilde{\delta}U_0)$ decreasing with decreasing $\tilde{E}$. In fact, the qualitative behavior of the localized solutions does not depend on the sign of α. However, as we will see below, the sign of α is important for the problem of stability, which originates from the singularity in the interaction potential for red frequency detuning ($\alpha > 0$), where the condensate distributions become narrower for an increasing number of atoms, in contrast to the case of blue detuning ($\alpha < 0$), where the condensate distributions become flatter due to the saturation behavior of the nonlinearity.

If the inequality given by Eq. (5) is not fulfilled, self-bound states of the BEC do not exist for $\alpha < 0$. However, for red detuning ($\alpha > 0$), topologically the same phase portrait takes place if the number of condensate atoms exceeds some critical value (see Fig. 1a). This critical number of atoms corresponds to the case when the ground energy of the condensate is equal to $E = -E_c$, which can be found by direct integration of Eq. (6). In a case that may be verified experimentally, when laser intensities are near the threshold level, i.e., $0 < \delta = 1 - (|\mathbf{E}|^2/E_{\mathrm{th}}^2) \ll 1$, the ground-state distribution is self-organized into the form

$$\psi_*(x) \simeq \sqrt{\frac{3\delta}{4\pi\alpha}}\frac{1}{1+\gamma^2x^2}, \qquad (7)$$

where $\gamma = (\delta/\hbar)\sqrt{3mU_0/4\pi\alpha}$. This solution contains a critical number of atoms, N_*, which does not depend on δ:

$$N_* = \int_{-\infty}^{\infty}\psi_*^2(x)dx \simeq \sqrt{\frac{3\pi\hbar^2}{4mU_0\alpha}}. \qquad (8)$$

In a 3D geometry, N_* plays the role of the atom surface density.

It is interesting to note that Eq. (6) not only has purely localized solutions ($\psi \longrightarrow 0$ at $x \longrightarrow \pm\infty$) but also describes localized solutions on a homogeneous condensate background, as a dark soliton corresponding to the separatrix curve from the equilibrium point A to $-A$ (Figs. 1b, 1c, and 1d) and as a hump (compressed) field in the condensate (closed separatrix around the equilibrium point B in Fig. 1b). If the dark soliton in Fig. 1d can be considered as a generalized version of the well-known solution also observed experimentally (see, for instance, in [14]), the others represent new solutions indicating that new types of collective excitations can be produced in laser-condensate interactions.

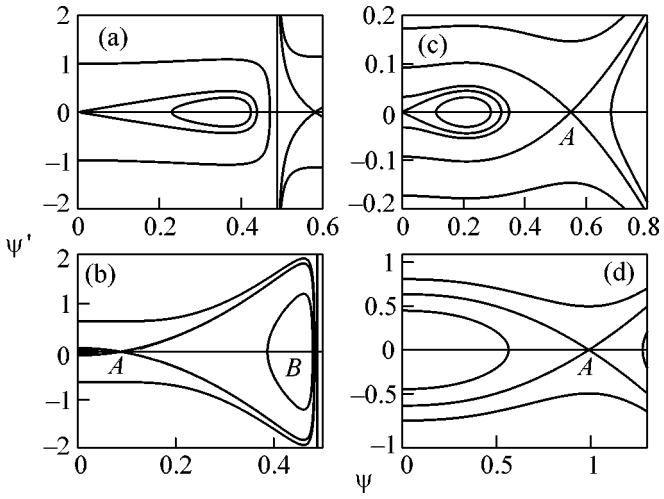

Fig. 1. Phase portrait for Eq. (6) for different regimes when the self-confinement of the ground state can occur (symmetrical with respect to the axis ψ'): (a) $\alpha > 0$, $E < -E_c$, for any number of condensate atoms if $|\mathbf{E}|^2 > E_{\mathrm{th}}^2$ and otherwise for $N > N_*$; (b) $\alpha > 0$, $E > -E_c$ and $|\mathbf{E}|^2 < E_{\mathrm{th}}^2$; (c) $\alpha < 0$, $|\mathbf{E}|^2 > E_{\mathrm{th}}^2$; and (d) $\alpha < 0$, $|\mathbf{E}|^2 < E_{\mathrm{th}}^2$. The dashed line indicates the singularity point in the potential energy $V_e(\psi^2)$.

The important role of the sign of α is clearly seen for axisymmetric BEC structures that occur if the total number of atoms exceeds a critical number, which can easily be calculated by expanding the potential function in the low-density limit, where the ground-state solution is the so-called Townes mode [12, 15]. Equation (6) admits localized solutions for any sign of the detuning. However, it is obvious that, for positive α, such solutions are unstable against collapse. This is in accordance with the stability criterion of Kolokolov and Vakhitov [16]. The ground state is unstable when the total number of atoms is an increasing function of the energy $\delta N/\delta E > 0$, as seen in Fig. 2a. Otherwise, it is stable (Fig. 2b) due to the saturation-type nonlinearity. Thus, for $\alpha > 0$, condensates tend to collapse and can produce even a condensed-matter state. It should be noted that one-dimensional states may also be unstable against collapse due to the singularity in the potential energy (see, for example, [17]) and, therefore, quasi-1D condensed-matter structures can also be formed.

Thus, for experimental realization of the predicted self-confined effects, it is sufficient that the laser intensity exceeds the threshold given by Eq. (5). For ^{87}Rb and ^{23}Na atoms and linearly polarized light with a fre-

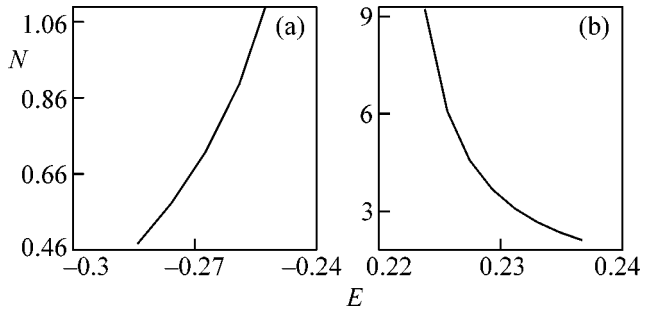

Fig. 2. Dependence of the total number of atoms in the self-confined BEC structure on the ground-state energy at $|\mathbf{E}|^2 > E_{\text{th}}^2$ for positive (a) and negative (b) α. All quantities are dimensionless.

quency detuning of 0.95 GHz from the $^2S_{1/2}$–$^2P_{3/2}$ atomic resonance (irrespective of the sign of the detuning), the threshold intensity is equal to 130 mW/cm^2 and 900 mW/cm^2, respectively. However, it should be noted that, below this threshold, the density modulation can also occur for red detuning ($\alpha > 0$) only if the total number of atoms exceeds the critical value $N = N_* S$, where S is the transverse cross section (see Eq. (8)). For the same parameters, N_* is equal to 4.7×10^{11} cm^{-2} and 7×10^{11} cm^{-2}. For example, for $S = 10 \times 10$ μm, $N = 4.7 \times 10^5$ and 7×10^5 for Rb and Na condensates, respectively.

Notice that, in the model we have presented, all absorption processes were neglected, a legitimate assumption provided that the laser detuning Δ is so large compared with the spontaneous emission rate γ_o (e.g., for Na $\gamma_o/2\pi \simeq 10$ MHz) that the imaginary part of the dielectric permittivity can be considered negligibly small. In this case, the effect of resonance absorption on the BEC density modulations is small but will define the lifetime of these structures. However, even if the laser detuning was chosen to be large enough, i.e., $\Delta \gg \gamma_o$, resonance absorption could come into play due to photoassociation, which can be an effective mechanism of excitation of the high-lying vibrational levels of an excited molecule created from two atoms during a collisional process [18]. However, as was recently experimentally shown in almost-pure condensates, a photoassociation spectrum is quite narrow [19, 20]. At the laser intensities presented in the above estimates, the photoassociation linewidth would be approximately twice the atomic linewidth corresponding to the low-intensity limit, where it is independent of intensity. For higher intensities, the linewidth is broadened (and also shifted) linearly with the intensity up to a maximum of 60 MHz at 1 kW/cm^2 for Na. We note that this intensity value is three orders of magnitude higher than that in our estimates. Thus, our estimates show that, by choosing appropriate laser detunings, we are able to avoid the photoassociation absorption or even to use it for effectively creating highly vibrationally excited molecules by employing the considered BEC density modulations.

ELECTRODYNAMIC EFFECTS AND 3D LIMITS OF SMALL-SCALE STRUCTURES

So far, we have considered the problem of BEC structures in a given laser field. However, in general, Eq. (4) must be considered self-consistently together with Maxwell's equations, which determine the dynamics of the electromagnetic radiation. The condensate density modulations may affect the electromagnetic field propagation and, as a consequence, the self-consistent interaction may exhibit features that differ from what was predicted in the first part of this work. Thus, we will concentrate now on the possible back-effects of BEC density modulations on the electromagnetic field. In particular, we will show that, if the density gradient is along the electric field, the corresponding variations in the dielectric permittivity can strongly influence the microscopic field and may even change the character of the nonlinear effects.

To gain insight into this effect, we consider the structural dynamics of a condensate that is well localized within a laser wavelength. In this case, we can use the following as a governing equation for the field [11]:

$$\nabla(\varepsilon \mathbf{E}) = 0. \tag{9}$$

The evolution of condensates in electromagnetic fields within the framework of Eqs. (2), (4), and (9) may be referred to as quasi-electrostatic BEC dynamics. First of all, the characteristic scales of the density modulations can be obtained from the problem of structural stability of the background state against small perturbations. We assume the background state to be homogeneous: $\Psi = \Psi_0 \exp(-iE_0 t/\hbar)$; $\mathbf{E} = \mathscr{E}_0 \mathbf{e}_y$; and the relation between Ψ_0, E_0, and $\mathscr{E}_0$ is given by the algebraic equation $E_0 = U_0 \Psi_0^2 - \alpha \mathscr{E}_0^2 / [4(1 - 4\pi\alpha\Psi_0^2/3)^2]$. The latter also defines the equilibrium points in Fig. 1. We introduce the electrostatic potential, $\mathbf{E} = -\nabla\varphi$, which implies that Eq. (9) becomes $\varepsilon\nabla^2\varphi + (\nabla\varepsilon\nabla\varphi) = 0$. By linearizing the basic set of equations for small perturbations, i.e., writing $\Psi = [\Psi_0 + u_1(\mathbf{r}, t) + iv_1(\mathbf{r}, t)]\exp(-iE_0 t/\hbar)$, $\varphi = -\mathscr{E}_0 \mathbf{y} + \varphi_1(\mathbf{r}, t)$, where u_1, v_1, φ_1 are assumed to be real functions, we arrive at a set of linear equations. For solutions of the form $u_1, v_1, \varphi_1 \propto e^{\Gamma t - i\kappa \mathbf{r}}$, the growth rate is given by

$$\Gamma = \frac{\kappa}{\sqrt{2m}} \times \left\{ \left[\frac{4\pi\alpha^2 \mathscr{E}_0^2 (1 - 3\kappa_y^2/\kappa^2 \tilde{\varepsilon}_0)}{3(1 - (4\pi)3\alpha\Psi_0^2)^3} - 2U_0 \right] \Psi_0^2 - \frac{\hbar^2 \kappa^2}{2m} \right\}^{1/2}, \tag{10}$$

where $\kappa^2 = \kappa_x^2 + \kappa_y^2 + \kappa_z^2$ and $\tilde{\varepsilon}_0 = 1 + (8\pi/3)\alpha\Psi_0^2$. The growth rate reaches its maximum at $\kappa_y = 0$, i.e., for condensate density modulations extended along the electric field and well localized in the perpendicular direction.

The most striking new feature of the self-consistent interaction between the condensate modulation and the electromagnetic radiation is that modulations along the field are strongly suppressed, whereas, in the first part of this work, fully localized structures were found when only the condensate dynamics was included. The nature of such a behavior can be understood by considering a simplified model that assumes 1D density variations in a specific geometry. More specifically, we assume the laser field to be homogeneous (on the scale of the wavelength) and the density gradients to be along the direction of the field. Thus, the model equation for the BEC dynamics is rewritten by coupling it to the governing equation for the electromagnetic radiation. This model is built to describe exactly the conditions under which we have found, from Eq. (10), that no localized BEC structure along the field direction should be formed. While the result of Eq. (10) comes from the general model of Eqs. (4) and (9), we will now focus on a simpler model describing only the 1D case of density modulations parallel to the field. The aim is to understand how the nonlinear interaction is modified in this case and why localized structures are suppressed.

For linearly polarized light, Eq. (9) implies that the macroscopic field generated inside the condensate is given by

$$\mathbf{E}(x, t) = \frac{\mathbf{E}_L}{\varepsilon(x, t)}, \tag{11}$$

where $\mathbf{E}_L = \mathrm{E}_L\mathbf{e}_x$ is the laser field. Substituting Eq. (11), with the dielectric permittivity given by Eq. (2), into Eq. (3), we arrive at the following governing equation:

$$i\hbar\frac{\partial\Psi}{\partial t} = \hat{H}_0\Psi + \left[U_0|\Psi|^2 - \frac{\alpha}{4}\frac{\mathrm{E}_L^2}{(1 + (8\pi/3)\alpha|\Psi|^2)^2}\right]\Psi \tag{12}$$

which models the simplified case of density modulations parallel to the laser electric field, so that it differs from the general model (Eq. (4)) for the simplifying assumptions between Eq. (11). Equation (12) is thus intended to shed light on the more general result obtained from the full model and contained in Eq. (10) on the effects of density gradients parallel to the vector electric field. As is easily seen in the low-density limit, the interaction energy is $V_d^{nl} \simeq 8\pi\alpha^2\mathrm{E}_L^2|\Psi|^2/3 > 0$, which leads to a defocusing nonlinearity, as for repulsive interaction between particles, independently of the sign of α.

Thus, Eq. (12) shows the effects of density modulations along the direction of the field. These density modulations induce variations of the dielectric constant, which then affect the electromagnetic field.

It turns out that this effect is of the same order of magnitude as that due to the induced dipole–dipole interaction. In fact, it is strong enough to give rise to a different type of nonlinearity. Apart from a family of localized dark soliton-like solutions, which can be excited as collective excitations, an analysis of the steady-state solutions of Eq. (12) shows that there are no localized humplike solutions for the case of density modulations along the electric field. This means that, in the general 3D case, along the direction of the laser field, self-localized states can be generated only over a length scale comparable to or larger than the laser wavelength. However, as follows from Eqs. (4) and (10), in any other direction, the focusing nature of the nonlinearity can lead to the formation of narrower density distributions. Consequently, the evolution of a BEC affected by laser-induced interactions in a linearly polarized field may result in a self-organized cigar-shaped bound state extended along the field.

In conclusion, we have presented an analysis of the density modulations of a BEC produced via laser-induced forces, and we have shown that, by modifying easily controllable parameters, such as the laser intensity, frequency detuning and field polarization, different self-confined condensate structures can be accomplished. Furthermore, we have investigated the self-consistent back-reaction of atom density modulations on the electromagnetic field and have found that, when the vector nature of the field is taken into account, spatial localization over a wavelength scale along the electric field is inhibited, though it is still possible in the transverse direction.

REFERENCES

1. G. Kalosakas, K. Ø. Rasmussen, and A. R. Bishop, Phys. Rev. Lett. **89**, 030402 (2002).
2. M. Kramer, L. Pitaevskii, and S. Stringari, Phys. Rev. Lett. **88**, 180404 (2002).
3. S. Giovanazzi, D. O'Dell, and G. Kurizki, Phys. Rev. Lett. **88**, 130402 (2002); D. O'Dell *et al.*, Phys. Rev. Lett. **84**, 5687 (2000).
4. F. Dalfovo *et al.*, Rev. Mod. Phys. **71**, 463 (1999).
5. S. Yi and L. You, Phys. Rev. A **61**, 041604 (2000); K. Goral, K. Rzazewski, and T. Pfau, Phys. Rev. A **61**, 051601 (2000); L. Santos *et al.*, Phys. Rev. Lett. **85**, 1791 (2000).
6. G. Lenz, P. Meystre, and E. M. Wright, Phys. Rev. Lett. **71**, 3271 (1993).
7. W. Zhang, D. F. Walls, and B. C. Sanders, Phys. Rev. Lett. **72**, 60 (1994); J. Ruostekoski and J. Javanainen, Phys. Rev. A **56**, 2056 (1997); H. Wallis, Phys. Rev. A **56**, 2060 (1997); L. V. Krutitsky, F. Burgbacher, and J. Audretsch, Phys. Rev. A **59**, 1517 (1999).
8. M. Saffman, Phys. Rev. Lett. **81**, 65 (1998).

9. L. P. Pitaevskii, Sov. Phys. JETP **39**, 1008 (1961).
10. L. D. Landau and E. M. Lifshitz, *Electrodynamics of Continuous Media* (GIFML, Moscow, 1959; Pergamon, New York, 1960).
11. J. D. Jackson, *Classical Electrodynamics*, 2nd ed. (Wiley, New York, 1975; Inostrannaya Literatura, Moscow, 1965).
12. E. V. Shuryak, Phys. Rev. A **54**, 3151 (1996).
13. R. A. Duine and H. T. C. Stoof, Phys. Rev. Lett. **86**, 2204 (2001).
14. J. Denschlag *et al.*, Science **287**, 97 (2000); B. P. Anderson *et al.*, Phys. Rev. Lett. **86**, 2926 (2001).
15. R. Y. Chiao, E. Garmire, and C. H. Townes, Phys. Rev. Lett. **13**, 479 (1964).
16. N. G. Vakhitov and A. A. Kolokolov, Radiophys. Quantum Electron. **16**, 783 (1975).
17. N. E. Kosmatov, V. F. Shvets, and V. E. Zakharov, Physica D (Amsterdam) **52**, 16 (1991).
18. J. Weiner, V. S. Bagnato, S. Zilio, and P. S. Julienne, Rev. Mod. Phys. **71**, 1 (1999).
19. C. McKenzie *et al.*, Phys. Rev. Lett. **88**, 120403 (2002).
20. I. D. Prodan *et al.*, Phys. Rev. Lett. **91**, 080402 (2003).

JETP Letters, Vol. 81, No. 11, 2005, pp. 567–570. Translated from Pis'ma v Zhurnal Éksperimental'noĭ i Teoreticheskoĭ Fiziki, Vol. 81, No. 11, 2005, pp. 699–702.
Original Russian Text Copyright © 2005 by Vasnetsov, Pas'ko, Soskin.

Spatial Dependence of the Frequency Spectrum of a Rotating Optical Beam

M. V. Vasnetsov*, V. A. Pas'ko, and M. S. Soskin

Institute of Physics, National Academy of Sciences of Ukraine, Kiev, 03028 Ukraine

** e-mail: mvas@iop.kiev.ua*

Received April 25, 2005

A rotating optical beam displaced relative to the rotational axis becomes polychromatic due to the rotational Doppler effect. The case where the initial beam has the form of a superposition of two Laguerre–Gauss modes and carries an elementary image in the form of an asymmetric intensity distribution is considered. The spatial distribution of the monochromatic components in the beam cross section is determined. © *2005 Pleiades Publishing, Inc.*

PACS numbers: 42.15.Dp, 42.25.Fx

The vibrational frequency in a monochromatic optical beam, e.g., the lowest transverse mode of laser radiation (Gaussian beam), is independent of the spatial coordinate in the beam cross section. However, if the beam is set in rotation by means of a deflecting element (in this case, the beam moves in space over a conical or cylindrical surface), the optical frequency is split into a symmetric spectrum due to the rotational Doppler effect (RDE) [1]. The splitting between the neighboring spectral components is equal to the rotational frequency Ω of the deflecting element; in other words, components with frequencies $\omega \pm \Omega, \pm 2\Omega, \pm 3\Omega, \ldots$ appear in the spectrum around the optical frequency ω. The RDE is associated with the existence of the orbital angular momentum (OAM) [2] for beams with a helicoidal wavefront, for which the phase is expressed in terms of the azimuth angle φ as $m\varphi$, where m is an integer (orbital number) [3]. The OAM per photon has a quantized value $m\hbar$ [4]. In the optical range, the RDE was detected when a Gaussian beam was transformed into a beam with an analogous phase dependence on a rotating spiral zone plate [5]. Since the beam deflected from the rotational axis can be represented in the form of a superposition of axial azimuthal harmonics, each of these harmonics acquires the corresponding frequency shift as a result of beam rotation.

Azimuthal harmonics are solutions of the scalar wave equation in the paraxial approximation (e.g., in the form of the Laguerre–Gauss (LG) modes). A peculiar feature of the RDE spectrum is that its shape is determined by the radial coordinate measured from the rotational axis, because each harmonic has its own radial amplitude distribution, and its contribution to the spectrum being measured is determined by the radial position of the measurement point [6].

In this work, we consider the azimuthal dependence of the RDE spectrum of a rotating displaced beam. The beam under study is taken in the form of a superposition of two LG modes with the initially nonzero OAM of one of the components. It should be noted that the RDE spectrum of such a beam (but without displacement from the rotational axis) was measured experimentally in [6].

Beam rotation is shown schematically in Fig. 1. The beam is displaced parallel to itself when it passes through an inclined transparent plane-parallel plate. The rotation of the plate about the axis of the incident beam leads to the motion of the transmitted beam over a cylindrical surface. An analogous scheme is shown for a version with beam reflection in an optical element that displaces and rotates the beam.

The parallel displacement of the beam (LG mode) in its constriction can be written in the form of the transformation

$$E(x, y) = E_{\mathrm{LG}}\left[\frac{(x - x_0) + i(y - y_0)}{w_0}\right]^l \times \exp\left[-\frac{(x - x_0)^2 + (y - y_0)^2}{w_0^2}\right], \quad (1)$$

where E_{LG} is the amplitude parameter of the mode, l is the azimuthal mode index, w_0 is the beam dimension in the waist, and x_0 and y_0 are the coordinates of the beam axis displacement. Expanding the exponential term in polar coordinates (ρ, φ), we obtain

$$E(\rho, \varphi) = \frac{E_{\mathrm{LG}}}{w_0^l}(\rho e^{i\varphi} - \delta e^{i\theta})^l \exp\left(-\frac{\rho^2 + \delta^2}{w_0^2}\right) \times \sum_{m=-\infty}^{\infty} I_m\left(\frac{2\rho\delta}{w_0^2}\right)\exp[im(\varphi - \theta)], \quad (2)$$

0021-3640/05/8111-0567$26.00 © 2005 Pleiades Publishing, Inc.

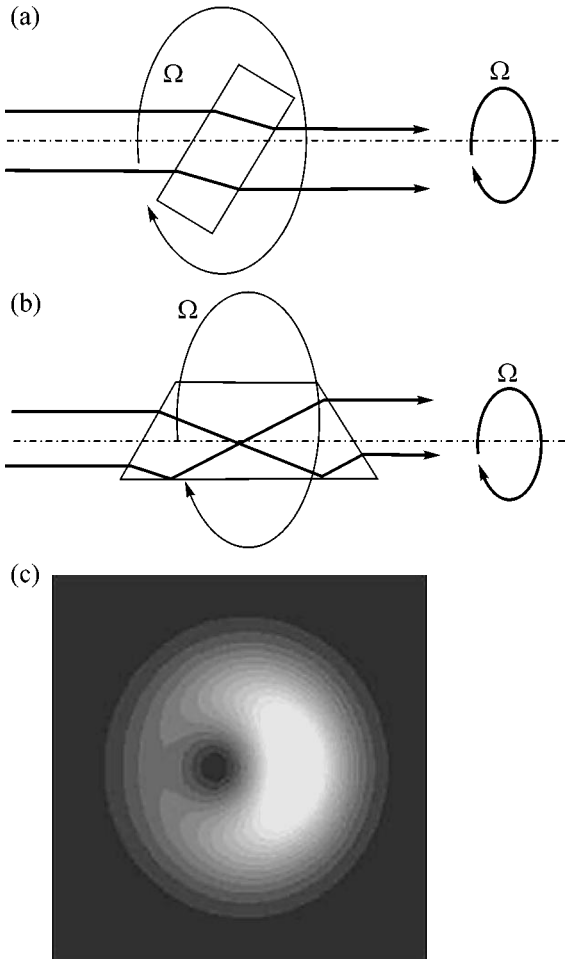

Fig. 1. Schemes of optical beam rotation using an optical element: (a) for parallel displacement without reflection; (b) for parallel displacement with reflection; and (c) the intensity distribution in the beam cross section for the superposition of the Gaussian beam and the LG_0^1 mode has the form of an off-axis dip in which an optical vortex is localized.

where $\delta = (x_0^2 + y_0^2)^{1/2}$ is the parallel displacement of the beam, θ is the azimuthal angle of displacement, and I_m is the modified Bessel function of integer order m [7].

To analyze the frequency spectrum of a rotating beam, we represent it in the form of a superposition of axial components,

$$E(\rho, \varphi) = \sum_{m=-\infty}^{\infty} A_{ml}(\rho, \delta)\exp[im\varphi - i(m-l)\theta], \quad (3)$$

where each component is an azimuthal harmonic

$$A_{ml}(\rho, \delta) = \frac{E_{\mathrm{LG}}}{w_0^l}\exp\left(-\frac{\rho^2+\delta^2}{w_0^2}\right) \times \sum_{n=0}^{l} C_l^n \rho^n (-\delta)^{l-n} I_{m-n}\left(\frac{2\rho\delta}{w_0^2}\right) \quad (4)$$

(C_l^n is the binomial coefficient). Thus, parallel displacement of the beam with orbital number l leads to the emergence of a superposition of beams with orbital numbers m. The rotation of an off-axis beam, which is specified by a continuous variation of the angle $\theta = \Omega t$, produces a frequency shift $(m - l)\Omega$ for each mth component. It follows from formula (3) that the frequency shift appears when the photon OAM changes and is proportional to the difference between the orbital numbers of the azimuthal harmonic and the original beam. The method of decomposing a displaced beam into azimuthal harmonics and the results of its application are described in [1].

If the original beam is a superposition of the lowest (Gaussian, $l = 0$) mode and the LG_0^1 mode ($l = 1$) with a phase difference $\Delta\Phi$ between them, the resultant beam has an asymmetric intensity distribution (Fig. 1c). Such a beam can serve as an example of an elementary optical image. As a result of beam displacement, each mode generates its own spectrum of OAM components (3), and the corresponding OAM components interfere in the displaced beam. It is interesting to note that the OAM of each beam component separately does not change under the parallel displacement of the beam, but the resultant OAM of the displaced beam in the case of the superposition is a function of the phase difference $\Delta\Phi$ between constituent LG modes as well as of the azimuth angle and displacement. This means that the optical element receives a certain angular momentum from the beam.

In accordance with formula (3), OAM components with different orbital numbers acquire the same frequency shift. Superposition of beams with different azimuthal dependences of the phase leads to a complex structure of the distribution of spectral radiation components, which depends on both the radial coordinate and the azimuth angle.

The expression for the monochromatic component with frequency $\omega + m\Omega$ has the form

$$E_{m\Omega}(\rho, \varphi) = A_{m0}(\rho, \delta)\exp[im(\varphi - \Omega t) + i\Delta\Phi] + A_{(m+1)1}(\rho, \delta)\exp[i(m+1)\varphi - im\Omega t], \quad (5)$$

where the first and second components originate from the spectrum of the displaced Gaussian beam and the spectrum of the displaced LG mode, respectively. The result is a superposition of several beams containing optical vortices [8]. Figure 2 shows the form of the intensity distribution for three monochromatic components and their phase portraits in the beam cross section. The positions of optical vortices are shown by dark points (intensity zeros); on the phase portraits, these positions coincide with the points of convergence of phase contours. The parameters of the calculations are $E_G = 0.5$, $E_{\mathrm{LG}} = 1$, $\delta = 0.5w_0$, and $\Delta\Phi = 0$.

In the case of beam displacement with reflection, the OAM of the beam does not change for the Gaussian

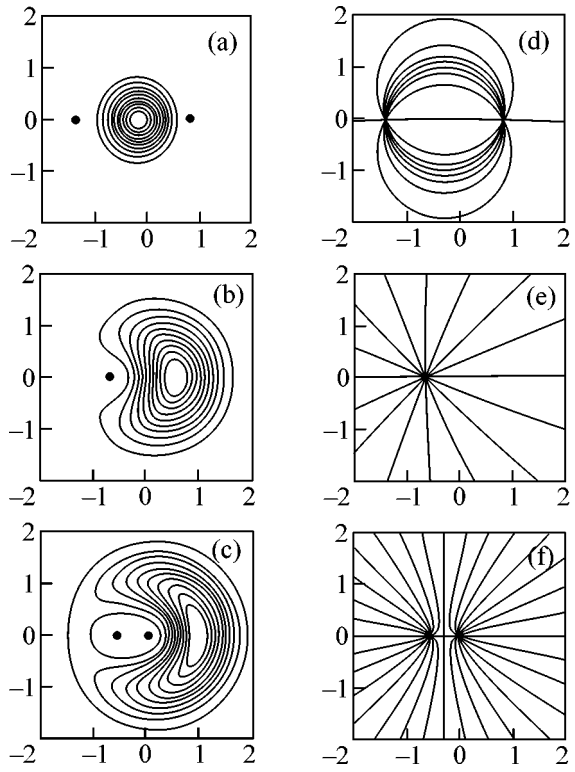

Fig. 2. Contour lines show the intensity distribution in several monochromatic components with frequencies (a) $\omega - \Omega$; (b) ω; and (c) $\omega + \Omega$. Intensity zeros are shown by points. The corresponding phase portraits of the beams show the presence of (d) two opposite optical vortices, (e) a single off-axis optical vortex, and (f) two optical vortices of the same sign with a saddle point between them. The step between phase contours is $\pi/8$. Transverse dimensions on the axes are given in units of the waist parameter w_0.

component, but it is inverted for the LG component. This behavior is due to the fact that the sign of the orbital quantum number is reversed as a result of wave reflection [8]. For zero transverse displacement, the frequency shift is equal to $-2l\Omega$ and to $-(m + l)\Omega$ for the OAM component in the case of beam displacement. For the monochromatic component with the frequency $\omega - m\Omega$, the amplitude distribution acquires the form

$$E_{-m\Omega}(\rho, \varphi) = A_{m0}(\rho, \delta)\exp[im(\varphi - \Omega t) + i\Delta\Phi] + A_{(m-1)1}(\rho, \delta)\exp[i(m-1)\varphi - im\Omega t]. \quad (6)$$

Figure 3 illustrates the calculation of the spectra (intensity of monochromatic components) for various points relative to the rotational axis of the beam at azimuth angles 0°, 90°, and 180° and the radial coordinate $\rho = 0.5w_0$. The computation parameters are $E_G = 1$, $E_{LG} = 3$, $\delta = 0.5w_0$, and $\Delta\Phi = 0$.

The physical meaning of the appearance of the RDE spectrum is that the angular momentum is transferred from the beam to the optical element when the OAM of the optical beam changes. As a result of rotation of the element, work is done and energy exchange takes place

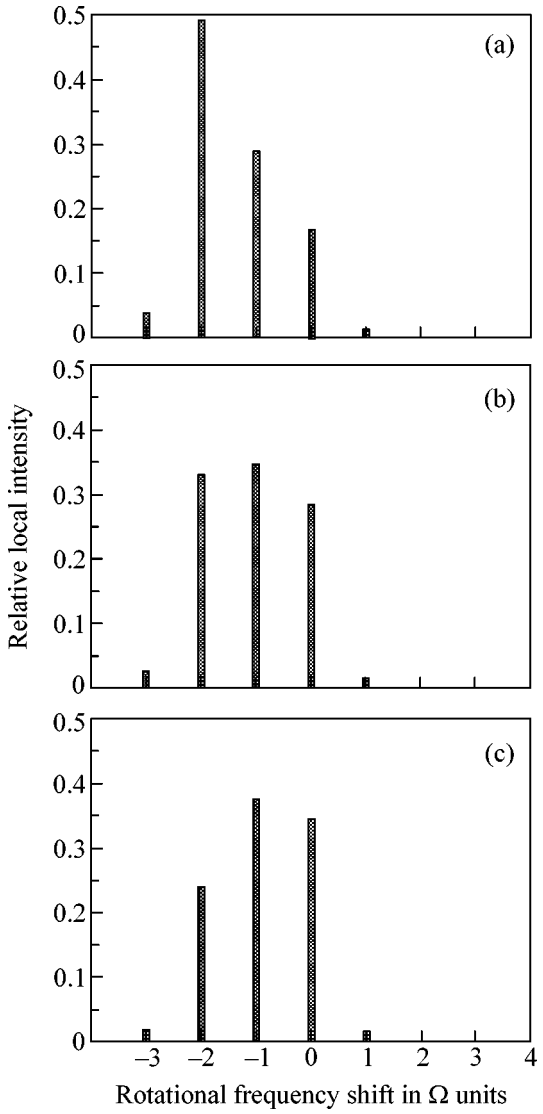

Fig. 3. RDE spectra calculated for various points of observation with the radial coordinate $\rho = 0.5w_0$ and φ = (a) 0, (b) $\pi/2$, and (c) π.

between the OAM component and the element, which changes the frequency of the component. The beam becomes polychromatic with a specific spatial distribution of monochromatic components. Our results also attribute the observed rotation of the image upon reflection to beats of the monochromatic components of the beam. In the case of beam rotation without reflection, the pattern of the original beam with an off-axis intensity dip is displaced parallel to itself, while the rotation of the element in the case of reflection leads to the rotation of the pattern of transverse distribution in the beam with doubled angular velocity.

We also note that the spatial dependence obtained for the rotating beam spectrum is applicable to problems of the transmission and reception of information based on OAM coding [9].

REFERENCES

1. M. V. Vasnetsov, V. A. Pas'ko, and M. S. Soskin, New J. Phys. **7**, 46 (2005); http://ej.iop.org/links/q12/goRgPFQgQ+OHnpImTSYxlw/njp5_1_046.pdf.
2. V. B. Berestetskiĭ, E. M. Lifshitz, and L. P. Pitaevskiĭ, *Quantum Electrodynamics*, 2nd ed. (Nauka, Moscow, 1980; Pergamon, Oxford, 1984).
3. M. Padgett, J. Courtial, and L. Allen, Phys. Today **57** (5), 35 (2004).
4. L. Allen, M. W. Beijersbergen, R. J. C. Spreew, and J. P. Woerdman, Phys. Rev. A **45**, 8185 (1992).
5. I. V. Basistyĭ, A. Ya. Bekshaev, M. V. Vasnetsov, *et al.*, Pis'ma Zh. Éksp. Teor. Fiz. **76**, 566 (2002) [JETP Lett. **76**, 486 (2002)].
6. M. V. Vasnetsov, J. P. Torres, D. V. Petrov, and L. Torner, Opt. Lett. **28**, 2285 (2003).
7. *Handbook of Mathematical Functions*, Ed. by M. Abramowitz and I. A. Stegun (National Bureau of Standards, Washington, 1964; Nauka, Moscow, 1979).
8. M. Vasnetsov and K. Staliunas, *Optical Vortices* (Nova Sci., New York, 1999).
9. G. Gibson, J. Courtial, M. Padgett, *et al.*, Opt. Express **12**, 5448 (2004); http://www.opticsinfobase.org/abstract.cfm?id=81642.

Translated by N. Wadhwa

JETP Letters, Vol. 81, No. 11, 2005, pp. 571–574. Translated from Pis'ma v Zhurnal Éksperimental'noĭ i Teoreticheskoĭ Fiziki, Vol. 81, No. 11, 2005, pp. 703–707.
Original Russian Text Copyright © 2005 by Mikhailova, Platonenko, Rykovanov.

Generation of an Attosecond X-Ray Pulse in a Thin Film Irradiated by an Ultrashort Ultrarelativistic Laser Pulse

Yu. M. Mikhailova, V. T. Platonenko, and S. G. Rykovanov

International Laser Center, Faculty of Physics, Moscow State University, Vorob'evy gory, Moscow, 119992 Russia

e-mail: mikhailova@ati.phys.msu.ru

Received April 27, 2005

The possibility of generating an attosecond x-ray pulse in a thin solid-density plasma layer irradiated by a femtosecond laser pulse of ultrarelativistic intensity has been demonstrated in numerical simulation. Changes in the plasma layer parameters during the light pulse result in the generation of a wide, partly continuous radiation spectrum in the layer. The separation of limited parts in the reflected or transmitted light spectrum makes it possible to obtain isolated short electromagnetic pulses with an intensity reaching 1% of the exciting light intensity.
© 2005 Pleiades Publishing, Inc.

PACS numbers: 42.65.Ky, 52.38.Ph

The generation of attosecond pulses (10^{-18}–10^{-15} s) (APa) of electromagnetic radiation is one of the topical problems of laser physics and nonlinear optics at the beginning of this century [1]. Attosecond pulses are not only of fundamental interest but also of considerable applied interest, in particular for various x-ray techniques (x-ray diffraction, spectroscopy, and microscopy) with subfemtosecond time resolution [2]. So far, the methods of obtaining APs based on the generation of coherent short-wavelength radiation upon atom ionization and subsequent recombination in intense laser beams have been theoretically analyzed and experimentally realized [3]. Unfortunately, the generation efficiency of atomic short-wavelength radiation is very low even under phase-matching conditions. In view of the creation of laser systems generating fields with intensity up to 10^{22} W/cm^2 [4], another way to obtain a wide coherent spectrum (and, thereby, a short pulse)—nonlinear interaction of a superstrong light field with a dense plasma [5]—that provides high efficiency of nonlinear optical transformation becomes particularly promising. The possibility of generating a train of attosecond pulses upon the reflection of ultraintense light from a supercritical plasma with a sharp density profile has been demonstrated in [6] using a 1D particle-in-cell (PIC) simulation. Selecting a certain number of high harmonics (above the 300th) in the simulation, Gordienko *et al.* [7] obtained trains of zeptosecond pulses. The problem of obtaining single APs was not discussed in [6, 7]. Formation of a single field splash, a videopulse, with a duration of less than a femtosecond was revealed in [8], where the reflection of a strongly focused light beam from a sharp boundary of a plasma with a density higher than a critical value by a factor of 1.5 was simulated.

The sharp density profile assumed in [7, 8] is practically unfeasible when the density is rather low ($N = 30N_c$ [7] and $1.5N_c$ [8], where N_c is the critical density). At the same time, when plasma density increases, the laser intensity required to generate attosecond pulses upon reflection from a massive solid target grows sharply. As is shown in this work, the above difficulty can be overcome using a freely suspended thin film. The numerical results presented below show that a single attosecond x-ray pulse can be efficiently generated by the interaction of an ultrashort laser pulse (τ_{FWHM} = 7 fs) of ultrarelativistic intensity ($I_\infty = 10^{21}$ W/cm^2) with a thin (40–100 nm) plasma layer of solid density ($N \approx 10^{23}$–10^{24} cm^{-3}).

The numerical investigation is carried out with a one-dimensional collisionless PIC model, which is capable of describing the interaction of a flat plasma layer with an intense laser beam of large diameter. The plasma layer is assumed to be initially ionized, with the ionization degree not changing during the simulation; the ion mass-to-charge ratio, which is the same for all ions, is 3762 times higher than that of an electron. The plasma has a sharp boundary and initial density $N = (250–300)N$. At $\lambda \approx 0.7$ μm, it roughly corresponds to the electron density in light metals, including the contribution of inner shells. The light pulse is linearly polarized and has a Gaussian time envelope $I(z, t) = I_0\exp(-t^2/\tau_e^2)$, and the pulse duration at half maximum $\tau_{FWHM} = 2\sqrt{\ln 2}\,\tau_e$ is equal to 2.5 field periods (about 7 fs for $\lambda = 0.8$ μm).

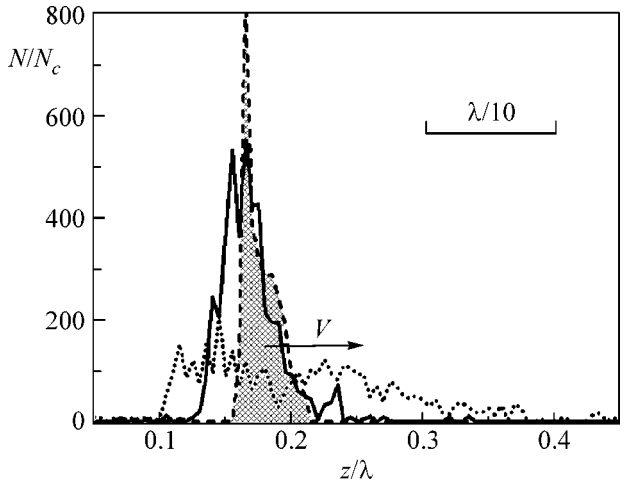

Fig. 1. Spatial distribution of particle density in units of the critical density N_c: (solid curve) electron density, (dashed curve) ion density, and (dotted curve) electron density at the end of the laser pulse.

The reliability of the results obtained with the PIC method depends strongly on the choice of time and space steps, the number of particles in a cell, and initial conditions, particularly at high deformations of the electron and ion plasma components. Moreover, in order to adequately interpret the results of a PIC simulation, it is necessary to eliminate the effects of mesh-related and numerical errors. An appropriate choice of time step is important not only for resolving as many high frequencies as possible but also for accurately describing ultrafast field changes upon interaction with the plasma, which provide the capability to generate APs. If the time step is insufficiently small, the field jump can be too sharp. In our computations, the time and space steps are $\Delta t = 1.25 \times 10^{-5} 1/\omega_0$, where ω_0 is the laser field frequency, and $\Delta z = 2.5 \times 10^{-3}\lambda/2\pi$, respectively. If the step increases noticeably, the results become step-dependent. Initially, 30 particles of each kind are in each mesh cell.

The results of simulations carried out for the given plasma layer density and thickness depend qualitatively on the intensity of the exciting light. For a quantitative intensity description, it is convenient to use a critical intensity I_c defined as follows:

$$I_c = I_{rel}\left(\frac{\pi l}{\lambda}\frac{N}{N_c}\right),$$

where l is the layer thickness, λ is the light wavelength, N is the plasma density, and $I_{rel} = c/8\pi(mc\omega/e)^2 \approx 1.37 \times 10^{18}[\lambda(\mu m)]^{-2}$ W/cm^2 is the intensity of linearly polarized light with the "relativistic" field amplitude $E_a = mc\omega/e$. At the intensity $I = I_c$, the light pressure amplitude $P_{light} = (1 + R)2I/c$ (where the reflectivity is $R \approx 1$) equals the maximum plasma layer counterpressure $R_{layer} = 2\pi(enl)^2$, the surface density of a force acting on the plates of a flat capacitor with charge density enl. It is natural to expect that, at intensities close to or above the critical value, the plasma layer will already be destroyed during the first field half-period, while, at intensities much lower than the critical value, a layer can last without noticeable deformation during many field periods. The following properties are observed in the calculations. Up to intensities $I \approx 0.25I_c$, the electron and ion plasma components, although they are strongly deformed in comparison with the initial state, remain in the form of relatively compact structures during the light pulse. The maximum density of both components in this case can noticeably (by almost an order of magnitude) exceed the initial values. Figure 1 shows the (solid curve) electron and (shading under the dashed curve) ion density distributions at a time close to the field node at the pulse center (initial layer density and thickness are $300N_c$ and $\lambda/10$, respectively). It is seen in Fig. 1 that the shift of the electron component with respect to the ion component not quite adiabatically follows the field change, i.e., oscillations of the light pressure. The centroid of the layer, or, more precisely, the centroid of the ion component, moves along the light beam direction with the velocity $V \approx 2\int I dt/c\rho l$, where ρ is the initial plasma mass density (the reflectivity remains close to unity). It is important that this velocity is relatively high and rises monotonically. The destruction of the plasma layer begins, as a rule, at approximately half of the critical intensity. By the end of the pulse, the electrons "scatter" along the light beam axis, mainly in the direction of the light propagation, as shown in Fig. 1 (dotted curve). The ion component is also strongly deformed, and the transmission of light increases strongly. Thus, the plasma layer parameters (thickness, density, and velocity) change continuously during the whole light pulse.

The plasma response to the field is of a resonance character: the nonlinear interaction of the incident light with a medium is most efficient at frequencies close to the natural frequencies of the medium. In this sense, the film acts as a resonator, with the spectrum of natural frequencies changing as the laser pulse interacts with it. It is important that these changes are aperiodic. Therefore, the spectral properties, as well as the intensity of reflected and transmitted light (in fact, radiation generated in the layer) are also aperiodic. Thus, it is possible to obtain isolated short electromagnetic pulses by cutting out limited parts of the reflected or transmitted spectrum.

If the film thickness and incident light parameters are appropriately chosen, it is possible to efficiently transfer incident radiation energy to the higher-frequency part of the spectrum. Numerical simulation allowed us to find at least three modes at which an isolated subfemtosecond pulse can be obtained. A single AP can be obtained in reflected light when the film is destroyed at the maximum incident intensity, i.e., at $I \geq I_c$. At $l = \lambda/20$ and $N = 250N_c$, the critical intensity is

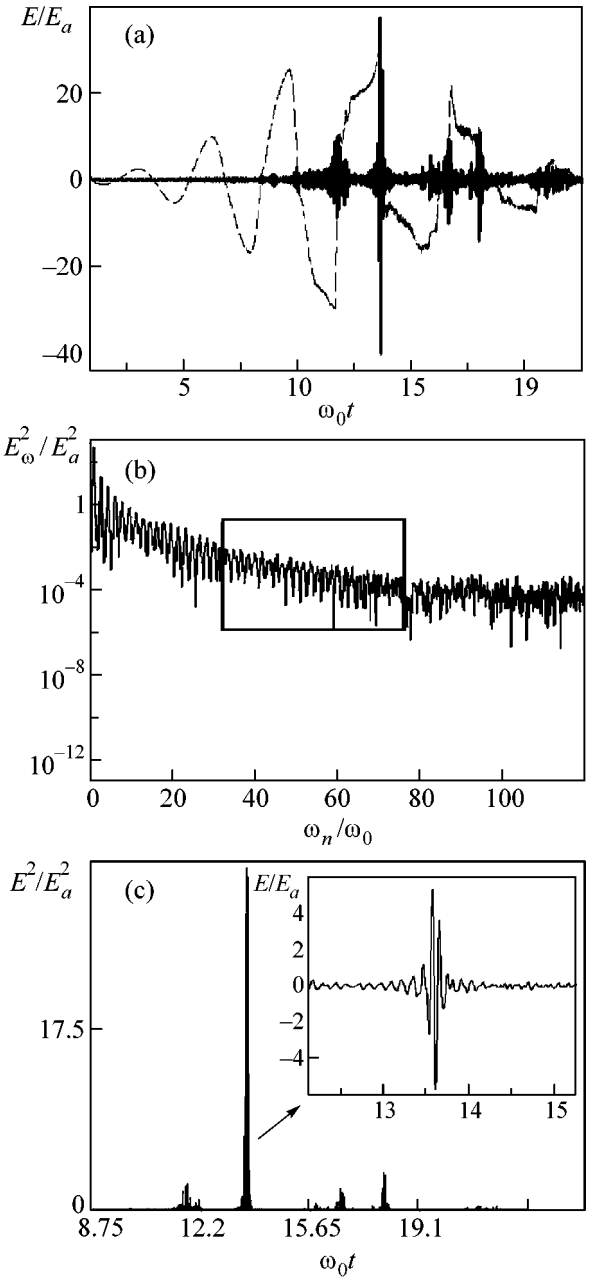

Fig. 2. (a) Time dependence ($\omega_0 t$ is in dimensionless units) of the field strength of (dashed curve) reflected light (in units of the relativistic amplitude $E_a = mc\omega/e$ at $l = \lambda/20$, $N = 250N_c$, and $I = 1700I_{rel}$) and (solid curve) after filtration (in units of $E_a/4$). (b) Reflected light spectrum, where filtration region is framed. (c) Time dependence of the field strength squared after filtration; the inset shows the attosecond-pulse field in a larger scale.

about ~$1500I_{rel}$, and it is possible to obtain a single AP at a laser pulse intensity in the interval $\approx(1.1–1.5)I_c$. Figure 2a shows the time dependence of the reflected field strength at $l = \lambda/20$, $N = 250N_c$, and $I = 1700I_{rel}$ (dashed curve) before and (solid curve) after filtration. The reflected light spectrum is shown in Fig. 2b, where

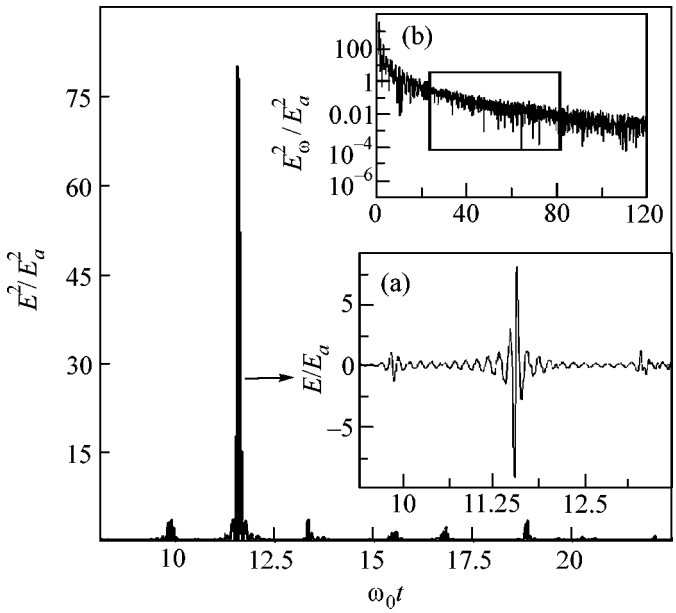

Fig. 3. Time dependence of the field strength squared after filtration; [inset (a)] the selected attosecond-pulse field; and [inset (b)] the reflected light spectrum at incident light intensity $I = 1900I_{rel}$, layer density $250N_c$, and thickness $\lambda/20$; the filtration region is framed.

the filtration region $(30–78)\omega_0$ is marked by a frame. Harmonics with integer numbers up to approximately the 50th harmonic are resolved in the spectrum, their frequencies are shifted to the left from the exact values, and the spectrum in the region of high frequencies becomes close to a continuous spectrum (the harmonics broaden). Figure 2c shows the field strength squared after filtration as a function of time. A 40-as pulse with an intensity $I = 16.5I_{rel}$ (1% of the exciting light intensity) and an intensity contrast of about nine is clearly seen. The field of this pulse is shown in a larger scale in the inset. By increasing the laser pulse intensity to $I = 1900I_{rel}$, it is possible to obtain an AP with even higher contrast and intensity. Figure 3 shows the field strength squared after filtration, [inset (b)] the reflected light spectrum, and [inset (a)] the selected AP field (intensity $I = 39I_{rel}$; intensity contrast about 23). The spectrum of such a pulse is continuous without a significant contribution from discrete integer harmonics. The presence of discrete harmonics in the selected part of the spectrum results in a lower pulse contrast.

An AP can be obtained in transmitted light as well, although with lower efficiency than in reflected light, in at least two cases: at intensities, first, far from the critical value, $I < I_c/10$, and, second, near the destruction threshold, $I \le I_c$. In the latter case, the laser pulse front hardly passes through the film, while radiation penetration at the pulse maximum is quite good. Figure 4 shows the transmitted field strength squared after filtration, [inset (b)] the transmitted light spectrum, where the filtration region $(20–50)\omega_0$ is marked by a frame,

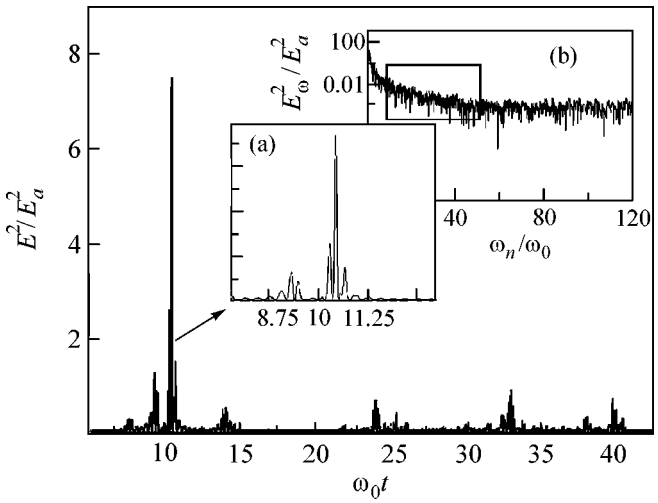

Fig. 4. Time dependence of the transmitted field squared after filtration; [inset (b)] the transmitted spectrum, where the filtration region (20–50)ω_0 is framed; and [inset (a)] the selected attosecond-pulse field at incident light intensity $I = 1500I_{rel}$, layer density $250N_c$, and thickness $\lambda/20$.

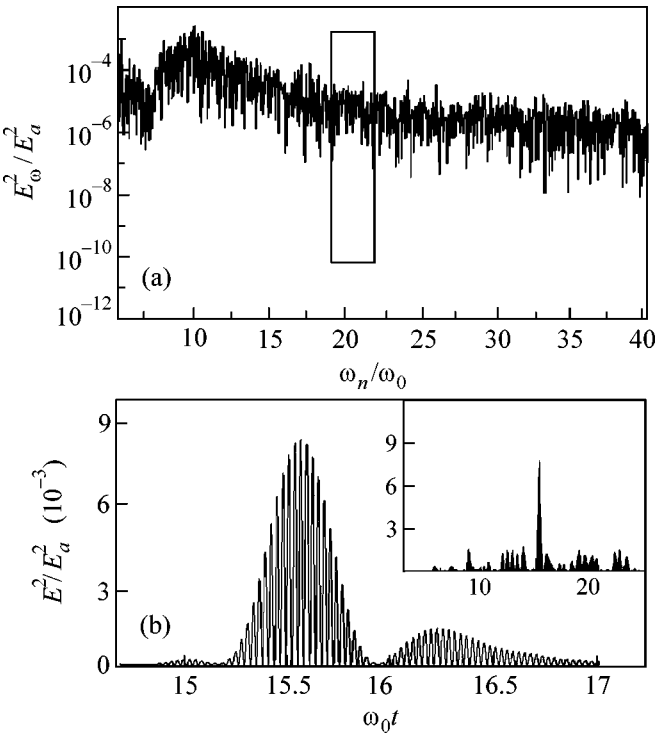

Fig. 5. (a) Transmitted light spectrum at $I = 600I_{rel}$, $N = 300N_c$, and $l = \lambda/10$; the filtration region (10–120)ω_0 is framed; (b) the selected attosecond-pulse field; the inset shows the field strength squared after filtration as a function of time.

and [inset (a)] the field of the selected AP with an intensity contrast of about six for incident light intensity $I = 1500I_{rel}$, layer density ~$250N_c$, and thickness $\lambda/20$. The number of well-resolved integer harmonics in the transmitted spectrum is small, and a considerable part of the energy is contained in the continuous spectrum.

At intensities far from the film destruction threshold, an AP containing higher harmonics as compared to the previous cases can be selected in transmitted light. The transmitted light spectrum at the incident intensity $I = 600I_{rel}$, layer density $300N_c$, and thickness $\lambda/10$ is shown in Fig. 5a. Integer harmonics are hardly pronounced against the continuous spectrum background. Selecting the spectral region (100–120)ω_0, we obtain the pulse shown in Fig. 5b (the inset shows the field after filtration on a smaller scale). This pulse duration is about 100 as, and the intensity contrast is about six. Selecting other parts of the same spectrum, other APs can be obtained, which are shifted along the time axis and differ in their duration and contrast. It appears possible to simultaneously select two APs with different frequencies shifted in time with respect to each other.

Thus, the numerical investigation of light interaction with a solid-density plasma layer demonstrates the possibility of obtaining a single attosecond x-ray pulse in a freely suspended thin film irradiated by an ultrarelativistic ultrashort laser pulse. Changes in the plasma layer parameters during the light pulse result in a nonstationary character of the plasma oscillation spectrum and in the formation of a wide radiation spectrum generated in the layer. The selection of separate parts of the spectrum using a bandpass filter allows one to obtain intense isolated subfemtosecond electromagnetic pulses. By varying the laser intensity and the thickness and density of the film, one can efficiently generate single APs of various spectral distributions, including pulses with frequencies several hundred times higher than the incident laser frequency.

The calculations were carried out on the computer cluster at the International Laser Center of Moscow State University. This work was supported by the Russian Foundation for Basic Research, project no. 05-02-17627.

REFERENCES

1. P. Agostini and L. F. DiMauro, Rep. Prog. Phys. **67**, 813 (2004).
2. M. Hentschel, R. Kienberger, Ch. Spielmann, *et al.*, Nature **414**, 509 (2001).
3. M. Drescher, M. Hentschel, R. Kienberger, *et al.*, Nature **419**, 803 (2002); Y. Mairesse, A. de Bohan, L. J. Frasinski, *et al.*, Science **302**, 1540 (2003).
4. S.-W. Bahk, P. Rousseau, T. A. Planchon, *et al.*, Opt. Lett. **29**, 2837 (2004).
5. P. Gibbon, Phys. Rev. Lett. **76**, 50 (1996).
6. L. Plaja, L. Roso, K. Rzazewski, and M. Lewenstein, J. Opt. Soc. Am. B **15**, 1904 (1998).
7. S. Gordienko, A. Pukhov, O. Shorokhov, and T. Baeva, Phys. Rev. Lett. **93**, 115002 (2004).
8. N. M. Naumova, J. A. Nees, I. V. Sokolov, *et al.*, Phys. Rev. Lett. **92**, 063902 (2004).

Translated by E. Baldina

JETP Letters, Vol. 81, No. 11, 2005, pp. 575–578. Translated from Pis'ma v Zhurnal Éksperimental'noĭ i Teoreticheskoĭ Fiziki, Vol. 81, No. 11, 2005, pp. 708–711.
Original Russian Text Copyright © 2005 by Volkov, Gordienko, Lachko, Savel'ev, Uryupina.

Acceleration of Heavy Multicharged Ions up to 1 MeV from a Cleaned Solid Target Irradiated by a Femtosecond Laser Pulse with an Intensity of 10^{16} W/cm^2

R. V. Volkov, V. M. Gordienko, I. M. Lachko, A. B. Savel'ev, and D. S. Uryupina

International Laser Center, Faculty of Physics, Moscow State University, Vorob'evy gory, Moscow, 119992 Russia

e-mail: savelev@femto.phys.msu.ru

Received April 29, 2005

A noticeable increase in the charge and energy of ions accelerated from a solid tungsten target irradiated by a femtosecond laser pulse with an intensity higher than 10^{16} W/cm^2 has been found when the target surface is precleaned by a nanosecond laser pulse with an energy density of 3 J/cm^2. Tungsten ions with charges up to +29 and energies up to 1 MeV were detected in this case, while the charge and energy of tungsten ions from a target with an uncleaned surface do not exceed +3 and 12 keV, respectively. © *2005 Pleiades Publishing, Inc.*

PACS numbers: 52.38.Kd, 52.50.Jm

At present, the formation of ion beams in the interaction of ultrashort laser pulses with dense targets is attracting considerable attention. Understanding of the mechanisms of fast ion acceleration, as well as optimization of ion beam parameters, is particularly important for the application of fast ion beams in various fields of fundamental and applied science [1, 2]. According to research [3–6], protons, which are always present in an adsorbed steam and oil-vapor layer on the target surface, are predominantly accelerated at the plasma–vacuum interface. The removal of this layer from the surface provides for the acceleration of ions of the main target material to high energies [5–7]. It is shown in this work that not only average energy per unit ion charge but also maximum charge of accelerated ions increase noticeably when a precleaned target surface is irradiated by 10^{16}-W/cm^2 femtosecond laser radiation. Tungsten ions with the energy up to 1 MeV and charge up to +29 were detected from a tungsten target.

The experimental setup is shown schematically in Fig. 1. The *P*-polarized radiation of the femtosecond laser system (λ = 616 nm, E = 0.5 mJ, τ = 200 fs) [8] was focused by an objective onto the target surface at an angle of 45° up to intensity of $I \sim 2 \times 10^{16}$ W/cm^2. The prepulse energy density did not exceed 0.3 J/cm^2, and the duration of the prepulse was about 40 ps. The target was placed in a vacuum chamber and shifted after each laser pulse. The residual gas pressure in the chamber was 10^{-5} Torr. The radiation of a pulsed XeCl excimer laser (λ = 308 nm, E = 10 mJ, τ = 30 ns) that entered the chamber through the second input window was used for target cleaning. A lens focused it in a 500-μm spot in the same target area as the femtosecond pulse. The energy density $W \sim 3$ J/cm^2 of the cleaning pulse and the time interval between the cleaning pulse and the femtosecond pulse $\Delta\tau$ = 100 μs were selected based on our experimental results [6].

Ion currents were detected perpendicularly to the target surface using an electrostatic mass spectrometer placed in a separate detection chamber (see Fig. 1). The angular acceptance was 8×10^{-4} sr. The mass spectrometer parameters and operation principle are described in more detail in [9]. Along with the ion plasma current, the x-ray yield was measured using a two-channel analyzer based on a photomultiplier tube with a NaJ scintillator and a set of Al and Be spectral filters. This method allows one to estimate the average energy of hot electrons in each laser shot [9, 10]. According to the results of x-ray plasma diagnostics, the average energy

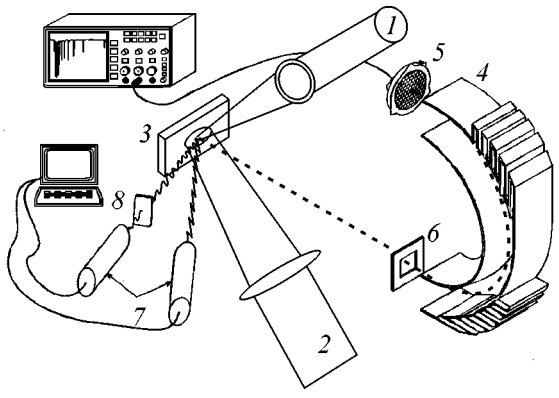

Fig. 1. Experimental setup: (*1*) femtosecond laser beam, (*2*) nanosecond laser beam, (*3*) target, (*4*) electrostatic mass spectrometer, (*5*) microchannel plate, (*6*) aperture, (*7*) x-ray detectors, and (*8*) x-ray filters.

0021-3640/05/8111-0575$26.00 © 2005 Pleiades Publishing, Inc.

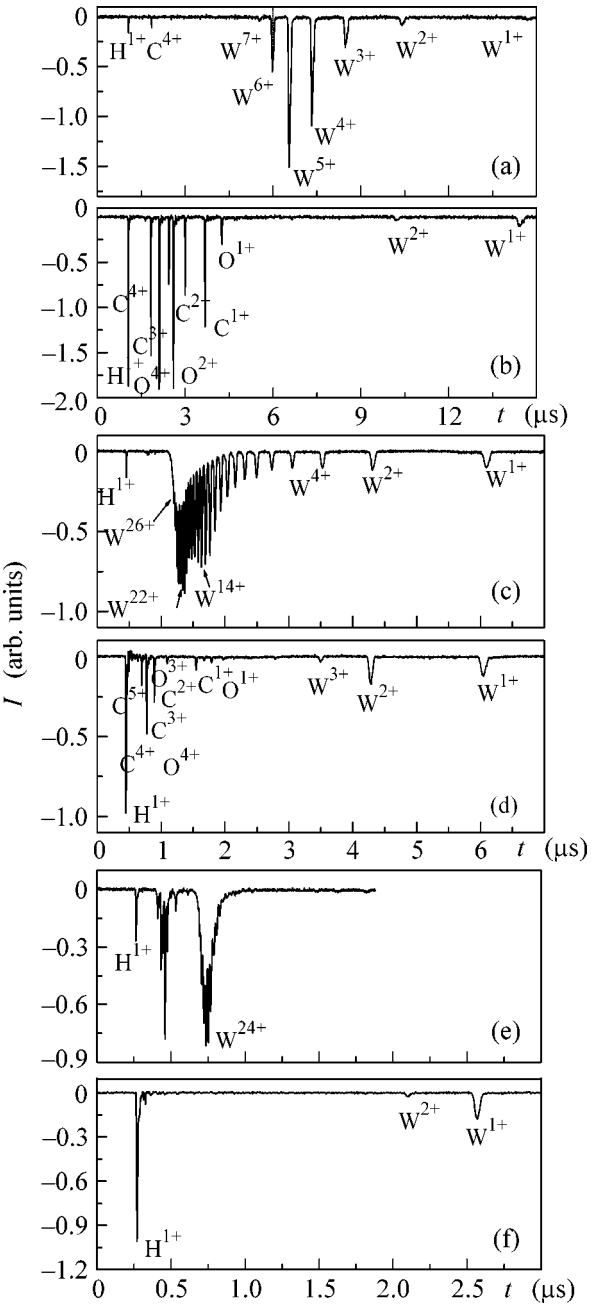

Fig. 2. Ion plasma currents from the [(a), (c), and (e)] cleaned and [(b), (d), and (f)] uncleaned tungsten targets for various ion energies per unit charge: (a) and (b) 1.8 keV, (c) and (d) 10.1 keV, and (e) and (f) 28 keV.

of hot electrons is $E_e = 6 \pm 2$ keV for the case of formation of a laser plasma on both precleaned and uncleaned target surfaces. No significant difference was found in the absolute yield of hard x-rays from the plasma. Thus, pulsed laser cleaning did not affect hot electron formation at the plasma–vacuum interface.

Typical signals recorded by the ion spectrometer from a tungsten target are shown in Figs. 2a and 2b. The signal was obtained for an ion energy of 1800 eV per unit charge. In the absence of pulsed laser cleaning, the ion current comprises predominantly hydrogen, carbon, and oxygen ions. The maximum ion charge reaches +6 for carbon (fully ionized atom; the ionization potential of the last *K*-shell electron is equal to 490 eV), +6 for oxygen (a helium-like ion the ionization potential of the lithium-like ion is equal to 138 eV), and only +3 for tungsten (ionization potential is 24 eV), where the total number of electrons is 74. The observed ion charge distribution is undoubtedly determined not only by ionization in the dense plasma but also by recombination during plasma expansion and flight of ions to the detector. The latter process depends strongly on ion velocity: as the velocity increases, the recombination rate decreases because the electron density of the plasma through which the ion moves decreases [11]. Thus, the initial tungsten ion charge immediately after the action of a femtosecond laser pulse is considerably higher than the detected charge.

In the case of the cleaned target (Fig. 2a), tungsten ions with a wide charge spectrum from +1 to +7 (the ionization potential of W^{7+} is about 60 eV) dominate in the ion current. A weak signal corresponding to protons and carbon ions is also present. The ion current from the uncleaned initial target consists mainly of hydrogen, carbon, and oxygen ions, and tungsten ions have charges +1 and +2. When the energy per unit charge of detected ions increases to 10 keV (Figs. 2c and 2d), tungsten ions with charges from +1 to +3, as well as protons and carbon ions, were observed from the initial target, while mainly tungsten ions with a wide charge spectrum from +1 to +26 were detected for the cleaned target.

A further increase in the energy of detected ions (Figs. 2e and 2f) did not result in noticeable change in the parameters of the ion current from the uncleaned target, while high-energy tungsten ions with an average charge of +22 were detected from the cleaned target. The maximum charge of tungsten ions in our experiments reached +29 (the ionization potential of the W^{28+} ion is higher than 700 eV) for the maximum ion energy 980 keV. Moreover, oxygen ions with a charge of +8 (ionization potential is 870 eV) were also observed. The energy spectra of some tungsten ions from the cleaned target are shown in Fig. 3. Analysis shows that the energy spectrum of tungsten ions with charges $Z > 18$ is well approximated by an exponential function of the form $e^{-\alpha\varepsilon_i}$, where α is independent of the ion charge Z and $\alpha^{-1} \approx 11.2 \pm 2$ keV. The independence of α from the ion charge shows that recombination of fast tungsten ions during their flight to the detector is negligible and that the recorded charge spectrum depicts the charge spectrum of tungsten ions at the very moment of their acceleration in the hot dense plasma.

The charge spectrum of tungsten ions from the cleaned target is shown in Fig. 4. Two groups of ions with average charges +5 and +22 are clearly visible (see also Fig. 2c). The presence of the two groups of ions is

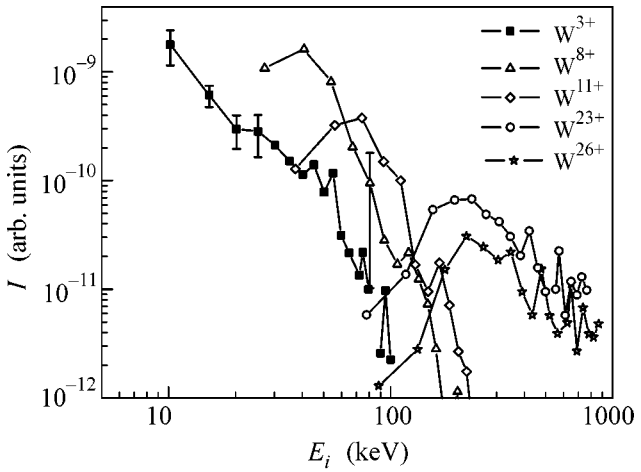

Fig. 3. Energy spectra of tungsten ions from the cleaned target.

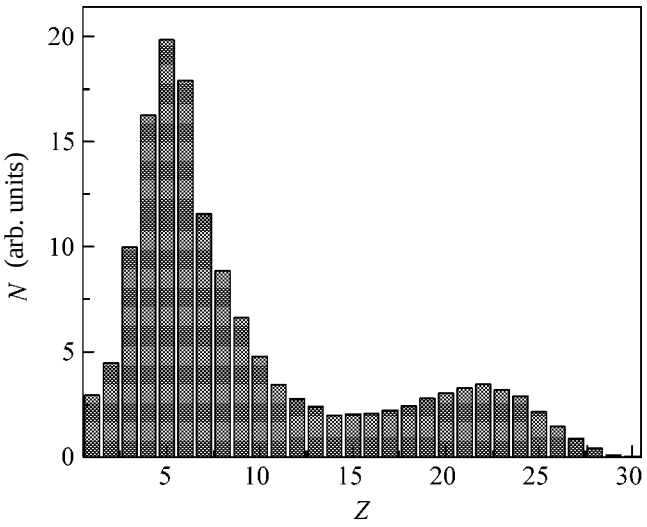

Fig. 4. Charge distribution of tungsten ions from the cleaned target.

attributed to efficient generation of hot electrons and, therefore, to a non-Maxwellian character of the electron energy distribution in the plasma [12]. The estimate obtained for the parameter α agrees well with the energy of hot electrons that is estimated above using the hard x-ray yield from the plasma (see above): the mean energy of a three-dimensional electron distribution E_e relates to the average energy of one-dimensional ion motion as $E_e \approx 0.5\alpha$ [7]. It should be noted that the charge and energy spectra of tungsten ions from the initial target are determined only by the equilibrium thermal part of the electron energy distribution, while hot electrons accelerate hydrogen, carbon, and oxygen ions from the target surface layer [7].

Thus, cleaning the target surface leads to an increase in the energy of the ions of the dominant target material due to, first, the efficient acceleration of these ions by the hot electron component and, second, an increase in the ionization multiplicity. The latter effect may be attributed to the inhomogeneity of the spatial temperature distribution of plasma thermal electrons during a femtosecond laser pulse. Thus, the 1D hydrodynamic simulations of the interaction of the femtosecond laser pulse with a plasma [13] show that the temperature at the plasma–vacuum interface in the maximum of the heating 200-fs pulse with intensity 10^{16} W/cm^2 is twice as high as the temperature at a depth of 40 nm and reaches 200 eV for an electron density of 10^{23} cm^{-3}. The average ionization multiplicity in the surface layer, where the ion concentration is one-fifth; of the solid-state value, reaches 20–22 at the laser pulse maximum. Note that the effect of hot electrons on the plasma charge distribution is insignificant [14] due to their high average energy and low concentration. Since hot electrons accelerate ions near the interface, some ions of the main target material are ionized to high charge values only on the cleaned target surface and, then, are efficiently accelerated by hot electrons.

The maximum charge of tungsten ions (+29) observed in the experiment is noticeably higher than the numerically predicted value (the charge distribution width in the dense plasma does not exceed ±2). The explanation of the observed effect of deep ionization of atoms on the cleaned surface may be associated with nonthermal ionization mechanisms. In particular, at much higher laser intensities (above 10^{18} W/cm^2), the anomalous ionization of ions accelerated from the rear target surface was observed in [15], where this effect was attributed to ionization by an accelerating ambipolar field. This ionization can also be observed in our experiments. Indeed, the accelerating field strength $\tilde{E}$ in the plasma with two electron components can be estimated as follows [16]:

$$\tilde{E} = \sqrt{8\pi(n_{\text{th}}T_{\text{th}} + n_{\text{h}}T_{\text{h}})},$$

where n_{th} (T_{th}) and n_{h} (T_{h}) are the concentrations (temperatures) of thermal and hot electrons, respectively. Under our experimental conditions ($n_{\text{th}} \approx 5 \times 10^{23}$ cm^{-3}, $T_{\text{th}} \approx 300$ eV, $n_{\text{h}} \approx 5 \times 10^{20}$ cm^{-3}, $T_{\text{h}} \approx 4000$ eV [9]), this expression yields an $\tilde{E}$ estimate of 2×10^{10} V/cm. Due to the mechanism of above-threshold ionization [17], such a field can ionize ions with an ionization potential of up to 600 eV (the average ionization multiplicity of the plasma is $z = 15$), which corresponds to an ion charge of up to +26 for the tungsten atom. A more detailed discussion of this mechanism is beyond the scope of this paper and requires more detailed numerical simulations, as well as additional experimental investigations.

This work was supported by the Russian Foundation for Basic Research, project no. 04-02-16341, and the

International Science and Technology Center, grant no. 2651(r). The work of I.M.L. was supported by INTAS, grant no. 03-55-1982.

REFERENCES

1. K. W. D. Ledingham, P. McKenna, and R. P. Singhal, Science **300**, 1107 (2003).
2. Y. Sentoku, T. E. Cowan, A. Kemp, and H. Ruhl, Phys. Plasmas **10**, 2009 (2003).
3. E. L. Clark, K. Krushelnick, J. R. Davies, *et al.*, Phys. Rev. Lett. **84**, 670 (2000).
4. R. A. Snavely, M. H. Key, S. P. Hatchett, *et al.*, Phys. Rev. Lett. **85**, 2945 (2000).
5. M. Roth, M. Allen, P. Audebert, *et al.*, Plasma Phys. Controlled Fusion **44**, B99 (2002).
6. R. V. Volkov, D. M. Golishnikov, V. M. Gordienko, *et al.*, Kvantovaya Élektron. (Moscow) **33**, 981 (2003).
7. V. M. Gordienko, I. M. Lachko, A. A. Rusanov, *et al.*, Appl. Phys. B **80**, 733 (2005).
8. R. V. Volkov, V. M. Gordienko, M. S. Dzhidzhoev, *et al.*, Kvantovaya Élektron. (Moscow) **24**, 1114 (1997) [Quantum Electron. **27**, 1081 (1997)].
9. V. M. Gordienko, I. M. Lachko, P. M. Mikheev, *et al.*, Plasma Phys. Controlled Fusion **44**, 2555 (2002).
10. R. V. Volkov, V. M. Gordienko, P. M. Mikheev, and A. B. Savel'ev, Kvantovaya Élektron. (Moscow) **30**, 896 (2000) [Quantum Electron. **30**, 896 (2000)].
11. R. W. P. McWhirter, *Plasma Diagnostic Techniques* (Academic, New York, 1965), p. 210.
12. L. M. Wickens and J. E. Allen, Phys. Rev. Lett. **41**, 243 (1978).
13. V. M. Gordienko, M. A. Joukov, A. B. Savel'ev, *et al.*, in *Application of High Field and Short Wavelength Sources*, Ed. by L. DiMauro, M. Murnane, and A. H'Huiller (Plenum, New York, 1998), p. 155.
14. V. V. Bol'shakov, V. M. Gordienko, A. B. Savel'ev, and O. V. Chutko, Pis'ma Zh. Éksp. Teor. Fiz. **79**, 80 (2004) [JETP Lett. **79**, 71 (2004)].
15. M. Hegelich, S. Karsch, G. Pretzler, *et al.*, Phys. Rev. Lett. **89**, 085 002 (2002).
16. M. Passoni, V. T. Tikhonchuk, M. Lontano, and V. Yu. Bychenkov, Phys. Rev. E **69**, 026411 (2004).
17. V. P. Krainov, J. Opt. Soc. Am. B **14**, 425 (1997).

Translated by E. Baldina

JETP Letters, Vol. 81, No. 11, 2005, pp. 579–582. Translated from Pis'ma v Zhurnal Éksperimental'noĭ i Teoreticheskoĭ Fiziki, Vol. 81, No. 11, 2005, pp. 712–716.
Original Russian Text Copyright © 2005 by Kamzina, Xu, Shi, Wu.

Phase Transitions and Optical Properties in ⟨001⟩ $(1 - x)PbZn_{1/3}Nb_{2/3}O_3 - xPbTiO_3$ Single Crystals

L. S. Kamzina[1], J. Xu[2], M. Shi[2], and X. Wu[2]

[1] *Ioffe Physicotechnical Institute, Russian Academy of Sciences, St. Petersburg, 194021 Russia*
e-mail: kamzin@AK12758.spb.edu

[2] *Shanghai Institute of Ceramics, Chinese Academy of Sciences, Shanghai 200050, People Republic of China*

Received April 20, 2005

The effect of a constant electric field ($0 < E < 5$ kV/cm) on the optical properties of $PbZn_{1/3}Nb_{2/3}O_3 - xPbTiO_3$ (PZN–*x*PT) crystals with $x = 7$ and 9% has been analyzed. It has been shown that, at temperatures close to the temperature of the transition from the rhombohedral [R(X)] phase to the tetragonal (T) phase, two induced phase transitions are observed in the electric field, which are associated with the appearance of new intermediate phases M_a and M_c [R(X)–M_a–M_c–T]. Correlation between these two transitions and the $PbTiO_3$ content *x* has been found. The *E*–*T* phase diagrams have been obtained. The M_c phase in PZN–9PT crystals is found to remain the ground state after the removal of the electric field, whereas the M_c phase in PZN–7PT crystals is metastable and is transformed into the M_a phase after the removal of the electric field. © *2005 Pleiades Publishing, Inc.*

PACS numbers: 77.80.Bh, 78.20.Ci

Solid solutions $PbZn_{1/3}Nb_{2/3}O_3$ (PZN) containing several percent $PbTiO_3$ (PZN–*x*PT) are relaxor ferroelectrics with a very high piezoelectric response that is an order of magnitude higher than the value in the standard piezoelectric ceramic of the type $Pb(ZrTi)O_3$ (PZT). They have cubic symmetry (C) at high temperatures and undergo a smooth phase transition as temperature decreases. Materials in the ferroelectric region in dependence on the structure have either rhombohedral (R) or tetragonal (T) symmetry, which are separated by the morphotropic phase boundary at $x \sim 9$–10%, similar to the well-known piezoelectric PZT system.

Surprisingly high values of electromechanical coupling and mechanical stresses were observed in rhombohedral crystals close to morphotropic phase boundary. These crystals were polarized along the [001] direction [1], although the polar axis in them coincides with the [111] direction [2]. The origin of an extremely high piezoelectricity of these materials and the effect of the electric field on the behavior of the polarization were studied theoretically and experimentally in many works. The polarization-rotation mechanism proposed in [3] explains the huge values of the electromechanical response in PZN–*x*PT. According to this model, the application of the field along the [001] direction in rhombohedral PZN–*x*PT crystals induces the rotation of the polarization vector in the (110) plane from the rhombohedral phase to the tetragonal one through the intermediate third monoclinic (M) phase. As was pointed out in [4], this transition is irreversible. The exact symmetry of this intermediate phase in compounds with various *x* values is under discussion. This symmetry depends on the path of the rotation of the polarization vector in the transition from the R phase to the T phase. Phase transitions induced by the electric field were analyzed for PZN–4.5PT and PZN–8PT crystals [5–7] by neutron and x-ray methods. In the PZN–4.5PT crystals that are far from the morphotropic phase boundary, the polarization vector was shown to rotate directly from the [111] direction to the [001] direction through the monoclinic M_a phase. At the same time, in the PZN–8PT compounds that are closer to the morphotropic phase boundary, the polarization vector first rotates in the R–M_a–T direction and, then, stepwise changes to a new path in the plane that contains the orthorhombic and tetragonal polar axes (i.e., R–M_a–M_c–T) [4, 5, 8]. Although the existence of low-symmetric monoclinic phases in a ferroelectric system with perovskite structure near the morphotropic phase boundary is unusual, Vanderbilt and Cohen [9] succeeded in explaining it within the framework of the Devonshire theory for strongly anharmonic crystals for which high-order terms are important. Their work made it possible to plot a new phase diagram for ferroelectric perovskites, which includes three different monoclinic phases M_a, M_b, and M_c, where the polarization vector lies in the pseudocubic $\{1\bar{1}0\}$ plane, {100} plane, and {010} plane, respectively. For both crystals, the tetragonal phase was observed only in high electric fields ~10–20 kV/cm. As the electric field decreases, the polarization vector rotates from the tetragonal [001] direction to the orthorhombic direction through the M_c phase and the initial rhombohedral state does not arise

0021-3640/05/8111-0579$26.00 © 2005 Pleiades Publishing, Inc.

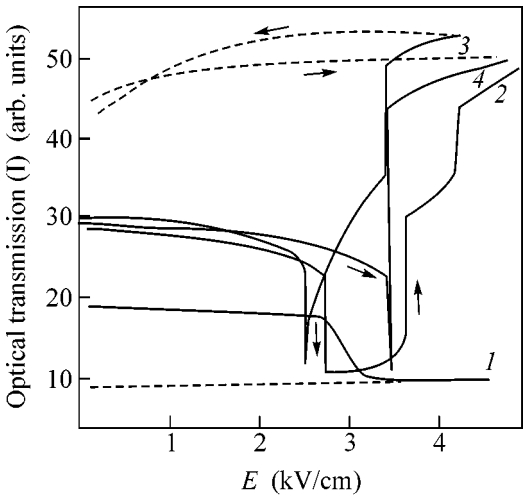

Fig. 1. Electric field dependences of the optical transmission *I* for the PZN–9PT crystals as measured at a temperature of (*1*) 289, (*2*) 320, (*3*) 332, and (*4*) 346 K.

even after the removal of the field (T–M_c). The *E–T* phase diagram plotted for PZN–8PT crystals in [10] on the basis of complicated neutron-diffraction measurements corroborated the conclusions made in [6, 7]. Moreover, the authors of [10] found that the system cooled even in the absence of field (ZFC) transits to a certain unidentified phase R(X) rather than to the R phase, as was thought previously. The existence of this new R(X) phase was corroborated in more recent works [11, 12].

Although induced phase transitions in the PZN–*x*PT system, as well as the origin of extremely high piezoelectricity at the morphotropic phase boundary, were investigated in numerous neutron and x-ray studies, there is no common opinion not only on the symmetry of intermediate phases arising in the field but also on their number. For complete understanding of the behavior observed in electric fields, a larger number of crystals with various *x* values, as well as various investigation methods including optical methods, are necessary. Data on the optical properties of these compounds are almost absent except for our work [13] and works [14, 15] devoted to the domain structure. At the same time, optical investigations, namely, measurements of optical transmission and small-angle light scattering [13], could provide additional information on the physical properties of these substances, because these methods are more sensitive compared to, e.g., dielectric methods, particularly for studying changes in inhomogeneity sizes in phase transitions.

In this paper, we present the results of an investigation of the optical transmission of PZN–9PT and PZN–7PT crystals, which are near the morphotropic phase boundary, in a temperature range of 273–500 K for various regimes of the application of a constant electric field $0 < E < 5$ kV/cm. The PZN–9PT and PZN–7PT crystals were grown by the modified Bridgman method in a 50 mol % PbO melt [16] and had rhombohedral symmetry at room temperature, and their maximum sizes reached 30 mm in diameter and 28 mm in length. The crystals were cut perpendicularly to the [001] direction into several parts 1–1.5-mm thick. The electric field was applied in the [001] direction, and light was propagated in the [100] direction. The Curie temperature is $T_c \sim 443$–453 K for PZN–9PT, the temperature of the morphotropic phase transition between R(X) and T phases is $T_{tr} \sim 333$–343 K, and $T_c \sim 452$ K and $T_{tr} \sim 393$ K for PZN–7PT. To reveal the electric field effect on the sequence of the phase transitions, we carried out two runs of measurements. First, the temperature dependence of the optical transmission was studied when cooling a crystal in various electric fields (FC). Second, the optical transmission was analyzed in the R(X) phase at fixed temperatures near T_{tr} as the electric field increases. To this end, the crystal before each measurement was heated above T_c, then was cooled to the RT that lies in the ferroelectric phase (ZFC), and finally was heated to the measurement temperature (ZFH). The temperature was stabilized and an electric field with various amplitudes was applied. A He–Ne laser was used for optical measurements.

Figure 1 shows the electric field dependences of the optical transmission *I* measured in cycle *2* in the ferroelectric phase at certain temperatures near T_{tr} for the PZN–9PT crystals. The evolution of *I* in the electric field that is associated with induced phase transitions is clearly seen in the figure. We emphasize that variations in *I* are not caused by the appearance of the tetragonal phase, because the measurements were carried out on sufficiently thick samples and the tetragonal phase arising in high electric fields could not be reached before the failure of the sample. In low electric fields, optical transmission is almost constant for all temperatures (lines *1–4*). Then, at a certain threshold field, a sharp decrease in the transmission is observed, which is attributed to the induced phase transition to another (likely M_a) phase. Since the symmetry of the arising phases cannot be determined in our optical measurements, we will use the notation of phases proposed in [5, 8]. The closer the temperature of measurement to the temperature T_{tr} of morphotropic phase transition, the lower the field at which this phase is induced (Fig. 1, lines *1–3*). A decrease in the transmission in the process of the transition to the monoclinic phase M_a indicates that the scattering of light in this phase is higher than the scattering in the rhombohedral phase R(X). This relation implies that the size of scatterers (domains or polar regions) increases in the M_a phase, because scattering depends on the ratio of the particle size to the light wavelength. With a further increase in the field, another induced phase transition to a new (likely M_c) phase is observed. The farther the measurement temperature from T_{tr}, the wider the region of the existence of the M_a phase (lines *2* and *3*). At temperatures far from T_{tr} (line *1*), we did not observe the induc-

tion of the M_c phase in the electric fields under investigation. The transmission in the M_c phase is much higher than in the phases M_a and R(X). This relation indicates that the domains in the M_c phase are smaller. A stepwise increase in the optical transmission with variations in the field that accompanies the induction of the M_c phase (lines *2*, *3*) apparently occurs due to the inhomogeneity of the phase. At measurement temperatures near T_{tr}, the region of the existence of the M_a phase collapses and the crystal transforms from the rhombohedral phase immediately to the M_c phase (lines *3* and *4*). In this transition, a sharp peak is observed in optical transmission. The existence of this peak corroborates both the percolation origin of the field-induced transition from the R(X) phase to the monoclinic phase and the appearance of a large-scale structure (these transition and structure were found in our work [13]). If the phase transition is of the percolation type, the mean size of the new-phase clusters at the percolation threshold tends to the sample size, a large-scale structure arises, and the phase transition is necessarily accompanied by the appearance of an anomalously narrow peak of the small-angle light scattering intensity and, therefore, by the minimum of optical transmission [17].

According to the dashed lines on curves *1*, *3*, and *4*, the M_a and M_c phases induced by the field in the PZN–9PT crystals remain stable after the removal of the field; i.e., the crystal remains in the monoclinic phase even after the removal of the field. Ohwada *et al.* [10] reported that the M_a phase remained stable at room temperature for more than two weeks after the removal of the field.

Similar dependences were obtained for the PZN–7PT crystals. Similarly to the PZN–9PT crystals, two induced phase transitions are observed in the electric fields under investigation. A substantial feature of the PZN–7PT crystal is the instability of the M_c phase after the removal of the electric field and the transition of the system to the M_a phase. It is remarkable that the M_c phase is not observed in the electric field (R–M_a–T) in the PZN–4.5PT crystals that are farther from the morphotropic phase boundary than the PZN–7PT crystals. At the same time, the M_c phase (R–M_a–M_c–T) in the PZN–8PT crystals [5, 6] and PZN–7PT crystals (this work) remains stable after the removal of the field. Our measurements of the optical transmission of the PZN–7PT crystals show that these crystals belong to the boundary of compositions for which the appearance of the second monoclinic mode in low electric fields is possible, but only the M_a phase remains stable.

Using the temperature dependences of the optical transmission that were obtained in different electric fields in two measurement runs (FC regime and the regime of Fig. 1), we plot the *E*–*T* phase diagrams for the (Fig. 2) PZN–9PT and (Fig. 3) PZN–7PT crystals. As is seen, the phase diagrams are almost identical for both crystals. Figures 2a and 3a show the results

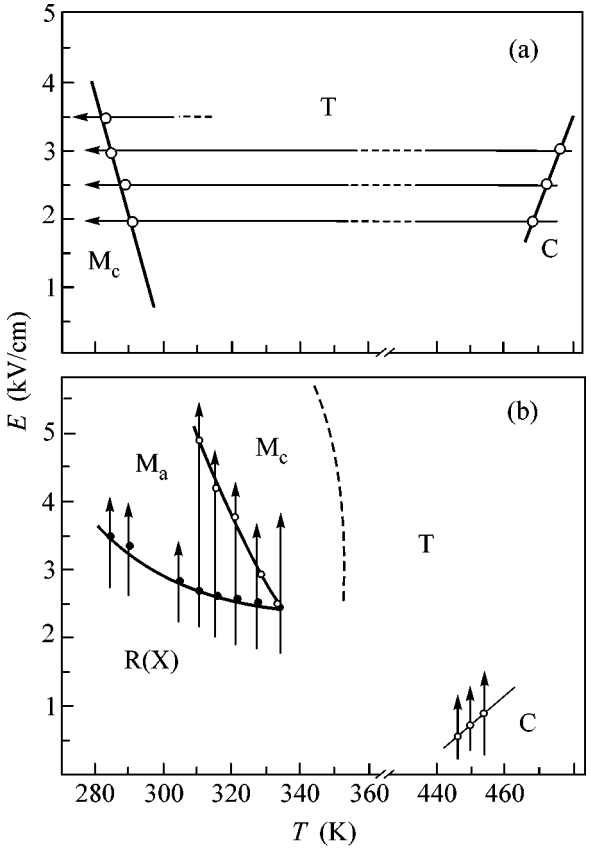

Fig. 2. *E*–*T* phase diagram for the PZN–9PT crystal as obtained from optical measurements (a) in the FC regime and (b) with an increase in the electric field after ZFC. The arrows show the direction of the applied electric field. The points correspond to the transition temperatures and fields determined for each particular measurement. The dashed line corresponds to the phase boundary between the M_c and T phases.

obtained in the FC process. As the electric field increases, the C–T and T–M_c phase boundaries in both crystals are shifted towards higher and lower temperatures, respectively. This indicates that the tetragonal phase is stable at high electric fields in both crystals. As is seen in Figs. 2a and 3a, the M_a phase does not appear in the FC regime. It was shown in [10] that this phase does not appear in the FC regime in the PZN–8PT crystals in extremely low electric fields ~0.5 kV/cm.

Figures 2b and 3b summarize the results for the optical transmission that were obtained with an increase in the electric field at the given temperatures after ZFC. At high temperatures, the C phase reversibly transforms to the tetragonal phase and the phase boundary behaves similar to the behavior seen in Figs. 2a and 3a. At low temperatures, the R(X) phase irreversibly transforms to the M_a phase, which transforms to the M_c phase in higher fields. We note that the phases R(X) and M_a become stable as temperature decreases, and the region of the existence of the M_a phase in the PZN–7PT

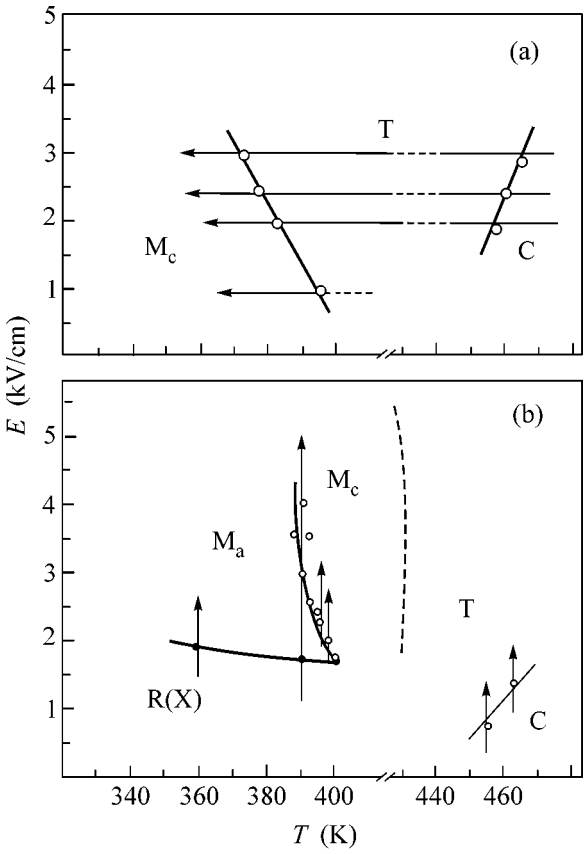

Fig. 3. Same as in Fig. 2, but for the PZN–7PT crystal.

crystals is wider than that in the PZN–9PT crystals. As the temperature approaches T_{tr}, the region of the existence of the M_a phase collapses and the crystal transforms from the R(X) phase immediately to the M_c phase. We point to the difference in the behavior of two crystals. When the M_c phase arises in the PZN–9PT crystal, the R(X) and M_a phases are not recovered in it for a long time and the M_c–T phase transition occurs only in higher fields. At the same time, the M_c phase in the PZN–7PT crystals is unstable after the removal of the field, which is corroborated by the existence of the almost vertical M_a–M_c phase boundary shown in Fig. 3b. The dashed lines in Figs. 2b and 3b are the expected phase boundary between the M_c and T phases (similar to that shown in [10] for the PZN–8PT composition).

Thus, the *E*–*T* phase diagrams are plotted for the PZN–9PT and PZN–7PT compositions. Correlation between induced phase transitions in these crystals and the $PbTiO_3$ content *x* has been found. The M_c phase in PZN–9PT crystals appears to remain the ground state after the removal of the electric field, whereas the M_c phase in PZN–7PT crystals is metastable and transforms to the M_a phase after the removal of the electric field. It has been shown that the irreversible R(X)–M_c phase transition is possible only for compositions with $x > 7\%$.

This work was supported by the Russian Foundation for Basic Research (project no. 05-02-17835) and by the Chinese Academy of Sciences and the Shanghai Committee of Science and Technology (grant no. 02DJ14041).

REFERENCES

1. S.-E. Park and T. R. Shrout, J. Appl. Phys. **82**, 1804 (1997).
2. J. Kuwata, K. Uchino, and S. Nomura, Ferroelectrics **37**, 579 (1981).
3. H. Fu and R. E. Cohen, Nature **403**, 281 (2000).
4. B. K. Durbin, E. W. Jacobs, J. C. Hicks, *et al.*, Appl. Phys. Lett. **74**, 2848 (1999).
5. B. Noheda, Z. Zhong, D. E. Cox, *et al.*, Phys. Rev. B **65**, 224101 (2002).
6. B. Noheda, D. E. Cox, G. Shirane, *et al.*, Phys. Rev. Lett. **86**, 3891 (2001).
7. K. Ohwada, K. Hirota, P. Rehrig, *et al.*, J. Phys. Soc. Jpn. **70**, 2778 (2001).
8. R. Guo, L. E. Cross, S. E. Park, *et al.*, Phys. Rev. Lett. **84**, 5423 (2000).
9. D. Vanderbilt and M. H. Cohen, Phys. Rev. B **63**, 094108 (2001).
10. K. Ohwada, K. Hirota, P. Rehrig, *et al.*, cond-mat/0207726 (2002).
11. G. Xu, Z. Zhong, Y. Bing, *et al.*, Phys. Rev. B **67**, 104102 (2003).
12. P. M. Gehrig, W. Chen, Z.-G. Ye, *et al.*, cond-mat/0304289 (2003).
13. L. S. Kamzina, J. Xu, M. Shi, and X. Wu, Pis'ma Zh. Tekh. Fiz. **30** (23), 62 (2004) [Tech. Phys. Lett. **30**, 1002 (2004)].
14. Y. Uezu, Y. Yamada, K. Fujishiro, *et al.*, Ferroelectrics **217**, 319 (1998).
15. K. Fujishiro, R. Vloch, Y. Uezu, *et al.*, Jpn. J. Appl. Phys. **37**, 5246 (1999).
16. J. Xu, S. Fan, B. Lu, *et al.*, Jpn. J. Appl. Phys. **41**, 7000 (2002).
17. L. S. Kamzina and A. L. Korzhenevskiĭ, Pis'ma Zh. Éksp. Teor. Fiz. **50**, 146 (1989) [JETP Lett. **50**, 163 (1989)].

Translated by R. Tyapaev

JETP Letters, Vol. 81, No. 11, 2005, pp. 583–586. From Pis'ma v Zhurnal Éksperimental'noĭ i Teoreticheskoĭ Fiziki, Vol. 81, No. 11, 2005, pp. 717–720.
Original English Text Copyright © 2005 by Askerzade.

Anisotropy of the Upper Critical Field in MgB_2: The Two-Band Ginzburg–Landau Theory¶

I. N. Askerzade

Department of Physics, Faculty of Sciences, Ankara University, 06100 Tandogan, Ankara, Turkey
Institute of Physics, Azerbaijan National Academy of Sciences, Baku-AZ1143, Azerbaijan

Received March 18, 2005; in final form, May 4, 2005

The temperature dependence of the anisotropy parameter of the upper critical field $\gamma_{H_{c2}}(T) = H_{c2}^{\parallel}(T)/H_{c2}^{\perp}(T)$ is calculated using the two-band Ginzburg–Landau theory for layered superconductors. It is shown that the anisotropy parameter $\gamma(T)$ increases with decreasing temperature. The results of the calculations are in agreement with experimental data for single crystals of MgB_2 and with other calculations. © *2005 Pleiades Publishing, Inc.*

PACS numbers: 74.20.De

INTRODUCTION

Three years ago, superconductivity in magnesium diboride (MgB_2) was discovered at a critical temperature, namely, T_c = 39 K, that is the highest critical temperature for a simply binary compound [1]. The origin of superconductivity in this compound can be explained in the framework of the ordinary *e–ph* mechanism. The material shows a pronounced isotope effect [2]. Measurements of the nuclear spin–lattice relaxation rate also indicate that MgB_2 is phonon-mediated superconductor [3]. The unusual superconductivity in this compound is related to two distinct energy gaps associated with different parts of the Fermi surface. The larger gap (Δ_σ = 7 meV) originates from holelike carriers residing on two cylindrical Fermi surface sheets, derived from σ bonding of the p_{xy} boron orbital (σ-*band*). The smaller gap (Δ_π = 2 meV) originates from the two 3D sheets of electrons and holes derived from π bonding of the p_z orbitals (π-*band*) [4–6].

In MgB_2, the crystal structure as well as the electronic and phononic band structure are all far from isotropic [7]. This should lead to anisotropic superconducting state properties. The corresponding electron transport is very anisotropic (ρ_c/ρ_{ab} = 3.5 [8]): the plasma frequency for the σ band along the *c* (or *z*) axis is much smaller than that in the *ab* (*xy*) direction [9]. In a clean material, the layered structure dictates a strong anisotropy of the upper magnetic critical field $H_{c2}^{\parallel} \gg H_{c2}^{\perp}$. Their ratio at low temperatures reaches about six, while $H_{c2}^{\perp}$ is as low as 2–3 T [10]. On the other hand, for a dirty material, the anisotropy is decreased, but the magnitudes of both $H_{c2}^{\perp}$ and $H_{c2}^{\parallel}$ are strongly increased [11].

A pronounced temperature dependence of the anisotropy parameter γ_H of the upper critical field was calculated based on the microscopic two-band (TB) model [12–15]. It is well known that Ginzburg–Landau (GL) theory remains a powerful instrument for the study of the magnetic phase diagrams of superconductors. Isotropic GL theory with two *s*-wave order parameters was used for the calculation of H_{c2} [16], H_{c1} [17], and other superconducting state parameters [18] and achieved good agreement for bulk MgB_2 samples. In this study, we first present calculations of the anisotropy parameter γ of the upper critical field using TB GL theory for layered superconductors. It is shown that, in contrast to SB layered superconductors, TB superconductors reveal temperature-dependent anisotropy of the upper critical field.

BASIC EQUATIONS

The free-energy functional for TB layered superconductors can be written as [16–19]

$$F[\Psi_{1n}, \Psi_{2n}] = \sum_n \int d^2 r (F_{1n} + F_{1n,2n} + F_{2n} + F_{1n,1(n+1)} + F_{2n,2(n+1)} + H^2/8\pi), \quad (1)$$

with

$$F_{in} = \frac{\hbar^2}{4m_i}\left|\left(\nabla_{2d} - \frac{2\pi i A}{\Phi_0}\right)\Psi_{in}\right|^2 + \alpha_{i,n}(T)\Psi_{i,n}^2 + \frac{\beta_{i,n}}{2}\Psi_{i,n}^4, \quad (2)$$

¶ The text was submitted by the author in English.

$$F_{1n,2n} = \varepsilon(\Psi_{1,n}\Psi^*_{2,n} + \text{c.c.}) + \varepsilon_1\left(\left(\nabla_{2d} + \frac{2\pi iA}{\Phi_0}\right)\Psi^*_{1,n}\left(\nabla_{2d} - \frac{2\pi iA}{\Phi_0}\right)\Psi_{2,n} + \text{c.c.}\right), \quad (3)$$

$$F_{in,i(n+1)} = \frac{\hbar^2}{4m_i^c d^2}\left|\Psi_{in} - \Psi_{i,(n\pm1)}\exp\left(-i\frac{2\pi dA_z}{\Phi_0}\right)\right|^2, \quad (4)$$

where we choose *x*, *y*, and *z* lying along the *a*, *b*, and *c* crystallographic axes, respectively. Here, m_i denotes the effective mass of the carriers in the plane belonging to band *i* (*i* = 1; 2). F_{in} is the free energy of separate bands in the plane. The coefficient α is given as $\alpha_{in} = \gamma_i(T - T_{ci})$, which depends on temperature linearly; γ is the proportionality constant, while the coefficient β_{in} is independent of temperature. **H** is the external magnetic field and **H** = curl*A*. The quantities ε and ε_1 describe the interband interaction of two order parameters and their gradients, respectively. Due to the identical character of planes, we can write $\alpha_{in} = \alpha_i$, $\beta_{in} = \beta_i$, and *d* is the distance between planes.

The choice of the vector potential **A** as **A** = (0, *Hx*, 0) corresponds to the perpendicular component of the magnetic field **H** = (0, 0, *H*). In this case, the GL equations for TB layered superconductors can be reduced to

$$-\frac{\hbar^2}{4m_1}\left(\frac{d^2}{dx^2} - \frac{x^2}{l_s^4}\right)\Psi_1 + \alpha_1(T)\Psi_1 + \varepsilon\Psi_2 + \varepsilon_1\left(\frac{d^2}{dx^2} - \frac{x^2}{l_s^4}\right)\Psi_2 = 0, \quad (5)$$

$$-\frac{\hbar^2}{4m_2}\left(\frac{d^2}{dx^2} - \frac{x^2}{l_s^4}\right)\Psi_2 + \alpha_2(T)\Psi_2 + \varepsilon\Psi_1 + \varepsilon_1\left(\frac{d^2}{dx^2} - \frac{x^2}{l_s^4}\right)\Psi_1 = 0, \quad (6)$$

where $l_s^2 = \hbar c/2eH$ is the so-called magnetic length. Calculating $H_{c2}^{\perp}$ in a manner similar to [18] leads to

$$H_{c2}^{\perp}(T) = \Phi_0/2\pi\xi_{\perp}^2, \quad (7)$$

where the effective coherent length ξ_{eff} of TB superconductors is given by the expression

$$\xi_{\perp}^2 = \frac{\hbar^2}{4}[-(m_1\alpha_1(T) + m_2\alpha_2(T) + 8\varepsilon\varepsilon_1 m_1 m_2/\hbar^2) + \sqrt{(m_1\alpha_1(T) + m_2\alpha_2(T) + 8\varepsilon\varepsilon_1 m_1 m_2/\hbar^2)^2 - 4m_1 m_2(\alpha_1(T)\alpha_2(T) - \varepsilon^2)}]^{-1}. \quad (8)$$

At small values for the upper critical field $H_{c2}^{\perp}(T)$, the following is true:

$$H_{c2}^{\perp}(T) = -\frac{\hbar c}{2e}\frac{(\alpha_1(T)\alpha_2(T) - \varepsilon^2)}{\frac{\hbar^2}{4}\left[\frac{\alpha_1(T)}{m_2} + \frac{\alpha_2(T)}{m_1} + \frac{8\varepsilon\varepsilon_1}{\hbar^2}\right]}. \quad (9)$$

For the calculation $H_{c2}^{\parallel}$, we choose **H** = (0, *H*, 0) and **A** = (0, 0, –*Hx*). Then, the GL equations for TB superconductors are reduced to the following form:

$$-\frac{\hbar^2}{4m_1}\frac{d^2\Psi_1}{dx^2} + \alpha_1\Psi_1 + \varepsilon\Psi_2 + \varepsilon_1\frac{d^2\Psi_2}{dx^2} + 2\frac{\hbar^2}{4m_1^c d^2}\left(1 - \cos\frac{2\pi dHx}{\Phi_0}\right)\Psi_1 = 0, \quad (10)$$

$$-\frac{\hbar^2}{4m_2}\frac{d^2\Psi_2}{dx^2} + \alpha_2\Psi_2 + \varepsilon\Psi_1 + \varepsilon_1\frac{d^2\Psi_1}{dx^2} + 2\frac{\hbar^2}{4m_2^c d^2}\left(1 - \cos\frac{2\pi dHx}{\Phi_0}\right)\Psi_2 = 0, \quad (11)$$

By elimination, we can get equations for Ψ_1 and Ψ_2 from (10) and (11), which turn out to be identical (see [18]):

$$\frac{\hbar^2}{4m_1}\frac{\hbar^2}{4m_2}\frac{d^4\Psi_1}{dx^4} - \left(\frac{\hbar^2}{4m_2}\alpha_1 + \frac{\hbar^2}{4m_1}\alpha_2\right)\frac{d^2\Psi_1}{dx^2} + \alpha_1\alpha_2\Psi_1 + \left(1 - \cos\frac{2\pi Hx}{\Phi_0}\right) \times\left(2\frac{\hbar^2}{4m_1^c d^2}\left[-\frac{\hbar^2}{4m_2}\frac{d^2}{dx^2} + \alpha_2\right] + 2\frac{\hbar^2}{4m_2^c d^2}\left[-\frac{\hbar^2}{4m_1}\frac{d^2}{dx^2} + \alpha_1\right]\right)\Psi_1 = \left(\varepsilon^2 + 2\varepsilon\varepsilon_1\frac{d^2}{dx^2} + \varepsilon_1^2\frac{d^4}{dx^4}\right)\Psi_1. \quad (12)$$

By neglecting high derivatives of the order parameter ($d^4\Psi_1/dx^4$) and small terms, we can obtain the Mathieu

equation for the calculation of the upper critical field $H_{c2}^{\parallel}$:

$$-\left(\frac{\hbar^2}{4m_2}\alpha_1 + \frac{\hbar^2}{4m_1}\alpha_2 + 2\varepsilon\varepsilon_1\right)\frac{d^2\Psi_1}{dx^2}$$

$$+ 2\left(\frac{\hbar^2}{4m_1^c d^2}\alpha_2 + \frac{\hbar^2}{4m_2^c d^2}\alpha_1\right)\left(1 - \cos\frac{2\pi dHx}{\Phi_0}\right)\Psi_1 \quad (13)$$

$$= (\varepsilon^2 - \alpha_1\alpha_2)\Psi_1.$$

At a small magnetic field $H \ll \Phi_0/2\pi d^2$ and after expansion of cosines in Eq. (13), we can get a final expression for the anisotropy parameter of the upper critical field:

$$\gamma_{H_{c2}} = \frac{H_{c2}^{\parallel}}{H_{c2}^{\perp}}$$

$$= \left[\frac{x(T - T_{c1}) + (T - T_{c2}) + 8\varepsilon^2 x\eta T_c}{\frac{m_2}{m_2^c}x(T - T_{c1}) + \frac{m_1}{m_1^c}(T - T_{c2})}\right]^{1/2}. \quad (14)$$

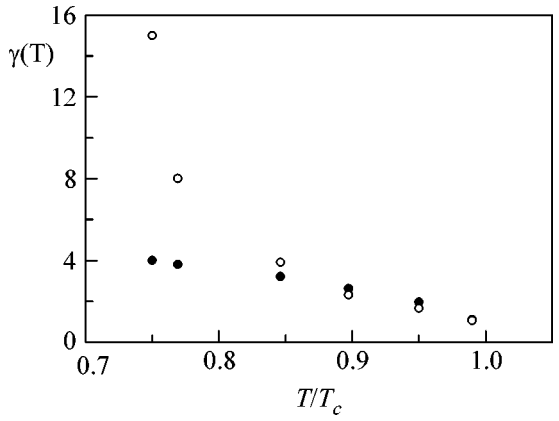

Temperature dependence of the anisotropy parameter $\gamma_{H_{c2}}$. The solid line is the TB GL theory for layered superconductors; the open symbols are experimental data from [21].

At a high magnetic field $H > \Phi_0/2\pi d^2$, the upper critical field $H_{c2}^{\parallel}$ can be defined from the lowest eigenvalue of the Mathieu equation [20] and is given by the following expression:

$$H_{c2}^{\parallel} = \frac{\Phi_0}{2\pi d}\frac{\alpha_2\frac{\hbar^2}{4m_1^c d^2} + \alpha_1\frac{\hbar^2}{4m_2^c d^2}}{\left(\left(\frac{\hbar^2}{4m_2}\alpha_1 + \frac{\hbar^2}{4m_1}\alpha_2 + 2\varepsilon\varepsilon_1\right)\left(\alpha_2\frac{\hbar^2}{4m_2^c d^2} + \alpha_1\frac{\hbar^2}{4m_1^c d^2} - \frac{\varepsilon^2 - \alpha_1\alpha_2}{2}\right)\right)^{1/2}}. \quad (15)$$

It means that

$$H_{c2}^{\parallel} < \frac{1}{(T - T^*)^{1/2}}, \quad (16)$$

where T^* is given by the following expression:

$$T^* = T_c - \frac{\hbar^2}{4m_1^c d^2\gamma_1} - \frac{\hbar^2}{4m_2^c d^2\gamma_2}.$$

RESULT AND DISCUSSION

In the figure, we plot the anisotropy parameter γ versus the reduced temperature T/T_c. Experimental results from Lyard [21] are denoted by the closed symbols. The open points denote the results of calculations from the TB layered GL theory presented above. Here, we used the following parameters: $T_{c1} = 20$ K, $T_{c2} = 10$ K, $\varepsilon^2 = 3/8$, $x = 3$, $\eta = -0.16$. The same parameters were also used in [16–18] to determine the temperature dependence of SC state parameters in the framework of isotropic TB GL theory. The anisotropy mass parameters for single crystals $m_2/m_2^c = 1.3$ and $m_1/m_1^c = 0.03$ are the same as in [22]. As shown in [16–18], isotropic GL theory gives a good description of the temperature dependences of measurable parameters of bulk samples of MgB_2. As follows from Eq. (14), the influence of the π (weak) band is effectively "switched off" and the anisotropy parameter is mainly defined by the σ (strong) band. As a consequence, at a small magnetic field, there is good agreement with experimental data on the investigation of anisotropy of the upper critical field. Increasing γ with decreasing temperature was observed experimentally by many groups [7, 10, 23, 24]. Thus, there is a consensus with regard to the understanding of the temperature behavior of γ.

At a high magnetic field, $H_{c2}^{\parallel}$ goes to infinity as $(T - T^*)^{1/2}$. This means that the orbital depairing effect of a magnetic field parallel to the layers does not destroy the superconductivity. This corresponds to the case where the cores of the vortices fit between the SC layers and the external magnetic field has no effects on the superconductivity. In fact, other magnetic mechanisms will limit the divergence. The divergence of $H_{c2}^{\parallel}$ at T^* will be removed by taking into account spin-orbit scattering [25] and the paramagnetic effect [26, 27]. Similar anisotropy of the upper critical field was observed for

the other possible class of TB superconductors—nonmagnetic borocarbides Y(Lu)Ni_2B_2C [28, 29].

Here, it is necessary to remark that similar two-band GL equations were recently discussed in [30]. However, in the equations presented in [30], terms similar to the intergradient interaction in Eqs. (5), (6) and (10), (11) are absent. As shown in [16–18], a maximal positive curvature of the upper critical field of bulk samples can be achieved by inclusion of an intergradient interaction. In the case of no intergradients of order parameters $\eta = 0$, the curvature reaches a maximum at the point of $0.5T_c$. Intergradient interaction shifts this maximum to a region close to the critical temperature. Such behavior is in good agreement with experimental data for bulk samples. As we can see from Eq. (14), in the case of anisotropic GL equations, intergradient terms also play a crucial role in the temperature dependence of the anisotropy parameter $\gamma_{H_{c2}}$.

Another version of the GL approximation was presented in [31]. This approach corresponds to an effective SB GL theory. In the framework of the theory [31], the ratio of order parameters is temperature- and field-independent; i.e., it is constant. This means that two-band GL theory is equivalent to the effective single-band approximation. In contrast to [31], in our consideration the ratio of order parameters is temperature- and field-dependent [16–18] (see also Eqs. (5), (6) and (10), (11)).

As shown by Bulaevskii [32] in the case of SB layered superconductors, the upper critical field is defined by the following expressions: $H_{c2}^{\parallel} = \Phi_0/2\pi\xi_\perp\xi_\parallel$ and $H_{c2}^{\perp} = \Phi_0/2\pi\xi_\parallel^2$. Note that, in this case, the anisotropy parameter $\gamma_{H_{c2}}$ is temperature-independent. As stated in the beginning, all coefficients α and β in the GL model are field-independent. Other generalizations of the considered model are related to the introduction of the field-dependent parameters α and β. The possible inclusion of field-dependent coefficients in the framework of TB GL is the subject of future investigations.

CONCLUSIONS

In summary, we have shown that experimental data on the anisotropy parameter $\gamma_{H_{c2}}(T)$ for MgB_2 can be described in the framework of TB layered GL theory at temperatures close to T_c, in contrast to SB layered superconductors, where the anisotropy parameter is temperature-independent. The presence of two order parameters with different dimensionalities plays a significant role in determining the temperature dependence of the anisotropy parameter $\gamma_{H_{c2}}(T)$.

I am grateful to Professors B. Unal, H. Yilmaz, and S. Atag at Ankara University for their hospitality. I am also grateful to Academician F.M. Hashimzade for support and to Drs. N. Guclu, A. Kilic, and Ms. Sc. student H. Shahin for discussions. This work has been financially supported by TUBITAK research grant no. 104T522.

REFERENCES

1. J. Nagamatsu, N. Nakagawa, T. Muranaka, *et al.*, Nature **410**, 63 (2001).
2. S. Budko, G. Lapertot, and C. Petrovic, Phys. Rev. Lett. **86**, 1877 (2001).
3. H. Kotegawa, K. Ishida, Y. Kitaoka, *et al.*, Phys. Rev. Lett. **87**, 127001 (2001).
4. A. Liu, I. I. Mazin, and J. Kortus, Phys. Rev. Lett. **87**, 087005 (2001).
5. H. J. Choi, D. Roundy, H. Sun, *et al.*, Nature **418**, 758 (2002).
6. J. Kortus, I. I. Mazin, K. D. Belashchenko, *et al.*, Phys. Rev. Lett. **86**, 4656 (2001).
7. M. Zehetmayer, M. Elstever, H. W. Weber, *et al.*, Phys. Rev. B **66**, 052505 (2002).
8. Yu. Eltsev, K. Nakao, S. Lee, *et al.*, Phys. Rev. B **66**, 180504(R) (2002).
9. A. Brinkman, A. A. Golubov, H. Rogalla, *et al.*, Phys. Rev. B **65**, 180517 (2002).
10. V. G. Kogan and S. L. Budko, Physica C (Amsterdam) **385**, 131 (2003).
11. A. Gurevich, S. Patnaik, V. Braccini, *et al.*, Supercond. Sci. Technol. **17**, 278 (2004).
12. A. Gurevich, Phys. Rev. B **67**, 184515 (2003).
13. A. A. Golubov and A. E. Koshelev, Phys. Rev. B **68**, 104503 (2003).
14. V. G. Kogan, Phys. Rev. B **66**, 020509 (2002).
15. A. A. Golubov, A. Brinkman, O. V. Dolgov, *et al.*, Phys. Rev. B **66**, 054524 (2002).
16. I. N. Askerzade, A. Gencer, and N. Güçlü, Supercond. Sci. Technol. **15**, L13 (2002).
17. I. N. Askerzade, A. Gencer, N. Güçlü, and A. Kiliç, Supercond. Sci. Technol. **15**, L17 (2002).
18. I. N. Askerzade, Physica C (Amsterdam) **397**, 99 (2003).
19. H. Doh, M. Sigrist, B. K. Chao, and Sung-Ik Lee, Phys. Rev. Lett. **83**, 5350 (1999).
20. *Handbook of Mathematical Functions*, Ed. by M. Abramowitz and I. A. Stegun, 2nd ed. (Dover, New York, 1972; Nauka, Moscow, 1979).
21. L. Lyard, P. Samuely, P. Szabo, *et al.*, Phys. Rev. B **66**, 180502 (2002).
22. P. Miranovich *et al.*, J. Phys. Soc. Jpn. **72**, 221 (2003).
23. M. Angst, R. Puzniak, A. Wisnievski, *et al.*, Phys. Rev. Lett. **88**, 167004 (2002).
24. H. Bando, Y. Yamaguchi, N. Shirakawa, and T. Yanagiawa, Physica C (Amsterdam) **412**, 258 (2004).
25. R. A. Klemm, M. R. Beasley, and A. Luther, Phys. Rev. B **12**, 877 (1975).
26. B. S. Chandrasekhar, Appl. Phys. Lett. **1**, 7 (1962).
27. V. Clogston, Phys. Rev. Lett. **9**, 266 (1962).
28. S.-L. Drechsler *et al.*, Physica C (Amsterdam) **317–318**, 117 (1999).
29. S.-L. Drechsler, H. Rosner, I. Opahle, *et al.*, Physica C (Amsterdam) **408–410**, 104 (2004).
30. V. H. Dao and M. E. Zhitomisrsky, cond-mat/0504053; Eur. J. Phys. B (in press).
31. A. E. Koshelev and A. A. Golubov, Phys. Rev. Lett. **92**, 107008 (2004).
32. L. N. Bulaevskii, Sov. Phys. JETP **37**, 1133 (1973).

JETP Letters, Vol. 81, No. 11, 2005, pp. 587–589. Translated from Pis'ma v Zhurnal Éksperimental'noĭ i Teoreticheskoĭ Fiziki, Vol. 81, No. 11, 2005, pp. 721–723.
Original Russian Text Copyright © 2005 by D. Gritsenko, Shaĭmeev, Lamin, Pchelyakov, V. Gritsenko, Lifshits.

Two-Band Conductivity of ZrO_2 Synthesized by Molecular Beam Epitaxy

D. V. Gritsenko[1], S. S. Shaĭmeev[1], M. A. Lamin[1], O. P. Pchelyakov[1], V. A. Gritsenko[1], and V. G. Lifshits[2]

[1] *Institute of Semiconductor Physics, Siberian Division, Russian Academy of Sciences, Novosibirsk, 630090 Russia*
e-mail: grits@isp.nsc.ru

[2] *Institute for Automation and Control Processes, Far East Division, Russian Academy of Sciences, Vladivostok, 690041 Russia*

Received May 5, 2005

Using experiments on the injection of minority carriers from *n*- and *p*-type silicon, the contribution of electrons and holes to the conductivity of ZrO_2 in the $Si/ZrO_2/Al$ structure is determined. It is found that electrons and holes make a contribution to the conductivity of ZrO_2, so that ZrO_2 exhibits two-band conductivity. © *2005 Pleiades Publishing, Inc.*

PACS numbers: 77.22.Jp, 77.55.+f, 77.84.Bw

Scaling silicon metal–insulator–semiconductor (MIS) devices is accompanied by a decrease in the channel length and in the thickness of the gate dielectric. Thermal silicon dioxide has been used as a gate dielectric for 40 years. A decrease in the SiO_2 thickness to 10–15 Å is accompanied by an unacceptably high leakage current. The main approach to decreasing the leakage current through the gate dielectric consists in the replacement of silicon dioxide by so-called alternative dielectrics (dielectrics with a high dielectric constant, i.e., high-k dielectrics). The use of alternative dielectrics allows the physical dielectric thickness to be increased and, in this way, the tunnel current to be suppressed [1, 2]. Zirconium dioxide is one of the most promising alternative dielectrics. ZrO_2 has a high dielectric constant ($\varepsilon = 25$), a wide band gap E_g = 5.5 eV, high barriers at the Si/ZrO_2 interface, and high thermodynamic stability of the interface with silicon [3]. In addition, the difference in the lattice constants of Si and ZrO_2 does not exceed 2.1% [4]. The latter circumstance opens the possibility of synthesizing ZrO_2 on Si by molecular beam epitaxy.

In the general case, the contribution to the conductivity of a dielectric is made by electrons and holes [5–7]. The detection of the sign of charge carriers in semiconductors is carried out using either the Hall effect or the thermal emf. In dielectrics, these methods are inapplicable because of the negligibly small concentration of mobile carriers. The goal of this work is to determine the contribution of electrons and holes to the conductivity of dielectric ZrO_2 films synthesized by molecular beam epitaxy in a $Si/ZrO_2/Al$ MIS structure.

We studied $Si/ZrO_2/Al$ structures with *n*- and *p*-type silicon(100) with a resistivity of ≈10 Ω cm. The Si/ZrO_2 structures were obtained in an ultrahigh-vacuum setup Katun'-V by molecular beam epitaxy. High-temperature thermal heating was performed in the setup with the aim of obtaining an atomically clean Si surface. To obtain a ZrO_2 vapor, an electron-beam evaporator was used with the electron beam current I = 250 mA, the voltage U = 6 kV, and magnetic sweep of the electron beam. The target temperature reached 2800–3200°C. The target was single-crystal ZrO_2.

Perfect single-crystal ZrO_2 films (according to electron diffraction data) were obtained on the atomically clean Si surface at substrate temperatures from 400 to 800°C. According to ellipsometric measurements, the ZrO_2 film thickness was in the range 110–300 Å. The measurements of current–voltage and capacity–voltage (100-kHz frequency) characteristics were performed at room temperature. Illumination was performed using a tungsten lamp.

The current–voltage characteristics of the *p*-$Si/ZrO_2/Al$ structure are presented in Fig. 1. The characteristics were obtained at two polarities of the voltage across the metal: in the enhancement mode (a negative potential at Al) and in the depletion mode (a positive potential at Al). In the depletion mode with a positive potential at Al, the saturation of the current is observed in the dark and the current relatively weakly depends on the voltage. The current increases upon switching illumination. The saturation of the current in the depletion mode is related to the injection of minority charge carriers from silicon into the dielectric. In the case of a negative potential at the metal in the enhancement mode, the current increases exponentially with increasing potential. Illumination does not affect the current.

0021-3640/05/8111-0587$26.00 © 2005 Pleiades Publishing, Inc.

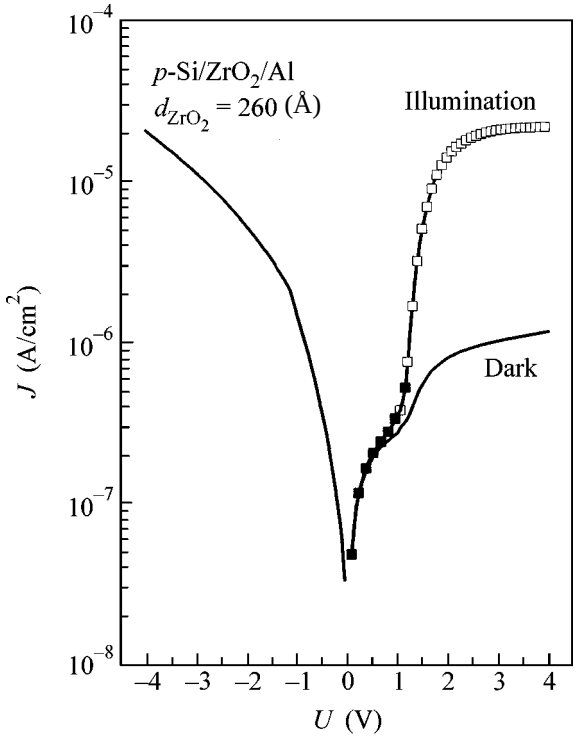

Fig. 1. Current–voltage characteristics of the p-Si/ZrO$_2$/Al structure obtained (solid lines) in the depletion and enhancement modes and (points) in the depletion mode with illumination.

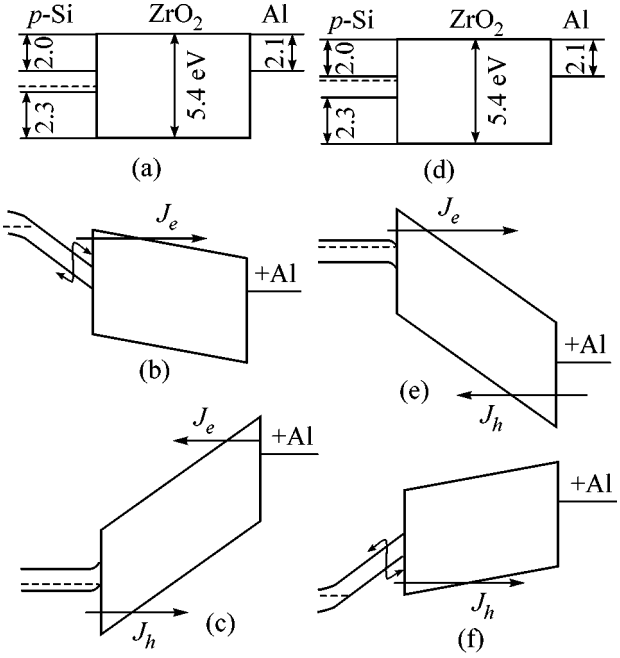

Fig. 2. Energy diagrams of [(a), (b), and (c)] p-Si/ZrO$_2$/Al and [(d), (e), and (f)] n-Si/ZrO$_2$/Al structures [(a) and (d)] with no applied voltage, [(b) and (e)] in the depletion mode, and [(c) and (f)] in the enhancement mode.

In this case, virtually all of the applied voltage drops across the dielectric.

The energy diagram of the Si/ZrO$_2$/Al structure according to the data of photoemission measurements [8] is presented for p- and n-type silicon in Figs. 2a–2f. Figures 2a and 2d show the energy diagram in the flat-band mode without an applied voltage. The ZrO$_2$ band-gap width is 5.4 eV, and the barrier for electrons at the Si/ZrO$_2$ interface is 2.0 eV. The energy diagrams of the p-Si/ZrO$_2$/Al and n-Si/ZrO$_2$/Al structures are presented in Fig. 2 for a positive potential on the metal (Figs. 2b, 2e) and for a negative potential on the metal (Figs. 2c, 2f).

In the depletion mode in the p-Si/ZrO$_2$/Al structure, the applied voltage is divided between the dielectric and the nonequilibrium depletion layer (Fig. 2b). This circumstance is caused by the fact that the injection current of minority carriers (electrons) is comparable with their generation rate in silicon. Illumination leads to an increase in the generation rate of minority carriers, to narrowing of the thickness of the depleted layer, to a decrease in the voltage drop across the depletion layer, to an increase in the voltage drop across the dielectric, and, hence, to an increase in the dielectric conductivity. Thus, the behavior of the current–voltage characteristics in the depletion mode indicate that the injection of electrons from silicon makes the main contribution to the ZrO$_2$ conductivity at a positive potential at aluminum. The flux of holes from the dielectric to silicon is negligibly small as compared to the opposite flux of electrons from silicon to the dielectric. In the case of a negative potential at the metal in the enhancement mode (Fig. 2c), the entire applied voltage drops across the dielectric. It is natural to suggest that the conductivity of the dielectric in this case is also due to electrons injected from aluminum, because the barriers for electrons at the Si/ZrO$_2$ and Al/ZrO$_2$ interfaces are close in height (Figs. 2a, 2d).

A similar behavior of the current–voltage characteristics is observed in the n-Si/ZrO$_2$/Al structure (Fig. 3). In the case of a positive potential at the metal in the enhancement mode, the entire applied voltage drops across the dielectric (Fig. 2e). It is natural to suggest that charge transfer in the dielectric in this case, as well as in the p-Si/ZrO$_2$/Al structure, is due to electrons injected from silicon (Fig. 2e). In the depletion mode with a negative potential at the metal, the saturation of the current–voltage characteristics is observed (Fig. 3). Illumination leads to an increase in the current level. This means that the nonequilibrium depletion layer is developed by virtue of the injection of holes from silicon into the dielectric (Fig. 2f). Thus, the current to n-Si at the Si/ZrO$_2$ interface is transferred by holes injected from silicon into the dielectric.

It is natural to suggest that charge transfer in the dielectric in the p-Si/ZrO$_2$/Al structure at a negative

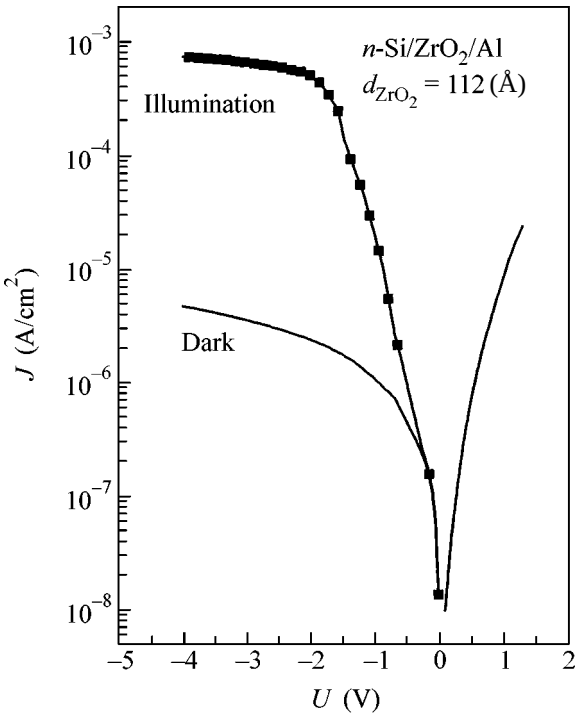

Fig. 3. Same as in Fig. 1, but for the n-Si/ZrO_2/Al structure.

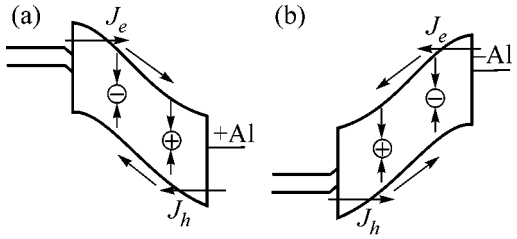

Fig. 4. Schematic diagram of current passage in the Si/ZrO_2/Al structure for (a) positive and (b) negative potentials on the metal. It is assumed that the generation rate of minority carriers in the depletion mode exceeds the rate of their injection into the dielectric.

potential at the metal is also performed by holes injected from silicon (Fig. 2c). In the general case, electrons are injected into the dielectric from a negatively biased electrode and holes are injected into the dielectric from a positively biased electrode. The experiment indicates that ZrO_2 has traps [9, 10]. A two-band model of electron and hole current passage in the Si/ZrO_2/Al structure is presented in Fig. 4 for two polarities of the potential at the metal. According to this model, ZrO_2 contains electron and hole traps, which serve as recombination centers. Consider current passage in more detail for positive polarity of the potential at the metal (Fig. 4a). Electrons are injected from silicon into ZrO_2 and are captured in the traps. Some of electrons are ionized from the traps by the Frenkel mechanism or by the multiphonon mechanism [7, 10]. Next, conduction-band electrons recombine with holes captured in the traps in the vicinity of the anode (metal). Holes from the positively biased metal are injected into the valence band of the dielectric, are captured in the traps, and recombine with free electrons. Some of hole traps are ionized, and the free holes move toward the silicon and recombine with localized electrons. The above model explains the development of a nonequilibrium depletion layer in n-type and p-type silicon due to the injection of minority carriers into the dielectric. A similar pattern is observed for a negative potential at the metal (Fig. 4). The model suggested above is similar to the model of current passage in silicon nitride [6, 7, 11].

This work was supported by the Siberian Division of the Russian Academy of Sciences, integration project no. 116.

REFERENCES

1. A. I. Kingon, J.-P. Maria, and S. K. Streiffor, Nature **406**, 1032 (2000).
2. G. D. Wilk, R. M. Wallace, and J. M. Anthony, J. Appl. Phys. **89**, 5243 (2001).
3. M. Gutowski, J. E. Jaffe, C. L. Liu, *et al.*, Appl. Phys. Lett. **80**, 1897 (2002).
4. Y.-Z. Hu and S.-P. Tau, J. Vac. Sci. Technol. B **19**, 1706 (2001).
5. V. A. Gritsenko, E. E. Meerson, and Yu. N. Morokov, Phys. Rev. B **57**, R2081 (1998).
6. K. A. Nasyrov, Yu. N. Novikov, V. A. Gritsenko, *et al.*, Pis'ma Zh. Éksp. Teor. Fiz. **77**, 455 (2003) [JETP Lett. **77**, 385 (2003)].
7. K. A. Nasyrov, V. A. Gritsenko, Yu. N. Novikov, *et al.*, J. Appl. Phys. **96**, 4293 (2004).
8. V. V. Afanas'ev, M. Houssa, and A. Stesmans, J. Appl. Phys. **91**, 3079 (2002).
9. M. Houssa, M. Tuominen, M. Naili, *et al.*, J. Appl. Phys. **87**, 8615 (2000).
10. S. Ramanathan, C.-M. Park, and P.-C. Mcintyre, J. Appl. Phys. **91**, 4521 (2002).
11. A. S. Ginovker, V. A. Gritsenko, and S. P. Sinitsa, Phys. Status Solidi B **26**, 489 (1974).

Translated by A. Bagatur'yants

JETP Letters, Vol. 81, No. 11, 2005, pp. 590–593. Translated from Pis'ma v Zhurnal Éksperimental'noĭ i Teoreticheskoĭ Fiziki, Vol. 81, No. 11, 2005, pp. 724–727.
Original Russian Text Copyright © 2005 by Kadomtseva, Popov, Vorob'ev, Ivanov, Mukhin, Balbashov.

Specific Features of the Magnetic Field–Induced Orientational Transition in $EuMnO_3$

A. M. Kadomtseva[1], Yu. F. Popov[1], G. P. Vorob'ev[1], V. Yu. Ivanov[2], A. A. Mukhin[2], and A. M. Balbashov[3]

[1] *Moscow State University, Vorob'evy gory, Moscow, 119992 Russia*
e-mail: kadomts@plms.phys.msu.ru
[2] *General Physics Institute, Russian Academy of Sciences, Moscow, 119991 Russia*
[3] *Moscow Power Engineering Institute (Technical University), Moscow, 105835 Russia*
Received May 6, 2005

It is found that the spin-flop transition in $EuMnO_3$ manganite induced by a magnetic field H parallel to the b axis is accompanied not only by a magnetization jump and magnetostriction anomalies but also by the appearance of electric polarization in the vicinity of the transition field $H_{cr} \sim 200$ kOe. This phenomenon can be associated with the occurrence of magnetically inhomogeneous (modulated) states in the vicinity of H_{cr}. In these states, the system loses the center of symmetry, which allows for the appearance of the polarization. The formation of such states in a magnetic field is caused by the general tendency of the occurrence of magnetically inhomogeneous (incommensurate) structures in the $RMnO_3$ series due to the frustration of exchange interactions with decreasing ionic radius of the rare-earth ion R starting with R = Eu. © *2005 Pleiades Publishing, Inc.*

PACS numbers: 75.80.+q

INTRODUCTION

Rare-earth manganites $RMnO_3$ having an orthorhombic distorted perovskite structure for R from La to Dy (space group *Pbnm*) are base compounds for obtaining materials with colossal magnetoresistance by means of their doping with Ca or Sr. Recently, new interesting properties have been revealed in some $RMnO_3$ manganites. These properties are associated with the appearance of electric polarization in these manganites in the region of the existence of modulated spin structures [1, 2] arising due to the frustration of exchange interactions as the ionic radius of the rare-earth ion R decreases. It was found [1–6] that a spatially modulated incommensurate magnetic structure forms for R = Eu, Gd, Tb, and Dy below the Neél point. As the temperature further decreases, this structure transforms either into a conventional canted antiferromagnetic structure of the A_YF_Z type (Eu, Gd) [2–6] or into a commensurate modulated structure at $T = T_{lock}$ (Tb, Dy) [1–4]. The appearance of electric polarization and of a magnetoelectric effect, whose mechanisms were related to the modulation of the crystal structure induced by the magnetoelastic interaction, was observed in $TbMnO_3$ and $DyMnO_3$ upon transition from the incommensurate structure to the commensurate modulated structure at $T_{lock} \sim 20$ K [1, 2]. The temperature dependence of the dielectric constant in these manganites exhibited anomalies at T_{lock}, which manifested a strong anisotropy depending on the electric field orientation. Anomalies in the dielectric constant were also observed for single crystals of $GdMnO_3$ [2, 7, 8] and $EuMnO_3$ [2] in the vicinity of the transition temperature T_{CA} from the incommensurate modulated structure to the antiferromagnetic canted state. In this case, a spontaneous electric polarization in $GdMnO_3$ was not observed in [2], but it was observed in [7]. We have showed recently [8] that a magnetic field $H \parallel b$ ($H_{cr} \sim 40$ kOe) applied to $GdMnO_3$ gives rise to a change in the electric polarization ΔP along the a and b crystal axes and that the sign of ΔP depends on the sign of the electric field in which the crystal is cooled. As for $EuMnO_3$, the existence of electric polarization and magnetoelectric interactions has not been detected for this manganite [2]. Nevertheless, it has been of interest to perform a comprehensive study of a $EuMnO_3$ single crystal in strong magnetic fields by analogy with $GdMnO_3$ [8] with the aim of revealing a possible tendency towards the occurrence of magnetoelectric interactions in this crystal.

According to [6], an incommensurate modulated antiferromagnetic structure arises in $EuMnO_3$ below $T_N \sim 50$ K; this structure transforms at a temperature $T_{CA} \sim 43$ K into a canted antiferromagnetic state with a transverse, weakly ferromagnetic moment along the c axis of the rhombohedral crystal (A_YF_Z).

It was also of interest to compare the properties of $EuMnO_3$ and $SmMnO_3$. In the latter case, a homogeneous magnetic structure A_YF_Z was observed at all temperatures $T < T_N = 60$ K.

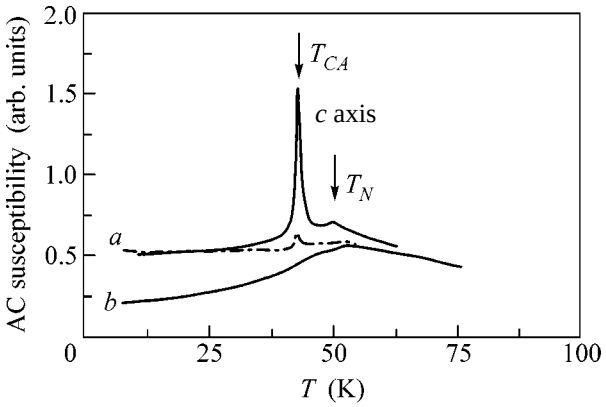

Fig. 1. Temperature dependences of the ac susceptibility in a $EuMnO_3$ single crystal along the main crystallographic directions.

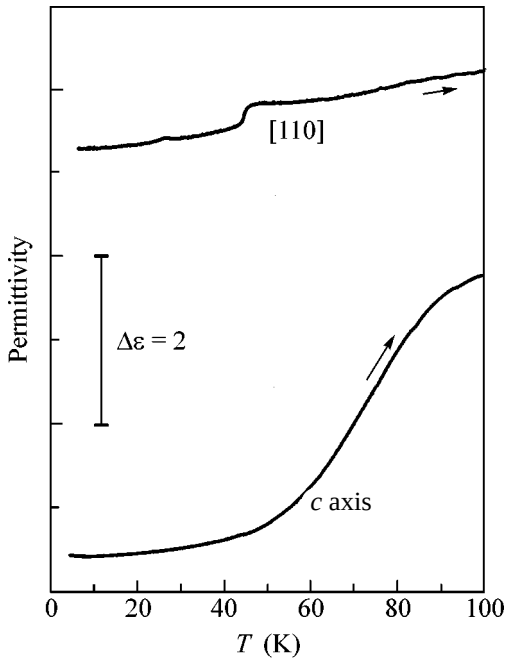

Fig. 2. Temperature dependences of the dielectric constant of a $EuMnO_3$ single crystal measured at a frequency of 1 MHz along the [001] and [110] crystallographic directions.

EXPERIMENTAL RESULTS AND DISCUSSION

Single crystals $EuMnO_3$ and $SmMnO_3$ were grown by zone melting with optical heat. X-ray powder diffraction analysis showed that the crystals are homogeneous and possess an orthorhombic crystal structure of the *Pbnm* type. The orientation of the crystals was determined by an x-ray diffraction method.

The ac magnetic susceptibility was measured at a frequency of ~240 Hz with an amplitude of an alternate magnetic field on the order of several fractions of an oersted in the temperature range 4.2–60 K. A weak peak at $T_N = 50$ K and a sharp peak at $T_{CA} = 43$ K were observed in the temperature dependence of the $EuMnO_3$ susceptibility along the *c* axis (Fig. 1) upon transition to the weakly ferromagnetic state A_YF_Z from the incommensurate modulated antiferromagnetic structure.

Measurements of the temperature dependence of the dielectric constant were also performed at a frequency of 1 MHz using the method described in [8]. A weak step was observed in the susceptibility at $E \parallel [110]$ (between the *a* and *b* axes) at the transition temperature T_{CA}, whereas no anomaly was observed along the *c* axis (Fig. 2), in agreement with the data reported in [1].

Studies of the magnetic, magnetoelectric, and magnetoelastic properties of $EuMnO_3$ single crystals were performed in the temperature range 4.2–50 K in pulsed magnetic fields up to 250 kOe.

When measuring the magnetization along the *b* axis in a strong magnetic field ($H_{cr} \sim 200$ kOe) $H \parallel b$, we observed a magnetization jump of ~6 emu/g evidently associated with the spin-flop reorientation phase transition $A_YF_Z \longrightarrow A_ZF_Y$ (Fig. 3). The threshold field of the spin-reorientation transition $H_{cr} \sim 200$ kOe agrees with the estimate of this field obtained from the antiferromagnetic resonance frequencies, which have approximately the same value as in $SmMnO_3$ ($\nu_{AFMR} \approx 20$ cm^{-1}) [6]. Jumps in the field dependence of the longitudinal magnetostriction along the *a*, *b*, and *c* axes were also observed at the same value of the magnetic field $H_{cr} \sim 200$ kOe applied along the *b* crystal axis. As is evident in Fig. 4, which presents the dependences of the longitudinal magnetostriction on the magnetic field along the *b* axis that arose upon the reorientation transition $A_YF_Z \longrightarrow A_ZF_Y$, the magnetostriction deformations exhibited a strong field hysteresis.

It was found that field-induced spin reorientation led to the appearance of electric polarization along the *a*, *b*,

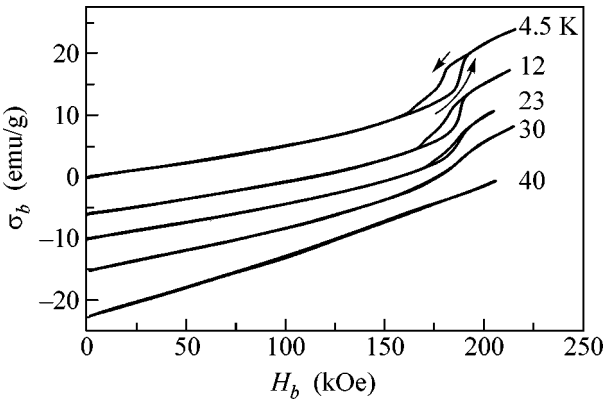

Fig. 3. Magnetization curves along the *b* axis in a $EuMnO_3$ single crystal at various temperatures (the origin of the ordinate axis for curves at $T = 12$, 23, 30, and 45 K is shifted down by 7, 10, 15, and 22.5 emu/g, respectively).

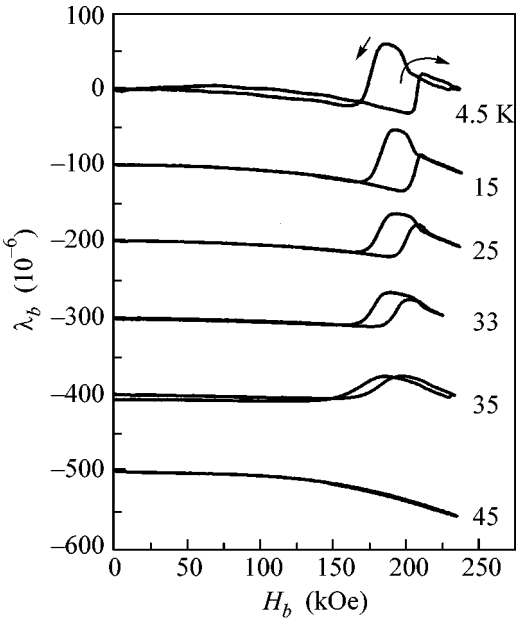

Fig. 4. Field dependences of the longitudinal magnetostriction of a $EuMnO_3$ single crystal at $H \parallel b$. The origin for various curves is shifted along the ordinate axis.

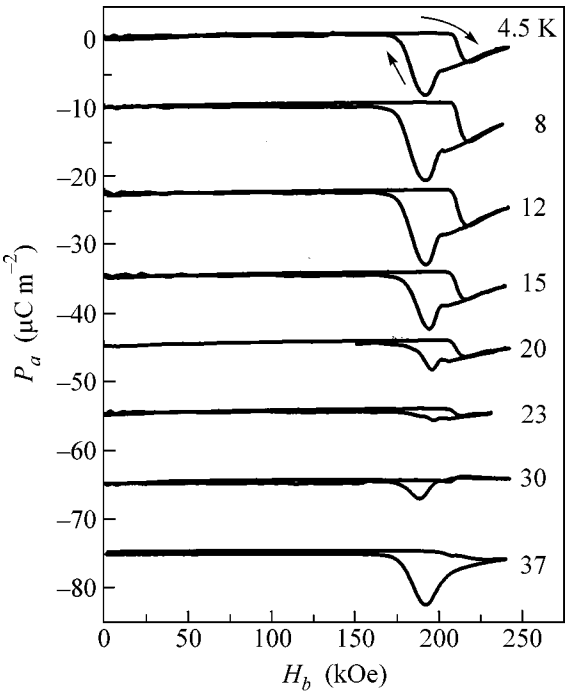

Fig. 5. Field dependences of the polarization of a $EuMnO_3$ single crystal along the *a* axis at $H \parallel b$. The origin for various curves is shifted along the ordinate axis.

and *c* crystal axes in the vicinity of $H_{cr} \sim 200$ kOe. This polarization reached a maximum value along the *a* crystal axis (Fig. 5) and vanished above $T_{CA} \sim 40$ K. An unusual increase in the value of the electric polarization was observed in the dependence $P_b(H_b)$ in the temperature range 27–40 K. A strong field hysteresis was observed in the dependence of the electric polarization $P_{a,b,c}(H_b)$; as the field decreased, the magnitude of anomalies substantially increased and were much more pronounced than in the case of increasing field. Though the magnetic field–induced electric polarization was small (~1–10 μC/m^2), its appearance is of crucial importance in understanding the nature of the magnetoelectric interactions in $RMnO_3$.

The appearance of electric polarization in the region of the spin-flop transition in $EuMnO_3$ can be associated with the occurrence of magnetically inhomogeneous (modulated) states in which the system loses its center of symmetry, which allows for the appearance of polarization [9]. Since a spontaneous incommensurate modulated structure occurs in $EuMnO_3$ in the temperature range 43–50 K, the tendency for its formation is also evidently revealed in the magnetic field in the region of the spin-flop transition. The fact that the polarization differs from zero only in the region of the spin-flop transition reflects the fact of the existence of a spin-modulated state, which disappears upon the transition to the homogeneous canted state A_ZF_Y when the field becomes $H > H_{cr}$. It is possible that the occurrence of such a spin-modulated state can be considered a manifestation of the instability of the antiferromagnetic layered structure of the *A* type, when the ferromagnetic layer with a magnetization opposite to the external field breaks down into a greater number of sublattices.

Considering that the field-induced reorientation transition in $EuMnO_3$ favors the manifestation of magnetically inhomogeneous (modulated) states and the related magnetoelectric interactions, it will be of interest to elucidate the possibility of an analogous effect in the case of spin reorientation in $RMnO_3$ crystals with other rare-earth ions, for example, the nearest $SmMnO_3$, in which ordering already gives rise to a homogeneous canted antiferromagnetic structure. Our measurements showed that a $SmMnO_3$ single crystal at $H \parallel b$ exhibited anomalies in magnetostriction deformations in the field $H_{cr} \sim 200$ kOe associated with the induced spin-flop transition (Fig. 6); however, no electric polarization was manifested in this case. This indicates that the magnetic structure of $SmMnO_3$ is homogeneous at all temperatures below T_N, and, as distinct from $EuMnO_3$, the tendency for the formation of a modulated magnetic structure in a magnetic field is already completely suppressed here.

CONCLUSIONS

Thus, the studies performed in this work showed that the spin-flop transition in $EuMnO_3$ in a magnetic field $H \parallel b$ is accompanied by the appearance of electric polarization in the vicinity of the transition field. This

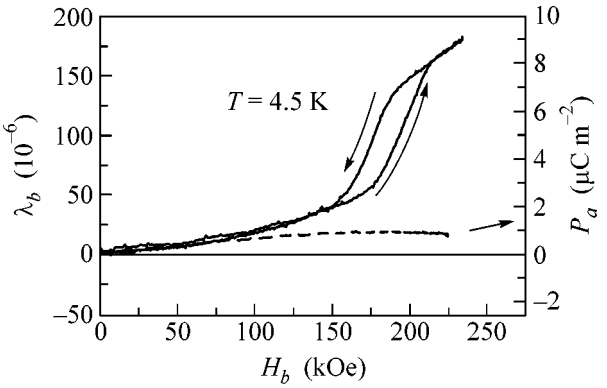

Fig. 6. Dependences of the magnetostriction along the *b* axis and the polarization along the *a* axis on the magnetic field $H \parallel b$ in a $SmMnO_3$ single crystal.

effect can be explained by the instability of a homogeneous canted structure and by the induction of magnetically inhomogeneous (modulated) states in the vicinity of H_{cr}. In this case, the system loses its center of symmetry, and the appearance of electric polarization becomes possible. The development of such an instability of homogeneous states in a magnetic field is related to the general tendency for magnetically inhomogeneous (incommensurate) structures to occur in the $RMnO_3$ series due to the frustration of exchange interactions with decreasing ionic radius of the rare-earth ion R, starting with R = Eu. For the preceding rare-earth ion R = Sm of the $RMnO_3$ series, the above effect has not been observed.

This work was supported in part by the Russian Foundation for Basic Research, project nos. 04-02-16592, 03-02-16445, 03-02-16759, and 04-02-81046-Bel2004.

REFERENCES

1. T. Kimura, T. Goto, H. Shintani, *et al.*, Nature **426**, 55 (2003).
2. T. Goto, T. Kimura, G. Lawes, *et al.*, Phys. Rev. Lett. **92**, 257 201 (2004).
3. S. Quezel, R. Tcheou, J. Rossat-Mignod, *et al.*, Physica B & C (Amsterdam) **86–88**, 916 (1977).
4. T. Kimura, S. Ishihara, H. Shintani, *et al.*, Phys. Rev. B **68**, 060 403 (2003).
5. J. Hemberger, S. L. Lobina, H.-A. Krug von Nidda, *et al.*, Phys. Rev. B **70**, 024414 (2004).
6. A. A. Mukhin, V. Yu. Ivanov, V. D. Travkin, *et al.*, J. Magn. Magn. Mater. **272–276**, 96 (2004).
7. H. Kuwahara, K. Noda, J. Nagayama, and S. Nakamura, in *Proceedings of 124th International Conference on Strongly Correlated Electron Systems* (2004).
8. A. M. Kadomtseva, Yu. F. Popov, G. P. Vorob'ev, *et al.*, Pis'ma Zh. Éksp. Teor. Fiz. **81**, 22 (2005) [JETP Lett. **81**, 19 (2005)].
9. V. G. Bar'yakhtar, V. A. L'vov, and D. A. Yablonskiĭ, Pis'ma Zh. Éksp. Teor. Fiz. **37**, 565 (1983) [JETP Lett. **37**, 673 (1983)]; V. G. Bar'yakhtar, E. P. Stefanovskiĭ, and D. A. Yablonskiĭ, Pis'ma Zh. Éksp. Teor. Fiz. **42**, 258 (1985) [JETP Lett. **42**, 317 (1985)].

Translated by A. Bagatur'yants

JETP Letters, Vol. 81, No. 11, 2005, pp. 594–598. From Pis'ma v Zhurnal Éksperimental'noĭ i Teoreticheskoĭ Fiziki, Vol. 81, No. 11, 2005, pp. 728–732.
Original English Text Copyright © 2005 by Fateev, Litvinov.

On Differential Equation on Four-Point Correlation Function in the Conformal Toda Field Theory¶

V. A. Fateev[1, 2] and A. V. Litvinov[1]

[1] *Landau Institute for Theoretical Physics, Russian Academy of Sciences, Chernogolovka, Moscow region, 142432 Russia*
e-mail: litvinov@itp.ac.ru

[2] *Laboratoire de Physique Théorique et Astroparticules, Université Montpelier II, Pl.E. Bataillon, 34095 Montpelier, France*

Received May 5, 2005

The properties of completely degenerate fields in the conformal Toda field theory are studied. It is shown that a generic four-point correlation function that contains only one such field does not satisfy an ordinary differential equation, in contrast to the Liouville field theory. Some additional assumptions for other fields are required. Under these assumptions, we write such a differential equation and solve it explicitly. We use the fusion properties of the operator algebra to derive a special set of three-point correlation functions. The result agrees with the semiclassical calculations. © *2005 Pleiades Publishing, Inc.*

PACS numbers: 11.25.Hf

There are several motivations to study the conformal Toda field theory. This theory has a nontrivial geometric formulation [1] and, hence, plays a significant role in the quantization of noncritical strings with extended symmetry [2]. It also provides an example of a theory with higher spin symmetry and, hence, has its own interest. The algebra of generators of this symmetry (*W* algebra) is closely related to a rather general class of integrable systems. It can be derived by quantization of the second Hamiltonian structure of the generalized KdV-type equations associated with Lie algebras [3, 4]. This symmetry manifests itself in rational conformal field theories (CFT), which describe the critical behavior of many interesting statistical systems, such as, for example, Z_n Ising models (parafermionic CFT [5]), tricritical Ising and Z_3 Potts models, Ashkin–Teller models, etc. Though it has been known for many years and has been applied to many interesting problems in contemporary mathematics and physics, the W symmetry is still rather mysterious and needs further detailed study. The conformal Toda field theory with a real coupling constant is irrational CFT, which has a simple Lagrangian formulation and possesses this symmetry. In this Letter, we find a special set of three-point correlation functions of the exponential fields in this theory, but the general formula is not known to us at present.

The action of the conformal Toda field theory has the form

$$\mathcal{A} = \int d^2x\left(\frac{1}{8\pi}(\partial\varphi)^2 + \mu\sum_{k=1}^{r} e^{b(e_k,\varphi)}\right), \qquad (1)$$

where e_k are the simple roots of Lie algebra $\mathcal{G}$ and (e_k, φ) denotes the scalar product of the roots with the r component scalar field $\varphi = (\varphi_1, \ldots, \varphi_r)$. We consider the case $\mathcal{G} = sl(n)$, $r = n - 1$. The conserved holomorphic W currents W_j, which form a closed W algebra in this case, have spins $j = 2, \ldots, n$ and can be expressed in terms of φ by the relation[1]

$$\prod_{i=0}^{n-1}(q\partial + (h_{n-i}, \partial\varphi)) = \sum_{k=0}^{n} W_{n-k}(z)(q\partial)^k, \qquad (2)$$

where $q = b + 1/b$ and h_k are the weights of the first fundamental representation π_1 of $sl(n)$ with the highest weight ω_1: $h_1 = \omega_1$, $h_k = \omega_1 - e_1 - \ldots - e_{k-1}$. In particular, $W_0 = 1$, $W_1 = 0$, and

$$W_2 = T(z) = -\frac{1}{2}(\partial\varphi)^2 + (Q, \partial^2\varphi)$$

is the stress-energy tensor. Here, $Q = (b + 1/b)\rho$, with ρ being the Weyl vector (half of the sum of all positive roots). The primary fields of the W algebra are exponential fields:

$$V_\alpha = e^{(\alpha,\varphi)}.$$

The main term of the operator product expansion (OPE) of these fields with the currents $W_k(z)$ defines the quantum numbers to $w^{(k)}(\alpha)$ as

$$W_k(z)V_\alpha(z') = \frac{w^{(k)}(\alpha)V_\alpha(z')}{(z-z')^k} + \ldots. \qquad (3)$$

¶ The text was submitted by the authors in English.

[1] This relation is known in, the theory of integrable equations, as a Miura transformation [3].

0021-3640/05/8111-0594$26.00 © 2005 Pleiades Publishing, Inc.

They are known explicitly and are symmetric under the action of the Weyl group $\mathcal{W}$ of the Lie algebra $sl(n)$ [6]

$$w^{(k)}(\alpha) = w_s^{(k)}(\alpha) \equiv w^{(k)}(Q + s(\alpha - Q)), \quad s \in \mathcal{W}. \quad (4)$$

In particular,

$$w^{(2)}(\alpha) = \Delta(\alpha) = (\alpha, 2Q - \alpha)/2$$

is the conformal dimension of the field V_α. Equation (4) means that the fields connected via the action of the Weyl group $\mathcal{W}$ should coincide up to a multiplicative constant

$$V_{Q + s(\alpha - Q)} = R_s(\alpha)V_\alpha. \quad (5)$$

The reflection amplitude $R_s(\alpha)$ was found recently in [7]. Completely degenerate fields that contain $n-1$ null vectors in their Verma moduli are parameterized by two highest weights Ω_1 and Ω_2 of the Lie algebra $sl(n)$ and correspond to $\alpha = -b\Omega_1 - \Omega_2/b$ [6]. In particular, it follows from the definition of the fields $W_j(z)$ (Eq. (2)) that, in the classical case ($q \longrightarrow 1/b$), the field $V_{-b\omega_1}$ satisfies the differential equation of the order n [6]

$$\sum_{k=0}^{n} W_{n-k}(z)(b^{-1}\partial)^k V_{-b\omega_1} = 0. \quad (6)$$

One can expect that, in the quantum case, holomorphic Eq. (6) should still make sense. It was done for the $sl(2)$ Toda or the Liouville field theory in [8]. The precise statement is the following: all four-point correlation functions that contain at least one degenerate field satisfy an ordinary differential equation. In particular, the correlation function with the degenerate field $V_{-mb/2}$ satisfies the ordinary differential equation of order $m+1$. The solution to this equation, which gives a four-point correlation function with one degenerate field $V_{-mb/2}$, can be written in terms of the functions $G_m^{(c,d,g)}(z)$ defined in [9, 10],[2]

$$\langle V_{-\frac{mb}{2}}(z, \bar{z})V_{a_1}(0)V_{a_2}(1)V_{a_3}(\infty)\rangle \sim |z|^{2mba_1}|1-z|^{2mba_2}G_m^{(c,d,g)}(z),$$

where

$$c = b(a_2 + a_3 - a_1 - 2Q + m/2),$$

$$d = b(a_1 + a_3 - a_2 - 2Q + m/2),$$

$$g = -b(a_1 + a_3 + a_2 - 2Q - m/2)$$

and

$$G_m^{(c,d,g)} = \int \prod_{i=1}^{m} d^2t_i |t_i|^{2c}|t_i - 1|^{2d}|t_i - z|^{2g} \prod_{i<j} |t_i - t_j|^{-4b^2}. \quad (7)$$

We will show below that, in the general $sl(n)$ case, such a statement is not valid and that additional restrictions on α_i should be imposed.

Let us assume now that n is general and consider a four-point correlation function

$$\Psi(z) = \langle V_{-b\omega_1}(z)V_{\alpha_1}(z_1)V_{\alpha_2}(z_2)V_{\alpha_3}(z_3)\rangle. \quad (8)$$

Here, $V_{\alpha_k}(z_k)$ are some general primary fields, and we have omitted their $\bar{z}$ dependence for simplicity. Let such a function satisfy the nth-order differential equation

$$(-\partial^n + P(z)\partial^{n-1} + \ldots)\Psi(z) = 0. \quad (9)$$

Then, it should have the following set of canonical solutions:

$$\Psi_k^j(z) = (z - z_k)^{\rho_k^j}(1 + \ldots) \quad (10)$$

where the numbers $\rho_k^j = \Delta(\alpha_k - bh_j) - \Delta(\alpha_k) - \Delta(-b\omega_1)$ are known from the OPE [6]

$$V_{-b\omega_1}(z, \bar{z})V_{\alpha_k}(0, 0) = \sum_{j=1}^{n} C_{-b\omega_1, \alpha_k}^{\alpha_k - bh_j}(|z|^{2\rho_k^j}V_{\alpha_k - bh_j}(0, 0) + \ldots).$$

Here, $C_{-b\omega_1, \alpha_k}^{\alpha_k - bh_k}$ are the structure constants of the operator algebra, and … means the contribution of the descendant fields. Using (10), one obtains the main asymptotic of

$$P(z) = \sum_{k=1}^{3} \frac{p_k}{z - z_k} + \ldots,$$

with

$$p_k = \sum_{j=1}^{n} \rho_k^j - \frac{1}{2}n(n-1).$$

On the other hand, $\Psi(z)$ should satisfy the projective Ward identities. This means that its z dependence is very special:

$$\Psi(z) \sim \frac{\Psi(x)}{(z - z_2)^{2\Delta(-b\omega_1)}}, \quad x = \frac{z_{23}}{z_{13}}\frac{z - z_1}{z - z_2}. \quad (11)$$

Equations (9) and (11) are compatible if

$$\sum_{k=1}^{3} p_k = (n^2 - 1)b^2. \quad (12)$$

[2] Here, we use the common Liouville normalization $\Delta(a) = a(2Q - a)$ and $2Q = b + 1/b$.

In the case under consideration (all α_i are general), we find that

$$p_k = \frac{1}{2}n(n-1)b^2, \quad k = 1, 2, 3.$$

Unfortunately, (12) is satisfied only for $n = 2$. And this is the reason why the differential equation in the Liouville field theory exists.

One can notice that this difficulty is solved if we suppose that $\alpha_3 = \kappa\omega_{n-1}$. Then, only two fields appear in the OPE[3]

$$V_{-b\omega_1}V_{\kappa\omega_{n-1}} = [V_{\kappa\omega_{n-1}-bh_1}] + [V_{\kappa\omega_{n-1}-bh_n}].$$

Now, $p_3 = (n-1)b^2$ and p_1, p_2 remain unchanged. It compensates the balance in the sum $\sum p_k$ and (12) is satisfied. In this case, one can write down the differential equation explicitly. Namely, we define a new function

$$\begin{aligned}&\langle V_{-b\omega_1}(x)V_{\alpha_1}(0)V_{\alpha_2}(\infty)V_{\kappa\omega_{n-1}}(1)\rangle \\ &= |x|^{2b(\alpha_1, h_1)}|1-x|^{2\frac{b\kappa}{n}}G(x, \bar{x}),\end{aligned} \tag{13}$$

where $G(x, \bar{x})$ satisfies the generalized Pochgammer hypergeometric equation

$$\begin{aligned}&[x(x\partial + A_1)\ldots(x\partial + A_n) \\ &-(x\partial + B_1 - 1)\ldots(x\partial + B_{n-1} - 1)x\partial]G(x, \bar{x}) = 0,\end{aligned} \tag{14}$$

with

$$A_k = \frac{b\kappa}{n} - \frac{n-1}{n}b^2 + b(\alpha_1 - Q, h_1) + b(\alpha_2 - Q, h_k)$$

and

$$B_k = 1 + b(\alpha_1 - Q, h_1 - h_{k+1}).$$

Of course, the same equation is valid if we change $x \longrightarrow \bar{x}$. The simultaneous single-valued solution to both equations is unique up to a multiplicative constant and has a simple integral representation:

$$G(x, \bar{x}) = \int\prod_{i=1}^{n-1} d^2t_i|t_i|^{2c_i}|t_i - t_{i+1}|^{2d_i}|t_1 - x|^{2g}, \tag{15}$$

where $t_n = 1$ and

$$c_i = A_i - B_i, \quad d_i = B_i - A_{i+1} - 1, \quad g = -A_1.$$

Now let us explore (15) to obtain the three-point correlation function of the primary fields

$$\begin{aligned}&C(\alpha_1, \alpha_2, \alpha_3) = |z_{12}|^{2\gamma_{12}}|z_{13}|^{2\gamma_{13}}|z_{23}|^{2\gamma_{23}} \\ &\times\langle V_{\alpha_1}(z_1, \bar{z}_1)V_{\alpha_2}(z_2, \bar{z}_2)V_{\alpha_3}(z_3, \bar{z}_3)\rangle,\end{aligned} \tag{16}$$

where γ_{ij} can be found in [8]. We can rewrite (13) using *s*-channel OPE decomposition,

$$\begin{aligned}&\langle V_{-b\omega_1}(x)V_{\alpha_1}(0)V_{\alpha_2}(\infty)V_{\kappa\omega_{n-1}}(1)\rangle \\ &= \sum_{j=1}^{n} C_{-b\omega_1, \alpha_1}^{\alpha_1 - bh_j}C(\alpha_1 - bh_j, \alpha_2, \kappa\omega_{n-1})|\Psi_j(x)|^2,\end{aligned} \tag{17}$$

with $\Psi_j = x^{b(\alpha_1, h_1)}(1-x)^{b\kappa/n}G_j(x)$. The functions $G_j(x)$ are expressed in terms of generalized hypergeometric functions of the type $(n, n-1)$ [11]

$$F\left(\begin{matrix}A_1\ldots A_n \\ B_1\ldots B_{n-1}\end{matrix}\middle| x\right) = 1 + \frac{A_1\ldots A_n}{B_1\ldots B_{n-1}}x + \frac{A_1(A_1+1)\ldots A_n(A_n+1)}{B_1(B_1+1)\ldots B_{n-1}(B_{n-1}+1)}\frac{x^2}{2} + \ldots,$$

as

$$G_1(x) = F\left(\begin{matrix}A_1\ldots A_n \\ B_1\ldots B_{n-1}\end{matrix}\middle| x\right),$$

$$G_2(x) = x^{1-B_1}F\left(\begin{matrix}1-B_1+A_1\ldots 1-B_1+A_n \\ 2-B_1\ldots 1-B_1+B_{n-1}\end{matrix}\middle| x\right),$$

$$\ldots\ldots\ldots\ldots\ldots\ldots$$

$$\ldots\ldots\ldots\ldots\ldots\ldots$$

$$G_n(x) = x^{1-B_{n-1}}F\left(\begin{matrix}1-B_{n-1}+A_1\ldots 1-B_{n-1}+A_n \\ 1-B_{n-1}+B_1\ldots 2-B_{n-1}\end{matrix}\middle| x\right).$$

The ratio of the coefficients before $|\Psi_j(x)|^2$ in (17) can be found from integral representation (15) explicitly in terms of the γ functions $\gamma(x) = \Gamma(x)/\Gamma(1-x)$:

$$\begin{aligned}&\frac{C_{-b\omega_1, \alpha_1}^{\alpha_1 - bh_1}C(\alpha_1 - bh_1, \alpha_2, \kappa\omega_{n-1})}{C_{-b\omega_1, \alpha_1}^{\alpha_1 - bh_k}C(\alpha_1 - bh_k, \alpha_2, \kappa\omega_{n-1})} \\ &= \prod_{j=1}^{n}\frac{\gamma(A_j)\gamma(B_{k-1} - A_j)}{\gamma(B_j)\gamma(B_{k-1} - B_j)}.\end{aligned} \tag{18}$$

Here, we have set $B_0 = B_n = 1$. The structure constants $C_{-b\omega_1, \alpha_1}^{\alpha_1 - bh_k}$ admit the free-field representation [12]

$$\begin{aligned}&C_{-b\omega_1, \alpha_1}^{\alpha_1 - bh_k} = (-\mu)^{k-1} \\ &\times\int\left\langle V_{-b\omega_1}(0)V_{\alpha_1}(1)V_{2Q-\alpha_1+bh_k}(\infty)\prod_{i=1}^{k-1}V_{be_i}(z_i)d^2z_i\right\rangle_0.\end{aligned} \tag{19}$$

The expectation value in (19) is taken using the Wick rules in the theory of a free massless scalar field. This

[3] It follows from the explicit formula for $C_{-b\omega_1, \alpha}^{\alpha - bh_k}$ (20).

integral can be calculated explicitly:

$$C^{\alpha_1 - bh_k}_{-b\omega_1, \alpha_1} = \left(-\frac{\pi\mu}{\gamma(-b^2)}\right)^{k-1} \times \prod_{i=1}^{k-1} \frac{\gamma(b(\alpha_1 - Q, h_i - h_k))}{\gamma(1 + b^2 + b(\alpha_1 - Q, h_i - h_k))}. \quad (20)$$

Equation (18) together with (20) give us the set of functional relations for the three-point function $C(\alpha_1, \alpha_2, \kappa\omega_{n-1})$. There is another, "dual" set of equations with b replaced by $1/b$. One can readily solve them:

$$C(\alpha_1, \alpha_2, \kappa\omega_{n-1}) = [\pi\mu\gamma(b^2)b^{2-2b^2}]^{\frac{(2Q - \Sigma\alpha_i, \rho)}{b}} \times \frac{(\Upsilon_0)^{n-1}\Upsilon(\kappa)\prod_{e>0}\Upsilon((Q-\alpha_1, e))\Upsilon((Q-\alpha_2, e))}{\prod_{ij}\Upsilon\left(\frac{\kappa}{n} + (\alpha_1 - Q, h_i) + (\alpha_2 - Q, h_j)\right)}. \quad (21)$$

Here, $\Upsilon(x)$ is the entire self-dual function defined in [13], which satisfies the relations

$$\Upsilon(x + b) = \gamma(bx)b^{1-2bx}\Upsilon(x),$$

$$\Upsilon(x + 1/b) = \gamma(x/b)b^{2x/b-1}\Upsilon(x)$$

with the normalization condition $\Upsilon(1/2(b + 1/b)) = 1$, and

$$\Upsilon_0 = \left.\frac{d\Upsilon(x)}{dx}\right|_{x=0}.$$

Such a function has a semiclassical limit [14]:

$$\Upsilon(by) \longrightarrow \frac{\Upsilon_0 b^{1-y}}{\Gamma(y)} \text{ as } b \longrightarrow 0. \quad (22)$$

In the numerator of (21), the product goes over all positive roots of the $sl(n)$ and, in $(2Q - \sum\alpha_i, \rho)$, the sum includes α_1, α_2, and $\kappa\omega_{n-1}$.

We propose (21) as an exact three-point function in conformal Toda field theory. Of course, the same is true if we consider $\alpha_3 = \kappa\omega_1$. The answer would be the same as (21), but one should use the weights of the fundamental representation π_{n-1} instead of π_1.

Several simple checks of (21) can be made. In particular, the reflection with respect to the Weyl group $\mathcal{W}$, $\alpha_1 \longrightarrow Q + s(\alpha_1 - Q) : s \in \mathcal{W}$, gives the reflection amplitude

$$C(Q + s(\alpha_1 - Q), \alpha_2, \kappa\omega_{n-1}) = R_s(\alpha_1)C(\alpha_1, \alpha_2, \kappa\omega_{n-1}),$$

with

$$R_s(\alpha) = A_s(\alpha)/A(\alpha), \quad (23)$$

where

$$A(\alpha) = (\pi\mu\gamma(b^2))^{\frac{(\alpha - Q, \rho)}{b}} \times \prod_{e>0}\Gamma(1 - b(\alpha - Q, e))\Gamma(1 - (\alpha - Q, e)/b).$$

Result (23) was obtained previously in [7].

If the parameters in (21) satisfy the screening condition

$$\alpha_1 + \alpha_2 + \kappa\omega_{n-1} + b\sum_{i=1}^{n-1} l_i e_i = 2Q$$

with some nonnegative integer numbers l_i, (21) should have a multiple pole of order $n - 1$, with the residue being expressed in terms of a free field integral [15]. Such an integral was calculated for the Liouville case in [9, 10]. The general $sl(n)$ case was done recently [16], and the result agrees with (21).

It is interesting to consider the semiclassical limit $b \longrightarrow 0$. In this limit in the Hamiltonian picture, associated with radial quantization, we take into account only the zero-mode dynamics (minisuperspace approach) [17, 18]. In this approximation, the state created by the operator V_{Q+iP_j} corresponds to the wavefunction

$$V_{Q+iP_j} \longrightarrow \Psi_{P_j}(x),$$

where x is a zero mode of field φ. The function $\Psi_P(x)$ (the $sl(n)$ Whittaker function) satisfies the Scrödinger equation

$$\left(-\nabla_x^2 + 8\pi\mu\sum_{i=1}^{n-1} e^{b(e_i x)}\right)\Psi_P(x) = P^2\Psi_P(x), \quad (24)$$

and, in the region $(e_i, x) < 0$ (the Weyl chamber), possesses the asymptotic

$$\Psi_P(x) \sim \exp(i(P, x)) + \sum_{s \in \mathcal{W}} S_s(P)\exp(i(s(P), x)),$$

where the sum runs over all elements of the Weyl group $\mathcal{W}$ besides those that are identical, and the coefficients $S_s(P)$ are known exactly [19].[4] The minisuperspace approximation is valid if P_j/b are fixed. If we take $\kappa = ibs$ and $P_i = ibp_i$, then the semiclassical limit of the three-point correlation function should be given by the integral

$$C(Q + ibp_1, Q + ibp_2, bs\omega_{n-1}) \longrightarrow \int d\vec{x}\Psi_{bp_1}(x)\Psi_{bp_2}(x)e^{ibs(\omega_{n-1}, x)}. \quad (25)$$

[4] Note also that $S_s(P)$ can be obtained from the reflection amplitude $R_s(Q + iP)$ in the semiclassical limit $b \longrightarrow 0$.

The theory of the $sl(n)$ Whittaker functions has a long history. In particular, an explicit integral representation for these functions exists [20–22]. Recent progress was made in [23], where the integral on the right-hand side of (25) was calculated:

$$\int d\vec{x}\Psi_{bp_1}(x)\Psi_{bp_2}(x)e^{ibs(\omega_{n-1},x)} = \frac{1}{b^{n-1}}\left(\frac{\pi\mu}{b^2}\right)^{-i\left(s\frac{(n-1)}{2}+(p_1+p_2,\rho)\right)} \times \frac{\prod_{ij}\Gamma\left(\frac{is}{n}+i(p_1,h_i)+i(p_2,h_j)\right)}{\Gamma(is)\prod_{e>0}\Gamma(-i(p_1,e))\Gamma(-i(p_2,e))}. \quad (26)$$

We note that result (26) coincides exactly with the corresponding limit of three-point function (21). Unfortunately, integral (26) with an arbitrary parameter of the Fourier transform is a more complicated object, and its analytical expression is still unknown. In the quantum case, this integral corresponds to the semiclassical limit of a general three-point function (with all α_i being arbitrary). We propose to investigate the general situation in more detail in future publications.

The authors are grateful to D. Lebedev for explanation of some recent results from the theory of the Whittaker functions and to E. Stade for bringing [23] to our attention. A.L. would like to thank A. Belavin, B. Feigin, M. Lashkevich, and Ya. Pugai for useful discussions and suggestions.

This work was supported in part by the European Union under the contract EUCLID HRPN-CT-2002-00325, by INTAS under the grant no. INTAS-OPEN-03-51-3350, by the Russian Foundation for Basic Research under the grant no. 04-02-1602, and by the Russian Ministry of Science and Technology under the Scientific Schools grant no. 2044.2003.2. A.L. thanks also the Forschungszentrum Juelich for financial support, within the framework of the Landau Program, and the "Dynasty" foundation.

REFERENCES

1. J. L. Gervais, hep-th/9310116.
2. P. C. West, hep-th/9309095.
3. V. A. Fateev and S. L. Lukyanov, Int. J. Mod. Phys. A **7**, 853 (1992).
4. A. A. Belavin, Adv. Stud. Pure Math. **19**, 117 (1989).
5. V. A. Fateev and A. B. Zamolodchikov, Zh. Éksp. Teor. Fiz. **89**, 380 (1985) [Sov. Phys. JETP **62**, 215 (1985)].
6. V. A. Fateev and S. L. Lukyanov, Int. J. Mod. Phys. A **3**, 507 (1988).
7. V. A. Fateev, hep-th/0103014.
8. A. A. Belavin, A. M. Polyakov, and A. B. Zamolodchikov, Nucl. Phys. B **241**, 333 (1984).
9. V. S. Dotsenko and V. A. Fateev, Nucl. Phys. B **240**, 312 (1984).
10. V. S. Dotsenko and V. A. Fateev, Nucl. Phys. B **251**, 691 (1985).
11. *Higher Transcendental Functions (Bateman Manuscript Project)*, Ed. by A. Erdelyi (McGraw-Hill, New York, 1955; Nauka, Moscow, 1967), Vol. 3.
12. V. Fateev, A. B. Zamolodchikov, and A. B. Zamolodchikov, hep-th/0001012.
13. A. B. Zamolodchikov and A. B. Zamolodchikov, Nucl. Phys. B **477**, 577 (1996).
14. C. B. Thorn, Phys. Rev. D **66**, 027702 (2002).
15. M. Goulian and M. Li, Phys. Rev. Lett. **66**, 2051 (1991).
16. V. A. Fateev (unpublished).
17. G. W. Moore, N. Seiberg, and M. Staudacher, Nucl. Phys. B **362**, 665 (1991).
18. N. Seiberg, Prog. Theor. Phys. Suppl. **102**, 319 (1990).
19. M. A. Olshanetsky and A. M. Perelomov, Phys. Rep. **71**, 313 (1981).
20. E. Stade, Duke Math. J. **60**, 313 (1990).
21. S. Kharchev and D. Lebedev, Lett. Math. Phys. **50**, 53 (1999).
22. S. Kharchev and D. Lebedev, Pis'ma Zh. Éksp. Teor. Fiz. **71**, 338 (2000) [JETP Lett. **71**, 235 (2000)].
23. E. Stade, Isr. J. Math. **127**, 201 (2002).

JETP Letters, Vol. 81, No. 11, 2005, pp. 599–604. Translated from Pis'ma v Zhurnal Éksperimental'noĭ i Teoreticheskoĭ Fiziki, Vol. 81, No. 11, 2005, pp. 733–738.
Original Russian Text Copyright © 2005 by Molotkov.

On the Maximum Admissible Error and Key Compression Degree in Quantum Cryptography on Two Nonorthogonal States

S. N. Molotkov

Institute of Solid State Physics, Russian Academy of Sciences, Chernogolovka, Moscow region, 142432 Russia

Faculty of Computational Mathematics and Cybernetics, Moscow State University, Vorob'evy gory, Moscow, 119992 Russia

Received April 11, 2005; in final form, May 11, 2005

The extreme admissible error probability at the receiving end to which the secure key distribution is possible has been found. This result takes into account all possible attacks on the distributed key, including those that involve large quantum memory and the capability of an eavesdropper to perform collective measurements simultaneously over the entire transmitted sequence of quantum states. The critical error is independent of the parameters of a particular attack and is determined only in terms of the overlapping degree $\varepsilon = |\langle u_1|u_0\rangle|$ of information states and the fundamental functions of classical and quantum information theories. The latter functions are the capacity $H(Q)$ of a classical binary communication channel and classical capacity $\bar{C}(\varepsilon)$ of a binary quantum communication channel. The key compression degree after error correction is also expressed in terms of only the classical capacity $\bar{C}(\varepsilon)$ of the quantum communication channel. © *2005 Pleiades Publishing, Inc.*

PACS numbers: 03.67.Dt, 42.50.–p, 89.70.+c

Quantum cryptography, i.e., secure key distribution, is based on the fundamental Heisenberg uncertainty relation [1] or, more exactly, on the impossibility of common eigenvectors of a pair of observables that correspond to noncommuting Hermitian operators. Density-matrix operators are observable in quantum cryptography. The density matrices $0 \longleftrightarrow |u_0\rangle$ and $1 \longleftrightarrow |u_1\rangle$ are observables in quantum cryptography [2], where a pair of nonorthogonal states $\rho_0 = |u_0\rangle\langle u_0|$ and $\rho_1 = |u_1\rangle\langle u_1|$ is used as information states. The noncommutativity of operators means the nonorthogonality of the states $|u_0\rangle$ and $|u_1\rangle$ ($\langle u_1|u_0\rangle \neq 0$). The second fundamental quantum-mechanical exclusion is the exclusion of cloning of an *a priori* unknown quantum state [3].

A fundamentally important consequence of the above exclusions for quantum cryptography is the impossibility of measurements that enable one to reliably (with unit probability) distinguish between nonorthogonal states. For this reason, any attempts to eavesdrop (measure) transmitted quantum states change these states. Therefore, the measurement statistics at the receiving end inevitably differs from the measurement statistics on unperturbed states. If quantum mechanics enabled only detection of the eavesdropping attempt itself, it would be useless for secure key distribution. However, quantum-mechanical laws guarantee not only the detection of the eavesdropping attempt but also (and this is the primary interest for cryptography) key security under the condition that changes in statistics do not exceed a certain critical value. Perturbations of the states may evidently arise due to noise in a communication channel in the absence of an eavesdropper. In this sense, it is impossible to distinguish between the actions of the eavesdropper and noise. It is only important that perturbation of the states does not exceed a certain critical value. The critical error to which the secure key distribution is possible is an individual value for each quantum cryptography protocol. There are two basic quantum cryptography protocols on two nonorthogonal states: BB84 [1] and B92 [2]. All other protocols are derivatives of these two basic protocols. The calculation of the critical error is a nontrivial problem. The exact error is known for the BB84 protocol. The first strict and rather complicated proof was given in [4] (see also [5]). More recently, this proof was simplified in [6] using quantum codes. Such a proof has not yet been obtained for the B92 protocol despite its conceptual simplicity.

Below, the proof of the security of the B92 protocol will be outlined on the basis of the exact bounds for the classical capacity of the quantum communication channel.

The standard protocol is as follows. Alice randomly and equiprobably chooses 0 or 1 (with *a priori* probabilities $\pi_0 = \pi_1 = 1/2$) and sends $|u_0\rangle$ or $|u_1\rangle$, respectively, into the communication channel. Bob conducts mea-

surements sequentially with each state. A measurement is described by the unity decomposition

$$I = A_0 + A_1 + A_?, \quad A_0 = \frac{I - |u_1\rangle\langle u_1|}{1 + \langle u_0|u_1\rangle},$$
$$A_1 = \frac{I - |u_0\rangle\langle u_0|}{1 + \langle u_0|u_1\rangle}, \quad A_? = I - A_0 - A_1. \tag{1}$$

This measurement may provide three outcomes, which are interpreted by Bob as 0, 1, and ?. The measurement result in the channel A_0 never occurs on the $|u_1\rangle$ state. Correspondingly, the result in the A_1 channel never occurs on the $|u_0\rangle$ state. The ? outcome is interpreted as an inconclusive result, because the count in the channel $A_?$ can occur on both $|u_0\rangle$ and $|u_1\rangle$ states.

According to the most general strategy, Eve chooses a certain auxiliary state $|A\rangle \in \mathcal{H}$ with sufficiently large dimension, then accumulates the entire sequence of n quantum states sent by Alice, sends nothing to Bob, and connects this auxiliary state with all states:

$$\mathcal{U}(|u_{i_1}\rangle \otimes |u_{i_2}\rangle \otimes \ldots |u_{i_n}\rangle \otimes |A\rangle) = |\Phi_{i_1, i_2, \ldots i_n, A}\rangle, \tag{2}$$

where the $|\Phi_{i_1, i_2, \ldots i_n, A}\rangle$ state is entangled in terms of all $|u_{i_k}\rangle$ states and Eve's initial state $|A\rangle$. Then, without any measurement, Eve sequentially sends $|u_{i_k}\rangle$ states to Bob. Bob carries out measurement (1) with each state. A sequence of outcomes arises in the measurement channels $A_{0,1,?}$. After measurements of the entire sequence, Eve's state is as follows:

$$\mathrm{Tr}_{\mathrm{Bob}}\{\sqrt{A_{j_n}}\sqrt{A_{j_{n-1}}}\ldots\sqrt{A_{j_1}}\mathcal{U}(\rho_{i_1} \otimes \rho_{i_2}$$
$$\otimes \ldots \rho_{i_n} \otimes |A\rangle\langle A|)\mathcal{U}^+\sqrt{A_{j_1}}\sqrt{A_{j_2}}\ldots\sqrt{A_{j_n}}\} \tag{3}$$
$$= \rho^{\mathrm{Eve}}_{i_1, i_2 \ldots i_n}(j_1, j_2, \ldots j_n),$$

where

$$\rho_{i_k} = |u_{i_k}\rangle\langle u_{i_k}|, \quad j_k = 0, 1, ?. \tag{4}$$

Bob can obtain outcomes in the $A_{0,1}$ channels, which are interpreted as 0 and 1, and outcomes with an inconclusive result $A_?$. Outcomes with an inconclusive result are removed by exchanging information between Bob and Alice through the open communication channel, through which Bob reports the position numbers at which such a result is obtained. Having information from the open communication channel, Eve also removes these positions. To this end, it is sufficient to take the partial trace over the degrees of freedom in the state $|\Phi_{i_1, i_2, \ldots i_n, A}\rangle$ that are associated with the numbers j_k? of positions with the ? outcome. As a result, Eve's state is as follows:

$$\mathrm{Tr}_{j_{k_1}?, j_{k_2}?, \ldots j_{k_n}?}\{\rho^{\mathrm{Eve}}_{i_1, i_2 \ldots i_n}(j_1, j_2, \ldots j_n)\}$$
$$= \underbrace{\rho^{\mathrm{Eve}}_{i_1, i_2 \ldots i_n}}_{\mathrm{no}_{k_1, \ldots k_n}} \underbrace{(j_1, j_2, \ldots j_n)}_{\mathrm{no}_{j_{k_1}?, \ldots j_{k_n}?}}. \tag{5}$$

After Bob's measurements and removal of outcomes with an inconclusive result (?), the situation is as follows. Alice knows which state she has sent, Eve has the density matrix, and Bob has the bit string

$$|\mathbf{u}\rangle_{\mathbf{i}} = \underbrace{|u_{i_1}\rangle \otimes \ldots \otimes |u_{i_n}\rangle}_{(i_1, \ldots\ldots i_n)}$$
$$\longrightarrow \rho^{\mathrm{Eve}}_{i_1, i_2 \ldots i_n} \times (j_1, j_2, \ldots j_n) \longrightarrow (j_1, \ldots j_n), \tag{6}$$
$$j_k, i_k = 0, 1.$$

Here, it is assumed that indices are renumbered after the removal of ? outcomes and the length of the remaining string is denoted by the same symbol n as before. Errors are present in certain positions of Bob's string. Discrepancy of the indices of the transmitted states and the obtained results for certain indices $i_k \neq j_k$ arises due to Eve-induced perturbation of states that are sent by Alice. The probability of erroneous positions is determined by Alice and Bob through the open communication channel by reporting a random sample of positions and their content (approximately half of n). The fraction of discrepancies approximates the error probability Q. Then, open positions are rejected. Eve also rejects states referring to these positions in the manner discussed above.

Beginning with this point, the aim of Alice and Bob is to obtain the secure key by correcting errors in the unopened part of the sequence using discussions through the open communication channel. If the error probability is less than the critical value ($Q < Q_c$), which should be determined, the protocol continues; otherwise (if $Q > Q_c$), it is interrupted.

Using quantum-mechanical measurements of $\rho^{\mathrm{Eve}}_{i_1, i_2 \ldots i_n}(j_1, j_2, \ldots j_n)$, Eve aims to refer to Alice's bit string $(i_1, i_2, \ldots i_n)$, i.e., to separate a certain density matrix $\rho^{\mathrm{Eve}}_{i_1, i_2 \ldots i_n}(j_1, j_2, \ldots j_n)$ from the set of 2^n density matrices that correspond to other index sets $(i_1, i_2, \ldots i_n)$ for given indices $(j_1, j_2, \ldots j_n)$. The closeness between Eve's density matrix and that sent by Alice is characterized by the fidelity

$$F(|\mathbf{u}\rangle_{\mathbf{i}}, \rho^{\mathrm{Eve}})$$
$$= \mathrm{Tr}_{\mathrm{Eve}}\{\sqrt{|\mathbf{u}\rangle_{\mathbf{ii}}\langle\mathbf{u}|}\rho^{\mathrm{Eve}}_{i_1, i_2 \ldots i_n}(j_1, j_2, \ldots, j_n)\sqrt{|\mathbf{u}\rangle_{\mathbf{ii}}\langle\mathbf{u}|}\} \leq 1, \tag{7}$$

and $F(|\mathbf{u}\rangle_{\mathbf{i}}, \rho^{\mathrm{Eve}}) = 1$ iff

$$\rho^{\mathrm{Eve}}_{i_1, i_2 \ldots i_n}(j_1, j_2, \ldots, j_n) = |\mathbf{u}\rangle_{\mathbf{ii}}\langle\mathbf{u}|. \tag{8}$$

In the presence of an eavesdropping attack,

$$\rho^{\text{Eve}}_{i_1, i_2 \ldots i_n}(j_1, j_2, \ldots, j_n) \neq |\mathbf{u}\rangle_{\mathbf{ii}}\langle\mathbf{u}|, \tag{9}$$

because another result would contradict the no-cloning theorem; i.e., Eve could acquire information on nonorthogonal states without their perturbation. Eve's state after interaction cannot exactly coincide with the transmitted state. To prove this statement, it is sufficient to consider pairwise all states transmitted by Alice. Let $|\mathbf{u}\rangle_\mathbf{i}$ and $|\mathbf{u}\rangle_\mathbf{m}$ be a pair of such states. The join evolution and further calculation of the trace over Bob's variables provide $\rho^{\text{Eve}}_{i_1, i_2 \ldots i_n}(j_1, j_2, \ldots j_n)$ and $\rho^{\text{Eve}}_{m_1, m_2 \ldots m_n}(j_1, j_2, \ldots j_n)$. The scalar product of these two states of Eve is $\text{Tr}\{\rho^{\text{Eve}}_{i_1, i_2 \ldots i_n}(j_1, j_2, \ldots j_n)\rho^{\text{Eve}}_{m_1, m_2 \ldots m_n}(j_1, j_2, \ldots j_n)\} \leq |_\mathbf{i}\langle\mathbf{u}|\mathbf{u}\rangle_\mathbf{m}|^2$; i.e., the overlapping of Eve's states cannot become less than overlapping of the initial states sent by Alice. A decrease in the scalar product (an increase in the angle) would mean an increase in the distinguishability of the states as compared to the initial states. If this increase were possible, then, using new states as input states for a unitary transformation, one could increase the angle between them (distinguishability) until their complete (reliable) distinguishability, which would contradict the theorem [2]. Thus, the initial states sent by Alice are the best that Eve can acquire. The maximum classical information that can be extracted by Eve from these states is limited by the classical capacity of the quantum communication channel, which coincides with the von Neumann entropy in this case. A conservative estimate overestimating information that can be acquired by Eve reduces to Eq. (8).

We now calculate the critical error Q_c to which secure key distribution between Alice and Bob is possible. We outline a proof in the Shannon limit. At this stage, Alice and Bob have bit strings, and Bob's error probability is Q. Such a situation corresponds to the binary symmetric communication channel between Alice and Bob. Then, Alice randomly generates $M_{AB} - 1$ strings according to the equiprobable distribution on the set of all 2^n bit strings of length n and places M_{AB} strings, along with the transmitted string $(i_1, i_2 \ldots i_n)$, in an open, available handbook:

$$\left\{\begin{array}{c} l_1, l_2, \ldots l_n \\ r_1, r_2, \ldots r_n \\ \ldots\ldots\ldots\ldots \\ \underline{i_1, i_2, \ldots i_n} \\ k_1, k_2, \ldots k_n \end{array}\right\} = M_{AB} \leq 2^{n[H(Q)-\delta]}, \tag{10}$$

$$\delta \longrightarrow 0, \quad n \longrightarrow \infty,$$

where

$$H(Q) = 1 + Q\log Q + (1-Q)\log(1-Q) \tag{11}$$

is the capacity of the symmetric binary classical communication channel.

If $M_{AB} \leq 2^{n[H(Q)-\delta]}$, Bob chooses the correct string $(i_1, i_2, \ldots i_n)$ among the set of M_{AB} strings with unit probability according to the direct coding theorem for the binary classical communication channel. Bob has to compare all M_{AB} strings with his string and to choose a string that is closest to his string in the Hamming distance sense (i.e., these two strings have discrepancies in the minimum number of positions) [7, 8]. After that, Alice and Bob have the same bit strings with unit probability; i.e., the probability of erroneous decoding over all codewords

$$\begin{aligned} P_e(n, M_{AB}) &< (M_{AB}-1)2^{-n[H(Q)-\delta]} \\ &< \varepsilon(n, M_{AB}) \longrightarrow 0 \end{aligned} \tag{12}$$

tends to zero as $n \longrightarrow \infty$ and when $M_{AB} \leq 2^{n[H(Q)-\delta]}$.

We now discuss Eve's actions. Owing to open disposal of the set of codewords (10) in the handbook by Alice, Eve knows that a string of quantum states $|u_{a_1}\rangle \otimes |u_{a_2}\rangle \otimes |u_{a_n}\rangle$ that corresponds to one of the index sets $(a_1, a_2, \ldots, a_n)$ generated by Alice in (10) can be sent. Eve has to separate the only correct string $|\mathbf{u}_\mathbf{i}\rangle$ in the set of M_{AB} code strings sent by Alice. According to the direct coding theorem for the classical capacity of the quantum communication channel [9] (see also [10]), the probability of correct decoding (distinguishing) is equal to unity (Eve can know the correct string) if the number of codewords is $M_{\text{Eve}} \leq 2^{n[\bar{C}(\varepsilon)-\delta]}$, where $\bar{C}(\,)$ is the classical capacity of the quantum communication channel, which is in our case given by the expression

$$\begin{aligned} \bar{C}(\varepsilon) &= -\left(\frac{1-\varepsilon}{2}\right)\log\left(\frac{1-\varepsilon}{2}\right) \\ &-\left(\frac{1+\varepsilon}{2}\right)\log\left(\frac{1+\varepsilon}{2}\right), \quad \varepsilon = |\langle u_0|u_1\rangle|. \end{aligned} \tag{13}$$

According to the recently proven theorem of the so-called strong converse to the quantum channel coding theorem for [11], if the number of codewords is $M_{\text{Eve}} > 2^{n[\bar{C}(\varepsilon)-\delta]}$, the probability of correct decoding (separating the necessary string) is equal to zero. More exactly, the probability of correct decoding tends to zero and, correspondingly, the probability of error tends to unity as

$$P_e(n, M_{\text{Eve}}) > 1 - 2^{-n\alpha(\bar{C}(\varepsilon))} \longrightarrow 1, \tag{14}$$

where $\alpha(\bar{C}(\varepsilon))$ is a certain function.

This statement means that, under the condition $M_{AB} > M_{\text{Eve}}$, Eve cannot know the bit string of Alice and Bob. At the same time, Bob can correct Eve-induced errors in his string with unit probability and has the bit

string identical to that of Alice, which is unknown to Eve. This string is the common secure key for Alice and Bob. Thus, the critical error to which secure key distribution is possible is determined from the condition

$$\overline{C}(\varepsilon) = H(Q_c), \quad (15)$$

where Q_c is expressed only in terms of fundamental quantities and takes into account all possible attacks by Eve on the transmitted key. Under condition (15), quantum cryptography guarantees the security of the key, even if Eve has large quantum memory and can conduct collective measurements (in fact, experimentally realize the projection on linked (entangled) states).

The above argument concerning the generation of the secure key for $Q < Q_c$ is unconstructive, because it involves the concept of the Shannon random coding and requires an exponentially large set of codewords. Random coding ensures the maximum key length; i.e., errors at Bob's end are corrected most efficiently. All other constructively realizable methods for correcting errors provide a shorter final secure key. However, efficiency in the sense of the key length is not as important for quantum cryptography as the guaranteed security of the final key. Security formally means that the mutual information between legitimate users and Eve, who has a particular bit string, is exponentially small in any prechosen security parameter. After compression (random caching) of the key, the final secure key arises, and Eve has infinitely small information on this key. This circumstance is guaranteed by the strict mathematical privacy amplification theorem [12].

Let $x \in X$ be a random variable with the distribution $P_X(x)$ and $R(X)$ be the second-order Renyi entropy given by the expression

$$R(X) = -\log P_c(X), \quad P_c(X) = \sum_{x \in X} P_X^2(x), \quad (16)$$

where $P_c(X)$ is the collision probability, i.e., the probability that the random variable has the same value in two sequential tests. Similar relations are valid for conditional distributions

$$R(X|Y) = -\sum_{y \in Y} P_Y(y) R(X|Y = y). \quad (17)$$

The following relations between the Shannon entropy $H(X)$ and Renyi entropy $R(X)$ are important for further calculation of Eve's mutual information on the key:

$$R(X) \le H(X), \quad H(X) = -\sum_{x \in X} P_X(x) \log P_X(x), \quad R(X|Y) \le H(X|Y). \quad (18)$$

Let $g \in G$ be a random variable with uniform distribution over the set of universal second-order cache functions G [13], g: $X = \{0, 1\}^n \longrightarrow \{0, 1\}^r$ and $K = G(x)$. In this case,

$$H(K|G) \ge R(K|G) \ge r - \log(1 + 2^{r - R(X)}) \ge r - \frac{2^{r - R(x)}}{\ln(2)}, \quad (19)$$

where $H(K|G) = H(G(X)|G)$ is the mean conditional Shannon entropy. Here, the cache function is a random variable.

In the application to quantum-cryptography problems, the following consequence of the theorem is important. Let a joint probability distribution P_{XY} exist that is generally unknown. Here, $X = \{0, 1\}^n$ is the set of bit strings that are identical for legitimate users Alice and Bob after error corrections, and $Y = \{0, 1\}^c$ is Eve's set of bit strings. If the Renyi entropy is $R(X|Y = y) = c$ and Alice and Bob choose cache values of their (identical) strings $K = G(X)$ as the secure key, so that the cache function from $\{0, 1\}^n \longrightarrow \{0, 1\}^r$ is randomly and equiprobably chosen from G, then

$$H(K|G, Y = y) \ge R(K|G, Y = y) \ge r - \log(1 + 2^{r - c}) \ge r - \frac{2^{r - c}}{\ln(2)}; \quad (20)$$

i.e., Eve's information on the key is exponentially small in the parameter $c - r$. The conditional Renyi entropy $R(X|Y = y)$ is expressed in terms of conditional probabilities $P_{X|Y}(X = x|Y = y)$ after error correction in the key. The conditional probability $P_{X|Y}(X = x|Y = y)$ is the probability that this particular bit sequence of Eve $Y = y$ originates from a certain bit string $X = x$ of Alice and Bob.

Eve's mutual information on the secure key is given by the expression

$$I(K; GY) = H(K) - H(K|GY) \le \frac{2^{-s}}{\ln(2)}, \quad H(K) = r, \quad (21)$$

where s is the security parameter that is chosen by the legitimate users. If a string with length n remains after the error correction, the length of the remaining key is equal to

$$r = c - s, \quad (22)$$

which determines the key compression degree after the error correction. The Shannon entropy $H(K)$ is the entropy of a uniformly distributed random variable on the set of the final keys $K = \{0, 1\}^r$, where uniformity is ensured by the universality of the cache function.

The problem now reduces to the determination of the bound for conditional Renyi entropy (17). We will express this fundamental bound in terms of another fundamental quantity—the classical capacity of the quantum communication channel [9].

If error-correction procedures such as Binary [14] or Cascade with rejection of erroneous bits [15] are used, all participants of the protocol after the error correction are in the situation

$$|\mathbf{u}\rangle_{\mathbf{i}} = \underbrace{|u_{i_1}\rangle \otimes \ldots \otimes |u_{i_n}\rangle}_{(i_1, \ldots i_n)} \longrightarrow \rho^{\mathrm{Eve}}_{i_1, i_2 \ldots i_n} \times (i_1, i_2, \ldots i_n) \longrightarrow (i_1, \ldots i_n), \quad i_k = 0, 1. \tag{23}$$

Here, n is the length of the remaining string after the error correction. Alice and Bob have the identical bit strings, and there is a one-to-one correspondence between states $|u_{i_k}\rangle$ that are sent by Alice and Bob's bits $i_k \longleftrightarrow |u_{i_k}\rangle$. Eve has the density matrix of quantum states from which she has to obtain a bit string by means of measurements. According to the conservative estimate in favor of Eve, Eve's density matrix is closest to the sequence of quantum states transmitted by Alice if $\rho^{\mathrm{Eve}}_{i_1, i_2 \ldots i_n}(i_1, i_2, \ldots i_n) = \rho_{i_1} \otimes \rho_{i_2} \otimes \ldots \otimes \rho_{i_n}$, where $\rho_{i_k} = |u_{i_k}\rangle\langle u_{i_k}|$ (in essence, the argument is similar to the above argument when deriving Eqs. (7)–(9)).

Eve aims to determine the index set $y = (j_1, j_2, \ldots j_n)$ by means of quantum-mechanical measurements. The number of decoding regions (set of indices y) that can be decoded by Eve with zero error probability for large n does not exceed $2^{n\bar{C}(\varepsilon)}$. The number of codewords that are present in each decoding region and, correspondingly, are decoded into one codeword, which is the index set $y = (j_1, j_2, \ldots j_n)$, is equal to $2^n/2^{n\bar{C}(\varepsilon)}$. Further, measurements with $2^{n\bar{C}(\varepsilon)}$ outcomes are described by the unity decomposition

$$I = \sum_{y \in Y} X_y, \quad y \in Y = \{0, 1\}^t, \quad t = n\bar{C}(\varepsilon), \tag{24}$$

where X_y are measuring operators fixed to the decoding region y. The conditional probability that Alice has sent the state sequence $\rho_x = \rho_{i_1} \otimes \rho_{i_2} \otimes \ldots \otimes \rho_{i_n}$ ($x = (i_1, i_2, \ldots i_n)$) and that Eve obtains the result $y = (j_1, j_2, \ldots j_n)$ is equal to

$$P_{X|Y}(X = x|Y = y) = \mathrm{Tr}\{\rho_x X_y\}. \tag{25}$$

Since Alice equiprobably sends states in each message, $P_X(x) = 1/2^n$. Then,

$$P_{X|Y}(X|Y = y) = \sum_{x \in X_y} P_X(x) P_{X|Y}(X = x|Y = y) = \frac{1}{2^n} \sum_{x \in X_y} P_{X|Y}(X = x|Y = y) = \frac{2^{n\bar{C}(\varepsilon)}}{2^n}. \tag{26}$$

Here, X_y is the set of words that have been sent by Alice and are decoded in Eve's measurements to the same codeword—the index set $y = (j_1, j_2, \ldots j_n)$.

Let us discuss the key compression degree (see details in [12–16]). Let Alice and Bob choose an r-bit string $K = G(X)$ compressed by the random universal cache function G: $X = \{0, 1\}^n \longrightarrow K = \{0, 1\}^r$ as the secure key. If r is taken as $r = n - t - s = n(1 - \bar{C}(\varepsilon)) - s$, where s is the security parameter, Eve's mutual information on the key is

$$I(K; GY) \le 2^{-s}/\ln(2). \tag{27}$$

In this case, the collision probability and conditional Renyi entropy are given by the expressions

$$P_c(X|Y = y) = \frac{2^n}{2^{n\bar{C}(\varepsilon)}}\left(\frac{2^{n\bar{C}(\varepsilon)}}{2^n}\right)^2, \quad R(X|Y = y) = -\log(P_c(X|Y = y)) = n(1 - \bar{C}(\varepsilon)). \tag{28}$$

Roughly speaking, the conditional Renyi entropy is the number of bits per string that are not known to Eve with unit probability. Eve knows no more than $n\bar{C}(\varepsilon)$ bits per string with unit probability. This number is equal to the string length multiplied by the classical capacity of the quantum communication channel. Correspondingly, she does not know $n(1 - \bar{C}(\varepsilon))$ bits with unit probability, and this number of bits from the string after caching can be used as the secure key.

The overlapping of states (their distinguishability degree) $\langle u_0|u_1\rangle$ is chosen by the legitimate users at the beginning of the protocol and is assumed to be known to all participants. This value is independent of the observed error probability Q. In this sense, there is no optimum overlapping degree. We emphasize that an increase in the overlapping degree leads to an increase in the number of outcomes with an inconclusive result at the receiving end that are rejected, and this procedure reduces the key generation rate.

Thus, the B92 protocol ensures the key security if the error observed at the receiving end does not exceed the critical value determined by Eq. (15). This result takes into account all possible attacks by Eve on the distributed key, including those using large quantum memory and the capability of Eve to perform collective measurements simultaneously over the entire transmitted sequence (so-called projection on entangled or linked states in terms of [9]). The critical error is independent of the parameters of a particular attack and is expressed only in terms of the overlapping degree $\varepsilon = |\langle u_1|u_0\rangle|$ of the information states and the fundamental functions of classical and quantum information theories. The latter functions are the transmission capacity $H(Q)$ of a binary classical communication channel and classical capacity $\bar{C}(\varepsilon)$ of a binary quantum communication channel. The key compression degree after the error

correction is also expressed only in terms of the classical capacity $\bar{C}(\varepsilon)$ of the quantum communication channel.

In conclusion, we note that, if Eve can conduct only individual measurements over a state in each message, the critical error to which secure key distribution is possible is determined by the so-called classical capacity of the quantum channel per shot [9], which is equal to

$$C_1(\varepsilon) = \frac{1}{2}[(1+\sqrt{1-\varepsilon^2})]\log(1+\sqrt{1-\varepsilon^2}) + (1-\sqrt{1-\varepsilon^2})]\log(1-\sqrt{1-\varepsilon^2})], \quad (29)$$

and, always, $C_1(\varepsilon) < \bar{C}(\varepsilon)$. In this case, $C_1(\varepsilon)$ substitutes for $\bar{C}(\varepsilon)$ in Eq. (28) for the key compression degree.

This work was supported by the Russian Foundation for Basic Research (project no. 05-02-17837) and INTAS (grant no. 04-77-7284).

REFERENCES

1. C. H. Bennett and G. Brassard, in *Proceedings of IEEE International Conference on Computers, Systems, and Signal Processing* (Bangalore, India, 1984), p. 175.
2. C. H. Bennett, Phys. Rev. Lett. **68**, 3121 (1992); C. H. Bennett, G. Brassard, and N. D. Mermin, Phys. Rev. Lett. **68**, 557 (1992).
3. W. K. Wootters and W. H. Zurek, Nature **299**, 802 (1982).
4. D. Mayers and A. Yao, quant-ph/9802025.
5. E. Biham, M. Boyer, P. O. Boykin, *et al.*, quant-ph/9912053.
6. P. W. Shor and J. Preskill, quant-ph/0003004.
7. C. E. Shannon, Bell Syst. Tech. J. **27**, 397 (1948); Bell Syst. Tech. J. **27**, 623 (1948).
8. R. G. Gallagher, *Information Theory and Reliable Communication* (Wiley, New York, 1968; Sovetskoe Radio, Moscow, 1974); J. Wolfowitz, Ill. J. Math. **1**, 591 (1957).
9. A. S. Holevo, Probl. Peredachi Inf. **8**, 63 (1972); Probl. Peredachi Inf. **15**, 3 (1979); Usp. Mat. Nauk **53**, 193 (1998); *Introduction to the Quantum Information Theory* (MTsNMO, Moscow, 2002) [in Russian].
10. R. Jozsa and B. Schumacher, J. Mod. Opt. **41**, 2343 (1994); P. Hausladen, R. Jozsa, B. Schumacher, *et al.*, Phys. Rev. A **54**, 1869 (1996); B. Schumacher and M. D. Westmoreland, Phys. Rev. A **56**, 131 (1997).
11. T. Ogawa and H. Nagaoka, quant-ph/9808063.
12. C. H. Bennett, G. Brassard, C. Crépeau, and U. Maurer, IEEE Trans. Inf. Theory **41**, 1915 (1995).
13. J. L. Carter and M. N. Wegman, J. Comput. Syst. Sci. **18**, 143 (1979).
14. C. H. Bennett, F. Bessette, G. Brassard, *et al.*, J. Cryptology **5**, 3 (1992).
15. G. Brassard and L. Salvail, Lect. Notes Comput. Sci. **765**, 410 (1994).
16. A. P. Makkaveev, S. N. Molotkov, D. I. Pomozov, and A. V. Timofeev, Zh. Éksp. Teor. Fiz. (in press).

Translated by R. Tyapaev